CENTRO DE INVESTIGACIONES
EN ÓPTICA, A.C.

OPTICAL FIBER DEVICES BASED ON MODAL INTERFERENCE FOR SENSING APPLICATIONS

In partial fulfillment of the requirements for the degree of Doctor en ciencias (optica)

Advisor: Dr. Alejandro Martínez Ríos

Co-advisor: Dr. David Monzón Hernández

Student: MCO. Guillermo Salceda Delgado

June 2015
León, Guanajuato, México

ACKNOWLEDGEMENTS

To all the people that have made this work possible, especially to:

God
My parents
All my family
Consejo Nacional de Ciencia y Tecnología (CONACYT)
My school Centro de Investigaciones en Óptica (CIO)
My advisors: Dr. Alejandro Martínez Ríos, Dr. David Monzón Hernández, and Dr. Rodrigo Amezcua Correa
All of my professors.
To the project CONACYT 220444 that was granted in the last part of my studies.
The College of Optics and Photonics (CREOL) for allow the realization of my pre doctoral internship.
To the CREOL people that I worked directly with them: Dr. Mohammad Umar Piracha, Dr. Axel Schülzgen, Dr. Enrique Antonio Lopez, PhD student Gisela Lopez Galmiche, and PhD student Amy Van Newkirk
To the company Faz Technology for the collaboration that was made in my pre doctoral work
To the doctors: David Moreno Hernandez, Victor Duran Ramírez, J. Ascensión Guerrero Viramontes, Oliver Pottiez, Gilberto Anzueto Sanchez, and Ismael Torres Gómez, that in one way or the other I worked with them.

Index

Figure index

Summary

In this work, the modal interference effect in optical fibers was used with the aim of sensing applications. By means of tapering single mode fibers and utilizing a special seven-core fiber, modal interference was generated, and the modifications induced by external perturbations, such as bending, were evaluated.

The principal objective of this thesis was the measurement of physical parameters, particularly bending, using optical fiber modal devices. For this modal interference to be controlled, it was made in a single mode fiber. In order to obtain modal interference in a single mode fiber, it is necessary to induce perturbations that cause modal coupling for the generation of more than one mode propagating trough the single mode fiber device, then, by physically perturbing this device, it is possible to change the interference properties which can be monitored to find the magnitude of the physical parameter that causes this interference change.

For the modal coupling in optical fibers there are several kinds of perturbations capable to induce coupling, such as long period gratings, Bragg Gratings, optical fiber tapers, and so on. Everything that causes a breaking of the translational invariance on the longitudinal uniformity of the fiber can be considered as a coupling device. In this case, one way to make the coupling is by using a tapered optical fiber. These tapered optical fibers break the longitudinal invariance of the optical fiber by a diameter change. The optical fiber tapers presented in this work consist of a diameter decrement, then a section with a constant diameter (called waist), then there is an increment of diameter until the original diameter of the untapered fiber is reached.

For the construction of these optical fiber tapers, glass processing systems are utilized. The tapered optical fibers presented in this work were fabricated using a Vytran system model 3400 which permits a precise control of the geometrical dimensions of the tapered optical fiber. However for the proper optical working of the tapered optical fiber, it is necessary to play with parameters, such as filament power, pull velocity, taper pull delay, and initial tension of the fiber, and so on, to find the right parameter combination to construct a well-working tapered optical fiber. Actually, there are many optimization methods for fabrication process where the variations of the parameters involved in the fabrication process is crucial to the quality of the resulting product, such as the Taguchi method. However, due to the weather conditions that affect in the tapered fabrication process, the way to determine the best values of the fabrication parameters mentioned above was empirically.

Depending of the geometrical dimensions of the optical fiber tapers, they can be classified in adiabatic or no adiabatic. For the case of adiabatic tapers, the diameter change is not pronounced, so that, the core field of the un-tapered fiber will be redistributed in the optical fiber taper but it will be maintained in the core structure and there will be no coupling to other modes. On the other hand, for the case of no adiabatic tapers, the diameter change is pronounced enough to cause that the core field of the un-tapered fiber is not capable to follow the new redistribution of

the core structure, causing that a fraction of the light leaks from the core and becomes cladding light (cladding modes). Then, both core and cladding modes will propagate in the waist section, and for an interference between them is necessary a recombination of them. This recombination is made by the increasing diameter section of the tapered optical fiber, where now the effect of this diameter change causes a coupling from the cladding modes to the core mode, making them to interfere and generating an interference pattern which is observed in the spectral response as a modulation of the power transmitted with respect to the wavelength.

One that the modal interferometer is constructed, it can be sensitive to external physical parameters such as temperature or tension and bending, by means of the termo-optic and elasto-optic coefficient, which causes a change in the effective refractive index of the interfering propagated modes in the optical fiber, causing an spectral change in the transmission spectrum. Everything that causes a perturbation of the modes that will be interfering to generate the spectral interference pattern will cause a spectral change that can be tracked in order to determine de magnitude of the physical parameter that perturbed the interfering modes.

Another way to generate modal interference without the necessity to make perturbations to the optical fiber, is using special fibers such as multicore fiber. Depending on the multicore structure, these multicore fibers can have coupling of energy between cores, which generate the so-called super-modes. Those super-modes can interfere between them and produce the modal interference that is necessary for sensing applications. Using a seven core fiber that supports 7 super-modes, it is possible to excite only two super-modes to have a very well defined interference pattern that can be used for sensing applications.

In the first published paper (see chapter 2), we demonstrated experimentally a fiber comb-filter using a Mach-Zehnder fiber interferometer based on two concatenated fiber tapers separated by a distance L. It was also demonstrated that it is possible to tailor the strength and resonance attenuation peak position of the comb-filter by a proper selection of the diameter and length of the waist, the length of the down- and up- transitions, and the separation between them. Using a fiber optic 980HP single mode fiber from Nufern, it was found and demonstrated that the diameter waist has the greater effect to position the interference pattern, the transition length has the greater effect in the size of the interference band, the waist length affects the fringe visibility (changing the optical path of the two interfering signals), and the period is determined by the separation of tapers. It is necessary to mention that each of these parameters may have an effect on all the characteristics of the filter, but the greater effect of each one is as it was mentioned above. The fabrication process of this two identical inline tapered fiber optic comb-filter is quite simple and only takes a few minutes. In this way, all-fiber transmission filters with 50–300 nm spectral width centered in the region of 1200 to 1650 nm with a fringe period of 3 to 36 nm and a fringe bandwidth of 2.5 to 11 nm were demonstrated. The physical length of the devices fabricated range from 15 to 30 mm. Due to the low sensibility to temperature and surrounding refractive index, the device can be easily encapsulated, and the small temperature sensitivity may be compensated during packaging by known methods. The main important result of the present

work is the demonstration of the possibility to easily tailor the spectral position of the interference pattern, its spectral extension, and the fringe visibility, by simply adjusting the tapers geometrical parameters.

This work was based on two no adiabatic concatenated tapers for the construction of a comb-filter. The principal purpose of this work was to study the influence of every geometrical parameter in the optical fiber taper over the spectral shape in the transmitted spectrum, all of this with the purpose of generating desired spectral shapes of the comb-filters for a certain application.

In the second published paper (see chapter 2), we demonstrated a bending sensor using an in-line MZFI based on concatenating two low-loss fused tapers. The device is fabricated using standard single-mode fiber, it is compact, simple to construct, and highly sensitive to bending. The curvature applied to the MZFI induces a coupling of the core mode to cladding modes in the first taper, then in the second taper, the cladding modes are coupled back to the core, both modes interfere, and they produce a wavelength-modulated signal. To measure the changes in the curvature radius, the amplitude of the modulation or fringe visibility, is used. The dynamic range of the sensor can be simply tailored through the proper selection of taper waist diameter or separation between tapers. The effect of the external RI change over the interference fringe visibility is not significant, so that the sensor can be protected by immersing it in a solid protective matrix. The sensor can also be interrogated by analyzing other parameters like intensity or wavelength of one of the interference peaks. All these characteristics make this interferometer very attractive for structural monitoring applications.

This work was based on the fabrication of a bending sensor composed by two identical adiabatic tapers separated by a distance L, it is the same structure that the first published paper presented above, when this structure is bent the refractive index of the device changes by means of the elasto-optic coefficient, producing a perturbation in the modal coupling characteristics and an alteration of the propagation of the interfering modes, causing an increment in the visibility fringes of the transmitted spectrum.

In the third published paper (see chapter 3), an optical fiber sensor that is robust, compact, easy to construct, low-loss, and highly sensitive to bending based in a multicore fiber has been demonstrated. The multicore fiber used for this sensor was a designed seven core fiber; it is spliced between two single mode fibers and acts as a sensor head. Its working principle is based on the interference of two super-modes that are excited by the fundamental mode of a single mode fiber. The bending of the structure sensor induces a wavelength shift of interference pattern and changes in the amplitude of modulation (visibility) in the transmitted spectrum, so that it can be interrogated by either visibility or wavelength peak shift. Its dynamic range can be positioned in a desired range by the proper selection of the seven core fiber length when the sensor is interrogated by visibility, but when it is interrogated by wavelength shift it has sensitivities of around 3000 nm/mm^{-1} in the dynamic range from 200 to 450 mm of bending

radius. For protection it can be embedded in, or coated with, a protective material without disturbing its performance because of its insensitivity to external RI. All of these characteristics make the sensor very attractive for monitoring in structural applications.

This work was based in the super-mode interference presented in a seven core fiber, and using the elasto-optic coefficient, it was possible to change the interference properties between the two propagated super-modes in the seven core fiber. In this case the modal intereference was made by the super-mode interference of a multicore fiber without the necessity of making an alteration of the longitudinal invariance of the fiber.

The construction of fiber optic devices for sensing physical parameters is based on the fabrication of an optical structure capable of guiding at least two modes that will interfere to generate an interference pattern, then by altering the propagating characteristics of those modes by the physical parameter to measure, it is possible to track the spectral changes that will give us the magnitude value of the physical parameter.

Chapter 1

Introduction

A great majority of optical fiber devices used for applications other than information transmission, are based on the interaction between the electromagnetic modes that a given optical fiber structure can guide along its length. The standard single mode fiber only supports one mode, however, it may be conveniently modified to support more than one mode, that may be guided in the core or by the waveguide formed by the cladding and the surrounding media, which usually is air (if the original plastic cover is removed). One of these devices is the tapered fiber sections. Tapered optical fiber devices have been subject of continuous interest since they are advantageous for applications including chemical, biological and physical sensors, intracavity devices in fiber lasers and amplifiers, nonlinear media for supercontinuum generation and many more. On the other hand, there are fibers designed to support more than one mode, like multimode fibers and multi-core fibers. Of particular interest for this thesis are the multicore fibers. In a multicore fiber, the modes guided by each core that composes the fiber structure, jointly form a super-mode whose characteristics may be used to implement novel optical fiber devices.

In this chapter, I describe the general characteristics of tapered fiber devices, their fabrication methods, some of their applications and their operating principle. Then a short introduction about multicore fiber and the super-modes that they support will be presented. At the end of this chapter the content of this thesis is outlined.

1.1 Tapered fiber

A typical tapered fiber consists of an optical fiber section where the geometrical shape, in particular the fiber diameter, is modulated longitudinally. The taper has three well defined zones, the down-taper transition, the waist, and the up-taper transition. In the down-taper and up-taper regions, the fiber diameter decreases and increases, respectively. Between these transition regions, there is a section called the waist, where the diameter is uniform and smaller than the un-tapered original fiber diameter, as it is shown in Fig 1.1

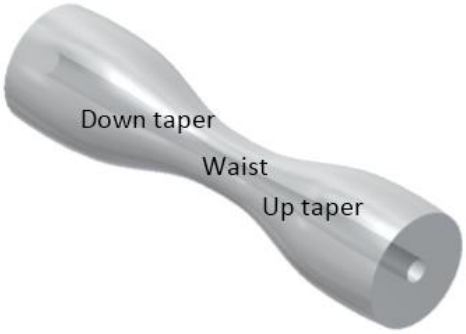

Fig. 1.1 Typical tapered optical fiber. The three regions which are part of it are illustrated, these are down taper, waist and up taper.

Optical fiber tapers have an important role on various applications such as coupling and multiplexing in optical fiber communications systems [1], and light concentrators [2]. They are the basis for many optical components such as directional couplers and beam expanders [3]. Their applications extend to saturable absorbers [4], sensors [5], and supercontinuum generation [6].

1.1.1 Operating mechanism

A model of propagation beams and field analysis for a tapered fiber was presented by Bertilone and co-workers [7, 8]. On the other hand, an exact field analysis was presented by Marcatili [9].
As the guided mode enters the down-taper transitions, more and more light is propagating through the cladding region, i.e. the evanescent part of the field increases. If the diameter reduction is strong enough, a field with a significant portion of it, propagating as an evanescent wave along the waist zone, will be available to interact with the surrounding medium. This is particularly useful for applications in chemical and biological sensors. In general, as the diameter decreases the effective index of the fundamental mode also decreases, and it happens that the core mode transforms into a cladding mode, guided by the cladding-air structure [10]. The confinement of the field in this cladding-air structure may be strong enough to enhance nonlinear effects, which is useful for the study and applications of nonlinear effects, such as the

supercontinuum generation. The above effects are generally observed if the diameter change at the transitions is adiabatic, if the change is not adiabatic, higher order modes will be excited, that still may be useful to fabricate interferometric devices for wavelength filtering. The interferometric fiber devices based on tapered fibers is one of the main subjects of this thesis.

1.1.2 Tapered fiber classification

Tapered fiber may be classified on the basis of the adiabaticity of the taper transitions, that as mentioned above may lead to different effects on the light propagating through the core. In an adiabatic taper, the fundamental core mode LP_{01} remains constant in power, and there is no coupling to higher order cladding modes, or it is negligible. On the other hand in the non-adiabatic case, there is coupling mainly between the fundamental mode propagated from the un-tapered fiber and higher order modes of the fiber structure, with the same symmetry (LP_{02}, LP_{03}, etc.).

1.1.2.1 Adiabaticity criterion

An optical fiber taper is approximately adiabatic if the taper angle (transition angle Ω(z) in Fig. 1.2) is small enough anywhere to ensure that there is negligible loss of power from the fundamental mode as it propagates along the length of the taper [11]. The simplest adiabaticity criteria is the length-scale criterion. It is based in the physical argument that the local taper length-scale must be much larger than the coupling length between the fundamental mode and the dominant coupling mode for power loss to be small [12, 13].

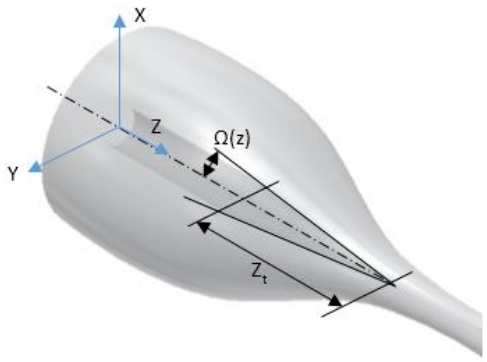

Fig. 1.2. Transition taper with the dimension for the length-scale criterion.

The local taper length scale Z_t (see Fig. 1.2) is the height of a right circular cone with base coincident with the local core cross-section and apex angle equal to the local taper angle (equation 1.1)

$$\Omega(z) = \tan(\frac{d\rho}{dz}) \tag{1.1}$$

where z is the distance along the taper and ρ=ρ(z) is the local core radius, which is a function of z.

The local coupling length between the two modes is the beat length between the fundamental an the second local modes (equation 1.2)

$$Z_b = \frac{2\pi}{\beta_1 - \beta_2} \tag{1.2}$$

where β_1 and β_2 are the respective propagation constants.

Based on length-scale criterion if $Z_t >> Z_b$, everywhere along the taper, then negligible coupling will occur. On the other hand if $Z_b >> Z_t$ there will be a significant coupling, but if $Z_t = Z_b$ there will be an approximate delineation between adiabatic and non-adiabatic tapers. This delineation is equivalent to [12]:

$$\Omega = \frac{\rho(\beta_1 - \beta_2)}{2\pi} \tag{1.3}$$

1.1.3 Manufacturing of tapered fiber

Tapering an optical fiber involves reducing the core and the cladding diameters by heating and pulling in opposite direction from its two ends; this is the well-known heating and pulling technique (see Fig. 1.3). The source of heating can be a flame [4], a focused CO_2 laser beam [14] and an electric arc [15]. The geometrical profile of the tapered fiber section depends on the heat, pulling speed, applied tension, and the fiber material. In general, the pulling is realized by holding the two fiber ends on translation stages driven by stepper motors.

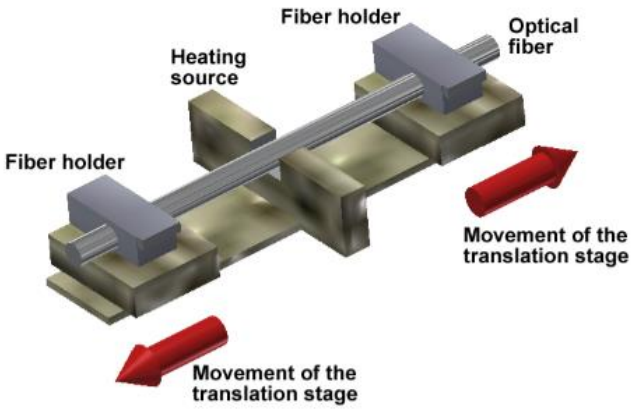

Fig. 1.3. Schematic of the heating and pulling technique for taper optical fibers. The fiber is pulled by the translation stages while it is heated by the heat source.

1.1.4 The importance of the parameters of the tapered optical fibers

The geometrical parameters of the taper, such as the waist diameter, waist length and the transition length determine the taper behavior. Different characteristics and forms of the fiber taper can be achieved by varying the pull and heating conditions, such as pull velocity, length of the heating zone, temperature, and so on [16]. Having a good control of all those parameters during the manufacturing process and knowing their influence on the behavior of fiber tapers a particular performance may be obtained, which is very useful for the design of a determined sensor application. The form of a tapered fiber is very important in situations where the optical fiber taper will be deformed, for example bending the taper for getting miniature devices [17], sensors [18], twist-induced tuning coupler [19], beam expander [20], and so on. So far, diverse forms of tapered optical fiber have been simulated assuming parabolic, sinusoidal, polynomial, among others [21-24]. These forms were obtained measuring real tapers and fitting to these functions [25].

1.1.5 Tapered optical fiber applications and optical fiber sensors

Many tapered optical fiber applications are used for sensing the surrounding refraction index changes [26], through the interaction with the evanescent portion of the field, which may feel the external medium if its diameter is small enough. The radial distribution of modal amplitudes of a guided wave in an optical fiber extends beyond the waveguide dimensions in the form of an evanescent wave that can carry an appreciable part of the guided power, this is the case of a tapered fiber, where the fiber diameter have been reduced to sub micrometer range [27]. In fact the fiber section with the reduced diameter can be bent to very small radii of curvature (1mm or less) with little bend loss, unlike un-tapered fiber [28].

Apart from sensing surrounding refraction index, there are many different tapered optical fiber applications, such as modal interferometers and sensors, spectral filters [29], for multi-wavelength laser [30], for mechanical sensors such as sensing parameters like bending [31], temperature, strain, and so on. In recent years, tapered optical fibers have been used for supercontinuum generation [32] due to their high non-linearity, in near field microscopes. In general, tapered fiber sensors have several advantages, such as high resolution, high sensitivity, small size, fast response, good stability and repeatability [33].

On the other hand, Mach-Zehnder modal interferometers based on tapered fiber sections, have been of great interest for physical and chemical sensing applications, such as temperature, tension, and refraction index, due to the simple, easy, and low price of the tapered optical fiber fabrication [34]. In this modal interferometer a non-adiabatic tapered fiber couples energy from the fundamental mode to cladding modes and vice versa. In this way, when the light is propagating through the first taper, part of the optical energy is coupled to cladding modes, the section between the two tapers (waist) induces a differential phase shift between modes [35], and finally, after the second taper, part of the cladding modes energy is re-coupled to the core mode [36], producing a spectral interference pattern. The modal interferometers are very attractive due to their small size, flexibility, low thermal sensitivity due to the low difference between the fiber modal thermo-optical coefficients [37, 38], it can be used in smart structures applications [39], and it has potential applications as comb filters (multi-wavelength).

1.2 Multicore fiber

A multicore fiber is a special fiber that contrary to the standard single mode fibers having only one center core, can have several cores inside the cladding. They are used to enhance space wavelength multiplexing [40], for sensing applications, such as bending [41], refractive index [42], and strain [43] measurements. They support the so-called super-modes if the distance between cores is small enough to generate energy coupling between cores. For example, using a seven core fiber with coupled cores, it is possible to generate seven super-modes. Playing with those super-modes, it is possible to create sensing optical fiber devices based on super-mode interference. This super-mode interference is controlled by the multicore structure and the interference is also controlled and less chaotic than those devices that use no core or large-core step-index as the devices supporting multiple modes [44].

Playing with the excitation conditions at the input of the multicore fiber, it is possible to control the number of excited super-modes. Using a single mode fiber as an input excitation only two super-modes can propagate through the seven core fiber structure. Taking advantage of this characteristic, it is possible to construct optical fiber devices with well-defined transmission spectrum which are suitable for sensing applications.

1.3 Thesis project.

1.3.1 Manufacture of tapered optical fibers.

The tapered optical fibers are fabricated with the glass processor machine Vytran-GPX 3400. This computerized system uses the heat and pulling technique. It has a carbon filament as a heat source and includes a software interface where we can easily vary all the heat and pulling parameters, and additionally the desired taper dimensions can be set. Fig. 1.4 shows an image for the software window where we can introduce the taper dimensions such as transitions lengths, waist length, waist diameter and fiber diameter.

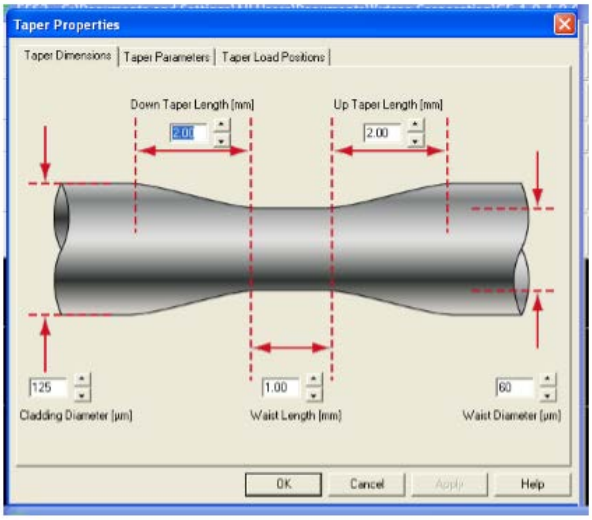

Fig. 1.4. Software window for Vytran-3400 to introduce the taper dimensions

Fig. 1.5 shows the taper fabrication parameters window, where we can vary the heat and pulling parameters to make the taper, the pull velocity (constant pull velocity [mm/s]), filament power (filament start [W]) , initial furnace move, filament delta [%], taper pull delay [s]. It shows the argon gas parameters to prevent the filament for burning. The Vytran system allows the control of the tapers dimensions, so that a systematic study of the influence of the different fabrication factors on the tapers performance is possible.

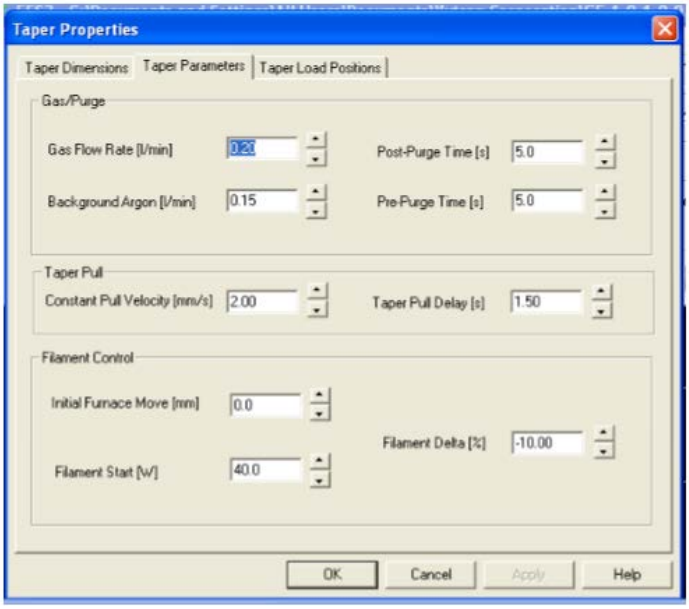

Fig. 1.5. Software window for Vytran-3400 to introduce heating and pulling parameters for the tapering process

1.3.2 Fabricated devices

Firstly, comb filters based on Mach Zehnder modal interferometers with concatenated tapered optical fibers were fabricated. The spectral characteristics (bandwidth, notch depth, period, and position) of this comb filters could be tailored by choosing properly the tapered optical fiber dimensions, while the heat and pulling parameters were varied to optimize losses. This study showed that most part of the changes for central wavelength peak, the amplitude, the period, the bandwidth are caused for varying the dimensions of the waist, waist length, taper separation and transition length respectively.

Mach Zehnder modal interferometers based on two concatenated tapered optical fibers were fabricated. These interferometers have the characteristic that they were adiabatic when they were kept straight, and when they were bent they became gradually non adiabatic. This gradually non adiabatic depended of the bending radius, being a very important characteristic, so a bending sensor were tested and demonstrated.

Optical fiber bending sensor based on super-mode interference on a seven core fiber was characterized and demonstrated. Using a small length of seven core fiber spliced between single mode fibers, it was generated a modulated transmission spectrum based on only two supermodes, when the device was bent the modulated transmitted spectrum suffered a wavelength shift, and at the same time, the visibility was altered too. Both changes, the wavelength shift and the visibility, were used to determine the bending radius of the optical fiber device.

1.3.3 General thesis content.

In chapter 2, the results of all the modal devices based on tapered fibers which were fabricated are presented and described.
In chapter 3, the modal device based on multicore fiber is presented and discussed
In chapter 4, the conclusions of this thesis work are presented.
In appendix A, a the mathematica code used for the simulation of light propagation through tapered fibers, and Mach-Zender interferometers based on them are outlined.

1.4 References

[1] A. K. Agarwal, Fiber, Int. Opt., 6, 27, 1987.
[2] D. Marcuse, “Compression of a Bundle of light Rays”,Appl. Opt., 10, 494, 1971.
[3] K. Jedrzejewski, “Biconical fused taper - a universal fibre devices", technology, Opto-Electr. Rev., Vol. 8, No. 2, pp. 153-159, 2000.
[4] K. Kieu and M. Mansuripur "Femtosecond laser pulse generation with a fiber taper embedded in carbon nanotube/polymer composite", Opt. Lett., Vol. 32, No. 15, pp. 2242-2244, 2007.
[5] K. Kieu y M. Mansuripur, "Biconical Fiber Taper Sensors", IEEE Photon. Technol.,Lett. Vol. 18, No. 21, pp. 2435-2437, noviembre 1 2006.
[6] T. A. Birks, W. J. Wadworth y P. St. J. Russel,"Supercontinuum generation in tapered fibers, Opt. Lett., Vol. 25, No. 19, pp. 1415-1417, 2000.
[7] Derek Bertilone and Colin Pask, “Exact ray paths in a graded-index taper”, Appl. Opt. 26, 7, 1189, 1987.
[8] D. Marcuse, A. Ankiewicz and C. Pask, “wave propagation in a graded-index taper”, Appl. Opt., 26, 2213, 1987.
[9] Derek Berrtilone, "Ray propagation and compression in a strictly adiabatic taper", Optical and Quantum Electronics, 19, pp. 361-375, 1987.
[10] Aiping Luo, Kan Gao, Feng Liu, Ronghui Qu y Zujie Fang, "Evanescent- field coupling based on long period grating and tapered fiber", Opt. Communications, 240, pp. 69-73 2004.
[11] J.D. Love, W.M. Henry, W.J. Stewart, R.J. Black, S. Lacroix, F. Gonthier, "Tapered single-mode fibers and devices Part 1: Adiabaticity criteria", IEE Proceedings-J., Vol. 138, No. 5, October 1991.
[12] Stewart, W.J., and Love, J.D., "Design limitation on tapers and couplers in single-mode fiber", 5th Int. Conf. Integrated Opt. & Opt. Fibre Commun./ 11th European Conf. Opt. Commun. Istituto Internazionale delle Comunicazioni, Venice, Italy, 1985, p. 559-562.
[13] Love J.D. "Application of a low-loss criterion to optical waveguides and devices", IEE Proc. J.,1989,136, p. 559-562.
[14] L. Y. Shao, A. P. Zhang, W. S. Liu, H. Y. Fu y S. He, "Optical refractive- index sensor based on dual fiber-Bragg gratings interposed with a multimode-fiber taper", IEEE Photonics Technol., Lett. 19, pp. 30-32 2007.

[15] F. Lissillour, D. Messager, G. Stephan y P. Feron, "Whispering gallery- mode laser at 1.561lm excited by a fiber taper", Opt. Lett., vol. 26, no. 14, pp. 1051 - 1053, Oct. 1991.
[16] B. Musa, A. A. Rozi, A. S. M. Noor, A. Ismail y M. A. Mahdi, "Effect of fiber profile parameters on the transmission properties of the tapered optical fibers", 978-1-61284-264-6/11/26.00 2011 IEEE
[17] C. Caspar, y E. J. Bachus, "Fiber-optic micro-ring-resonator with 2 mm diameter", Electron. Lett., Vol. 22, pp. 1506-1508, 1989.
[18] L. C. Bobb, P. M. Shankar, y H. D. Krumbolts, "Bending effects in biconically tapered single-mode fibers", J. Lighwave Technol., Vol. 8, pp. 1084-1090, 1990.
[19] T. A. Birks, "Twist-induced tuning in tapered fiber couplers", Appl. Opt., Vol. 28, pp. 4226-4233, 1989.
[20] K. P. Jedrzejewskii, F. Martinez, J. D. Minelly, C. D. Hussey y F. P. Payne, "Tapered-beam expander for single-mode optical-fibre gap devices", Electron. Lett., Vol. 22, pp. 105-106, 1986.
[21] W. J. Stewart y J. D. Love, "Desing limitation on tapers and couplers in single mode fibers", in proc. ECOC 85 (Venice), 1985, pp. 559-562.
[22] J. D. Love, y W. M. Henry, “Quantifying loss minimisation in single-mode fibe taper", Electron. Lett., Vol. 22, pp. 912-914, 1986.
[23] J. Bures, S Lacroix y J. Lapierre, "Analyse d un coupleur bidirectionnel a fibres optiques monomodes fusionnees", Appl. Opt., Vol. 22, pp. 1918-1922, 1983.
[24] W. K. Burns, M. Abebe y C. A. Villarruel, "Parabolic model for shape of fiber taper", Appl. Opt., Vol. 24, pp. 2753-2755, 1985.
[25] Tomothy A. Birks y Youwei W. Li, "The shape of fiber tapers", Journasl of lightwave technol., Vol. 10, No. 4, april 1992.
[26] G. Salceda-Delgado, D. Monzon-Hernandez, A. Martinez-Rios, G. A. Cardenas-Sevilla, and J. Villatoro, "Optical microfiber mode interferometer for temperatura-independent refractometric sensing", Optics Letters, Vol. 37, No.11, June 1, 2012.
[27] Jacques Bures y Rene Ghosh, "Power density of the evanescent field in the vicinity of a tapered fiber", J. Opt. Soc. Am. A, Vol. 16. No. 8, august 1999.
[28] T. A. Birks, K. P. Oakley, y C. D. Hussey, "Adiabaticity of miniature loops in tapered single-mode fiber, Electron Lett.., 2034-2035, 1992.
[29] Guillermo Salceda-Delgado, Alejandro Martinez-Rios, and David Monzón-Hernández, "Tailoring Mach-Zehnder Comb-Filters Based on Concatenated Tapers", Journal of Lightwave Technology, Vol. 31, No. 5, March 1, 2013.
[30] O Pottiez, A Martinez-Rios, D Monzon-Hernandez, G Salceda-Delgado, J C Hernandez-Garcia, B Ibarra-Escamilla and E U Kuzin, " Multiple Continuous-wave and pulsed modes of a figure-of-eight fibre laser", Laser Phys. 23(2013) 035103 (7pp).
[31] D. Monzon-Hernandez, A. Martinez-Rios, I. Torres-Gomez, and G. Salceda-Delgado, "Compact optical fiber curvature sensor base don concatenating two tapers", Optic Letters, Vol. 36, No. 22, November 15, 2011.

[32] T.A. Birks, W.J. Wadsworth and P.St. J. Russell, “Supercontinuum generation in tapered fibers”, Opt. Lett. 25, 1415, 2000.
[33] Di Wu, Tao Zhu, Ming Deng, De-Wen Duan, Lei-Lei Shi, Jun Yao y Yun-Jiang Rao, "Refractive index sensing based on Mach-Zehnder interferometer formed by three cascaded single-mode fibers tapers", Appl. Opt., Vol. 50, No. 11, 10, april 2011.
[34] Z. Tian, S. S. H. Yam, J. Barnes, W. Bock, P. Greig, J. M. Fraser, H. P. Loock y R. D. Oleschuk, “Refractive index Sensing With Mach-Zehnder interferometer Based on Concatenating Two single-mode Fiber Tapers”, IEEE Photon. Technol. Lett. 20, 626 2008.
[35] Z. Tian, J. Barnes, W. Bock, P Greig, J. Fraser, H. Loock y R. Oles- chuk, "Refractive index sensing with Mach-Zehnder interferometer based on conca- tenating two single mode fiber tapers", IEEE Photon. Technol. lett., Vol. 20, No. 8, pp. 326-628 abril 2008.
[36] Changjian Guo, Michael Nix, Scott S. H. Yam, y Saling He, "Picosecond and Sub-Picosecond Flat-Top pulse shaping using abrupt taper interferometers", Journal of lightwave technol., Vol. 28, No. 6, marzo 15 2010.
[37] T. A. Eftomov, and W. J. Brock, “Sensng with a LP01-LP02 intermodal interferometer”, Journal of lightwave technol., Vol. 11, 2150,
1993.
[38] O. Frazao, P. Caldas, F. M. Ara_ujo, L. A. Ferreira y J. L. Santos, "Picosecond and Sub-Picosecond Flat-Top pulse shaping using abrupt taper interferometers", Journal of lightwave technol., Vol. 28, No. 6, marzo 15 2010.
[39] Fiber optic smart structures E. Udd, (Wiley - Interscience 1995).
[40] Sercan Ö. Arık and Joseph M. Kahn, “Coupled-core Multi-core fibers for spatial multiplexing”, IEEE Photonics Technology Letters, Vol. 2, No. 21, November 1, 2013
[41] G. Salceda-Delgado, A. Van Newkirk, J. E. Antonio-Lopez, A. Martinez-Rios, A. Schülzgen, and R. Amezcua Correa, “Compact fiber-optic curvature sensor based on super-mode interference in a seven-core fiber”, Optics Letters, Vol. 40, No. 7, Abril 1, 2015.
[42] Ai Zhou, Guangping Li, Yanhui Zhang, Yuzhuo Wang, Chunying Guan, Jun Yang, and Libo Yuan, “Asymmetrical Twin-Core Fiber Based Michelson Interferometer for Refractive Index Sensing”, JOURNAL OF LIGHTWAVE TECHNOLOGY, VOL. 29, NO. 19, OCTOBER 1, 2011
[43] R. M. Silva, M. S. Ferreira, J. Kobelke, K. Schuster, and O. Frazão1, “Simultaneous measurement of curvature and strain using a suspended multicore fiber”, October 1, 2011 / Vol. 36, No. 19 / OPTICS LETTERS.
[44] Amy Van Newkirk, Enrique Antonio-Lopez, Guillermo Salceda-Delgado, Rodrigo Amezcua-Correa, and Axel Schülzgen, “Optimization of multicore fiber for high-temperature sensing”, OPTICS LETTERS / Vol. 39, No. 16 / August 15, 2014

Chapter 2 Modal devices based on tapered fibers

Resume

In this chapter the experimental results that were obtained with interferometric devices based on concatenated tapers are presented. First, the fabrication of comb-filters based on concatenating two tapers, whose transmission spectrum characteristics, such as central wavelength, amplitude, period and width, can be modified by the geometry of the two concatenated tapers, in order to get a determined comb filter with a desired transmission spectrum. Then an application for measuring micro-displacements is described with one of these devices to prove the sensing characteristics that those devices can show. In addition I describe a highly sensitive bending sensor based on two concatenated tapers. This sensor can be interrogated by visibility changes or by intensity.

2.1 Tailoring Mach-Zehnder Comb-Filters Based on Concatenated Tapers

In this section an all-fiber comb-filter constructed by concatenating two tapers is described. Depending of the geometrical shape of the two concatenated tapers, which are identical, the transmission interference pattern parameters such as, the central wavelength, the amplitude, the period, and the spectral width can be tailored. Therefore, it is possible to produce a desired interference pattern for a specific application of the comb-filter

The dimensions which conform the geometrical shape of the tapers, such as, diameter and length of the waist, length of the up- and down-transition, and even the separation between both concatenated tapers are critical for the shape of the transmission interference pattern. Depending on these geometrical taper parameters, the central position and span of the spectral interference pattern were tailored in the range of l200-1650 and 50-300 nm, respectively. Also by varying the interferometer length, separation between tapers, the fringe period and bandwidth were tailored between 3-36 and 2.5-11 nm, respectively.

The total physical length of the devices fabricated ranges from 15 to 30 mm. They are simple and suitable for applications in optical communications systems, fiber lasers, and in sensing, for the monitoring of strain and displacement.

2.1.1 Introduction

Dense-wavelength-division-multiplexed systems [1-4], multi-wavelength fiber lasers [5], and metrological measurements [6] are the most attractive and useful applications that the Comb-filters have. So far, there is an important number of comb-filters schemes proposed, most of them are based on the modal Mach-Zehnder fiber interferometers (MZFI) [2, 3, 5, 7]. This modal MZFI is one of the simplest methods to fabricate an in-line single-fiber comb-filter. The classical structure for this modal MZFI consists of two concatenated mode coupling fiber devices which can be long-period fiber gratings (LPG) [8] or tapered fiber sections [9, 10].

In mode coupling devices like those listed above, part of the propagating light, which is confined in the core fiber, is coupled to the cladding and becomes a cladding mode, and vice versa. When these devices are arranged in a concatenated way, a characteristic interference pattern of a modal Mach-Zehnder interferometer is generated.

A very regular interference pattern has been presented using a LPG-based MZFI [8], nevertheless, the span fringe interference of the transmission band is limited only to a few tens of nanometers, additionally, the temperature and strain sensitivity of the Fiber Bragg Grating (FBG) may alter the stability of the filter. On the other hand, the MZFIs based on two concatenated tapers reported up to now, the interference pattern have been very irregular, and also they have shown high insertion loss such as more than 5 dB. [9-11]. The reason of these irregularities in the transmission spectrum may be due to the high non adiabaticity that optical fiber tapers possess

when they are fabricated by electric arc discharge, since it is common the generation of abrupt transitions due to the application of the electric arc when the fiber is pulled. These abrupt transitions allow the excitation of more than two modes that generates irregularities in the modal interference transmission spectrum, and it may contribute significantly to insertion losses.

The construction of tapered optical fiber can be easily done in almost any kind of fiber by using a commercial fiber fusion splicer or a home-made tapering machine, but the final taper geometry is extremely difficult to control with these types of machines.

It is demonstrated in an experimental way that constructing fiber comb-filters based on a modal MZFI can be done by fabricating two fiber tapers in series. These comb-filters have very regular fringe interference and low insertion losses. The MZFI were fabricated in commercial fiber 980 HP from Nufern, a single mode fiber with a cut-off wavelength around 980 nm. For the fabrication of the concatenated tapers it was used the Vytran glass processing system, which allows us to precisely control the taper parameters. We found that the central wavelength, the amplitude, the period and the spectral extension of the filter can be tailored by adjusting the diameter and the length of the taper waist, the separation between tapers, and the taper transition length, respectively. For the 980 HP fiber the best filter characteristics were found for a taper waist diameter of 60 um, however, this filter can be done in any other fiber just by finding the right parameters for the construction of this interferometer.

The fiber comb-filters that were demonstrated for this work show low sensitivity to temperature and external refractive index, which is a good response for porpoises of packaging for practical applications.

2.1.2 Principle of operation of the modal MZFI

The structure of the modal MZFI consists in two identical abrupt tapers in series, separated by an optical fiber segment with a length of L, just as it is shown in Fig. 2.1. The geometrical parameters that make up the MZFIs devices are taper transition Lt, waist length L_W, waist diameter D_W, separation between tapers L. Considering all these geometrical parameters, a response analysis was made to determine the influence of every geometrical parameter on the transmitted spectrum shape. This analysis allowed the fabrication of MZFIs with a desired transmission spectra, for a determined application. Aside from multiple sensing applications because of the spectral shape of these devices, the most common application is as a comb filter.

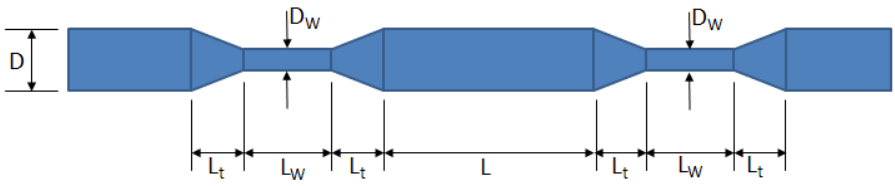

Fig. 2.1 Structure of the two concatenated tapers device. It consists of two identical optical fiber tapered sections separated by the distance L, and the geometrical parameters are L_t (Taper transition), L_W (Waist length), D_W (Waist diameter), and D (normal cladding diameter).

The operating principle of this kind of MZFI can be described as follows, a fraction of the fundamental core mode energy guided in the un-tapered fiber is coupled to higher order cladding modes when it is propagated in the first taper, this coupling is between modes with the same azimuthal symmetry [12], then both modes accumulate a phase difference when they propagate through a fiber section of length L, then the cladding modes are recombined into the core mode when they travel along the second taper. Due to the coupling, recombination and the accumulating phase difference between modes, the transmission spectra of the MZFI is dependent of the wavelength and has an oscillatory response.

As it is noticed in Fig. 2.1 both tapers have same geometrical parameters and they were also fabricated under the same conditions. The taper parameters such as the un-tapered fiber core diameter (D_{core}), un-tapered cladding diameter (D_{clad}), the taper transition length (L_t), the taper waist length (L_w), and taper waist diameter (D_w) are responsible of the mode coupling conditions, therefore they play an important role over the MZFI transmission spectrum.

In order to model the fundamental mode evolution, the core radius change through the down- and up-taper transitions with respect to z are given by [13]

$$r_{\mathrm{co}}^{\mathrm{down}}(z_t) = r_{\mathrm{co}} - \left(\frac{D_w}{D_{\mathrm{cla}}}\right) z_t \tag{1}$$

$$r_{\mathrm{co}}^{\mathrm{up}}(z_t) = \frac{D_w}{2} + \left(\frac{D_w}{D_{\mathrm{cla}}}\right) z_t \tag{2}$$

where D_{cla} is the original cladding diameter, D_w is the cladding diameter at the waist, and z_t goes from 0 to L_t. Similar relations are valid for getting the down- and up-taper cladding radius.

In this work it is considered that the fabricated tapers are axisymmetric, a solution scalar model is used to determine the device response. Consequently the fundamental LP_{01} mode is coupled to modes of the same symmetry (LP_{0m} modes).

Assuming a matching cladding refractive index profile, the characteristic equations for the core mode (equation 3) and cladding modes (equation 4) can be obtained by the scalar model [13, 14] as

$$\frac{J_1(U)}{J_0(U)}\{I_1(\mathrm{SW})K_0(W)+I_0(W)K_1(\mathrm{SW})+\frac{T}{W}\frac{K_1(\mathrm{ST})}{K_0(\mathrm{ST})}(K_0(W)I_0(\mathrm{SW})-I_0(W)K_0(\mathrm{SW}))\}=$$
$$\frac{T}{U}\frac{K_1(\mathrm{ST})}{K_0(\mathrm{ST})}(I_1(W)K_0(\mathrm{SW})+K_1(W)I_0(\mathrm{SW}))+\frac{W}{U}(K_1(W)I_1(\mathrm{SW})-I_1(W)K_1(\mathrm{SW})) \quad (3)$$

$$\frac{J_1(U)}{J_0(U)}\{Y_0(Q)J_1(\mathrm{SQ})-J_0(Q)Y_1(\mathrm{SQ})+\frac{T}{Q}\frac{K_1(\mathrm{ST})}{K_0(\mathrm{ST})}(J_0(Q)Y_0(\mathrm{SQ})-Y_0(Q)J_0(\mathrm{SQ}))\}=$$
$$\frac{T}{U}\frac{K_1(\mathrm{ST})}{K_0(\mathrm{ST})}(J_1(Q)Y_0(\mathrm{SQ})-Y_1(Q)I_0(\mathrm{SQ}))-\frac{Q}{U}(J_1(Q)Y_1(\mathrm{SQ})-Y_1(Q)J_1(\mathrm{SQ})) \quad (4)$$

Where the normalized parameters are defined by [13, 14]

$$U=kr_1\sqrt{n_1^2-n_{\mathrm{eff}}^2}\,;W=kr_1\sqrt{n_{\mathrm{eff}}^2-n_2^2}\,;\ Q=kr_1\sqrt{n_2^2-n_{\mathrm{eff}}^2}\,;\ T=kr_1\sqrt{n_{\mathrm{eff}}^2-n_3^2} \quad (5)$$

Where r_1 is the local core radius, k is the free-space propagation constant, n_1, n_2, and n_3 are the core, cladding, and surrounding medium refractive indices, and n_{eff} is the effective refractive index of the mode to be calculated.

Utilizing a root finding algorithm, equations (3) and (4) are solved for n_{eff} as a function of radius, such as it is defined by equations (1) and (2), and wavelength. It was assumed the surrounding medium to be air, so that the refractive index of the third layer is the unity. As an effective index behavior it was noted that both effective refraction indexes of the core and cladding modes were decreasing as the core radius decreases too.

Another important parameter that has to be considered in optical fiber tapers is the coupling of energy from the core mode caused in the taper transitions due to the fact that the fundamental core field distribution cannot follow the geometric variation of the cross-section resulting in a power lost to higher order. The geometrical amount of change in the cross-section related with the adiabaticity will determine the power lost to higher order modes. The way for quantifying the amount of power that is coupled is by means of the factor called the coupling coefficient, which determines the power transfer from the fundamental core mode to higher order cladding modes at the taper transitions.

It was considered that the coupling takes place at the down- and up-taper transitions only between the LP_{01} and LP_{02} modes. In order to calculate this coupling coefficient between the LP_{01} and LP_{02} core and cladding modes, respectively, the following expressions for the fields at each layer are considered [13, 14]:

$$\Psi_{0i}(R) = \begin{cases} A_{01}J_0(\mathrm{UR}), o \le R \le 1 \\ B_{0i}\Gamma_1 + C_{01}\Gamma_2, 1 < R \le S \\ D_{0i}K_0(\mathrm{TR}), R > 0 \end{cases} \quad (6)$$

Where Γ_1 and Γ_2 are equal to $I_0(\mathrm{WR})$ and $K_0(\mathrm{WR})$ for the LP_{01} mode, respectively, and equal to $J_0(\mathrm{QR})$ and $Y_0(\mathrm{QR})$ for the LP_{02} mode, respectively. Using boundary conditions and setting $A_{01} = 1$, it is obtained [13]:

$$B_{01} = -UJ_1(U)K_0(W) + WJ_0(U)K_1(W)$$

$$C_{01} = WI_1(W)J_0(U) + UI_0(W)J_1(U)$$

$$D_{01} = \frac{I_0(\mathrm{SW})B_{01} + K_0(\mathrm{SW})C_{01}}{k_0(\mathrm{TS})} \quad (7)$$

Here $R = r/r_1$, $S = r_2/r_1$

For the LP_{02} mode, it is again set $A_{02} = 1$ to obtain [13]

$$B_{02} = \frac{\pi(UJ_1(U)Y_0(Q) - QJ_0(U)Y_1(Q))}{2}$$

$$C_{02} = \frac{\pi(QJ_0(U)J_1(Q) - UJ_0(Q)J_1(U))}{2}$$

$$D_{02} = \frac{J_0(\mathrm{SQ})B_{02} + C_{02}Y_0(\mathrm{SQ})}{K_0(\mathrm{TS})} \quad (8)$$

The coupling of the fundamental core mode to higher order cladding modes can be modeled through the following coupled-mode equations [12, 13, 15]:

$$\frac{\mathrm{da}_m}{\mathrm{dz}} = \mathrm{i}\beta_m(z)a_m(z) + \sum_{n=1\neq m}^{N} k_{\mathrm{mn}}(z)a_n(z) \quad (9)$$

Where $\mathrm{a}_m(z)$ and $\beta_m = 2\pi\, n_{\mathrm{eff},m}/\lambda$, are the complex amplitude and propagation constant of the mode mth mode. And the coupling coefficient k_{12} which determines the coupling between the LP_{01} and LP_{02} modes is given by [13, 14]:

$$k_{12} = \frac{1}{2n_1}\frac{\frac{\mathrm{d}\rho}{\mathrm{dz}}}{n_{01}-n_{02}}\frac{\int_{\mathrm{A}\infty}\psi_{01}\psi_{02}\frac{\partial n^2}{\partial r}dA}{(\int_{\mathrm{A}\infty}\psi_{01}^2\,dA)^{1/2}(\int_{\mathrm{A}\infty}\psi_{02}^2\,dA)^{1/2}} \quad (10)$$

Where n_{01} and n_{02} denote the effective indexes of the LP_{01} and LP_{02} modes.

Considering a step index variation of the refractive index profile in the optical fiber taper, the squared refractive index can be written in terms of Heaviside functions [12], so that (10) can be evaluated analytically, by using the equations (6-8) and the continuity of the fields at each interface. The resultant expression is written as [12, 13]:

$$k_{12} = \frac{2}{r_1^2} \frac{1}{(F_1 F_2)^{1/2}(n_{01}-n_{02})} \times \{(n_1^2 - n_2^2) J_0(U_{01}) J_0(U_{02}) + (n_1^2 - n_3^2) K_0(T_{01} K_0(T_{02})\} \qquad (11)$$

Here the subscripts 01 and 02 in the modal parameters U and T emphasize that they must be evaluated using the corresponding effective index of the LP_{01} or LP_{02} mode, and the factors F_1 and F_2 are given by [13]

$$\begin{aligned} F_1 = \{&(J_0^2(U_{01}) + J_1^2(U_{01})) + B_{01}^2 S^2 (I_0^2(\mathrm{WS}) - I_1^2(\mathrm{WS})) - B_{01}^2 (I_0^2(W) - I_1^2(W)) \\ &+ C_{01}^2 S^2 (K_0^2(\mathrm{WS}) - K_1^2(\mathrm{WS})) - C_{01}^2 (K_0^2(W) - K_1^2(W)) - D_{01}^2 S^2 (K_0^2(T_{01} S) \\ &- K_1^2(T_{01} S))\} \end{aligned} \qquad (12)$$

$$\begin{aligned} F_2 = \{&(J_0^2(U_{02}) + J_1^2(U_{02})) + B_{02}^2 S^2 (J_0^2(\mathrm{QS}) - J_1^2(\mathrm{QS})) - B_{02}^2 (J_0^2(Q) + J_1^2(Q)) + C_{02}^2 S^2 (Y_0^2(\mathrm{QS}) \\ &+ Y_1^2(\mathrm{QS})) - C_{02}^2 (Y_0^2(W) + Y_1^2(Q)) - D_{02}^2 S^2 (K_0^2(T_{02} S) - K_1^2(T_{02} S))\} \end{aligned} \qquad (13)$$

For the evaluation of the coupling coefficients it is necessary to calculate the effective indices of the LP_{01} and LP_{02} for a specific range of wavelengths and radii to solve equation (10) for those specific ranges. The coupled amplitude equations were solved for the case of a concatenated taper device with the following geometrical dimensions: L_T = 2.5 mm, L_W = 1 mm, L = 2 cm, D = 125um, with the waist diameter D_W of 60, 62, and 64 um in order to analyze the effect of the variation in this parameter. Fig. 2.2 shows the simulations results for these three different diameters, and it is worth to notice that, as the waist diameter increases the spectral interference pattern moves to longer wavelengths which agree with the experimental results of the section 2.1.4.

In order to match the experimental and numerical results, it is necessary to include the higher cladding modes, material constituents of the fiber, and its material dispersion. For this simulation we assumed a fiber with 1.76/62.5 μm core cladding radius, a 0.2 numerical aperture, and an external refractive index of 1, close to the parameters of a 980 HP fiber from NUFERN.

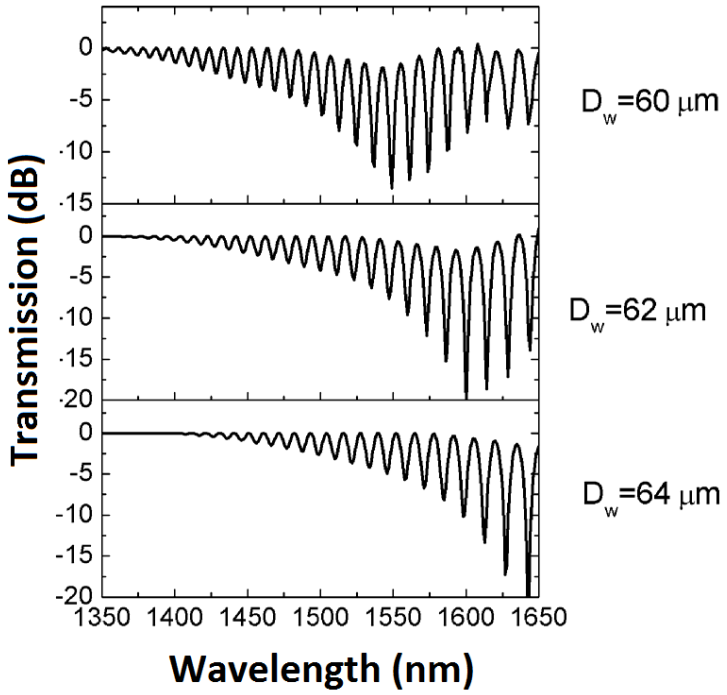

Fig. 2.2. Calculated transmission spectra of three MZFI with different taper waist diameter D_W, keeping L_T = 2.5 mm, L_w = 1mm, L = 2 cm, and D = 125 μm.

The effective indices of the core and cladding for every z value were calculated in steps of 1μm, in a range of wavelengths with steps of 1 nm, for the taper transitions and waist. Then the corresponding coupling coefficients for those values were calculated, and finally the coupled equations were solved using a Runge-Kutta algorithm for each wavelength. In appendix A it is shown in a Mathematica code the general procedure used for the simulation.

Fig. 2.3 shows the simulation for an optical fiber tapered at several tapered lengths (at the end of the first down-transition taper (a), at the end of the first waist (b), at the end of the first up-transition (c), at the end of the separation between tapers (d), at the end of the second down-transition (e), at the end of second waist (f), and at the end of the second up-transition (g)) for an optical fiber tapered with the dimensions being transition length 1 mm, waist length 1 mm, waist diameter of 65 μm and a separation between tapers of 10 mm.

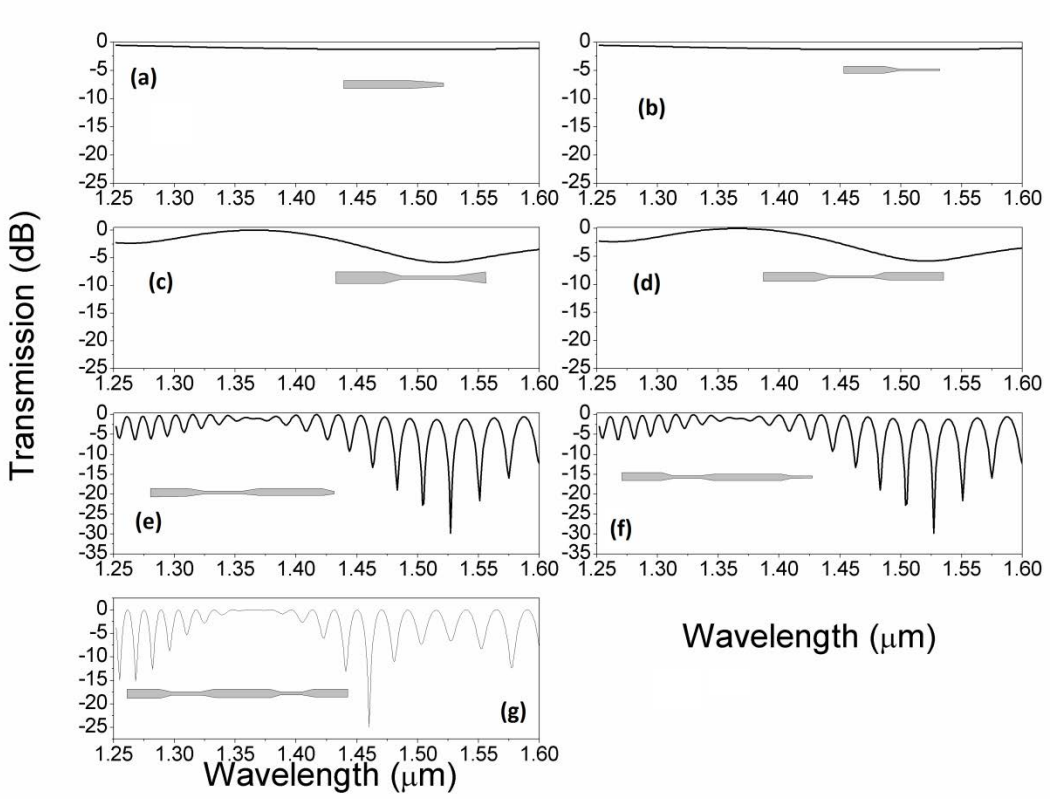

Fig.2.3. Calculated transmission spectra of an optical fiber device with two optical fiber tapers at different lengths (at the end of the first down-transition taper (a), at the end of the first waist (b), at the end of the first up-transition (c), at the end of the separation between tapers (d), at the end of the second down-transition (e), at the end of second waist (f), and at the end of the second up-transition (g)).

2.1.3 Fabrication of the Mach-Zehnder interferometer

It was shown in Fig. 2.1 the structure of the MZFI, for the taper fabrication. A glass processor system Vytran 3400 was used, which allows a precise control of the taper geometrical shape profile (D_W, L_W, and L_t). The fusion power was set to 39.9 W and the pull velocity to 1.5 mm/s.

A simple transmission set up was used to measure the optical transmission signal during the tapering process, a white source (WLS) model AQ4305 from Yokogawa and an optical spectrum analyzer (OSA) model AQ6370B from Yokogawa. Before tapering the fiber in the glass processing system, the coating of a section of the fiber was removed by stripping mechanically and then cleaned in an acetone ultrasonic bath.

In all of the MZFIs fabricated, it was measured and recorded the transmission signal of the fiber before and after the fabrication of the first and second taper. The transmission spectra after the first and the second taper are shown in dashed and continuous line, respectively.

2.1.4 Effect of the geometrical parameters of the MZFI on the fiber-comb-filter transmission spectrum.

In this section the effects of the geometrical MZFI parameters (L, D_W, L_W, and L_t) over the transmission spectral characteristics of the fiber-comb-filter are discussed with the principal purpose of identify the overall effect of every parameter to construct fiber-comb-filters with the desired parameters. In order to know these effects, individually, every parameter was varied keeping the others fixed, in order to observe directly its effect in the transmission spectrum. The variation of each parameter was made without using a specific rule. However, for another cases where an optimization process is required to reach a given transmission profile, optimization procedures can be implemented on the manufacture process. In the following sections experimental results of every parameter variation are shown.

2.1.4.1 Effect of the distance between tapers, L

In a typical MZFI, the increase in the taper separation will reduce the period of the interference pattern [8]. In order to experimentally prove this, several samples were fabricated varying the distance L, and keeping the other taper dimensions at the values of L_T = 2.5 mm, L_W = 1mm, and D_W = 60 μm. Fig. 2.4 shows the transmission spectra of three MZFIs with 5, 10, and 20 mm of separation length between the two tapers. It can be noted that this spectra behavior is similar to that reported for MZFI based on two LPGs [8]. But in our case, the maximum loss peak is quite smaller ($\sim 5dB$), the insertion loss are lower (0.5 dB), and the modulation band transmission width is one order of magnitude larger.

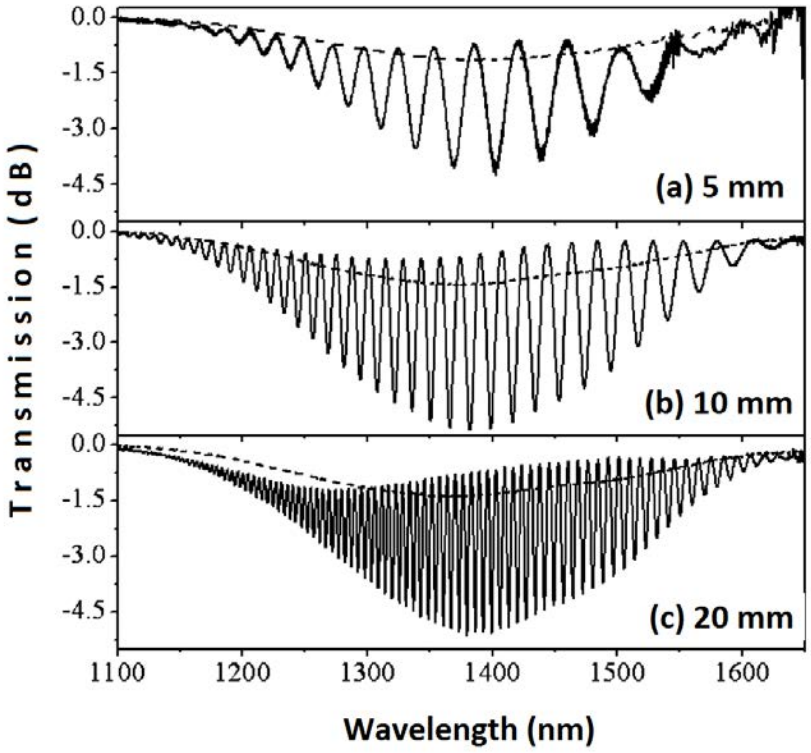

Fig. 2.4 Transmission spectra of three MZFI with distance between tapers of (a) 5, (b) 10, and (c) 20 mm, keeping L_T = 2.5 mm, L_w = 1mm, D = 125 μm, and D_w = 60 μm.

The corresponding period for the MZFIs with 5, 10, and 20 mm were 36.12, 19.0, and 7.145 nm. Taking in consideration these values, it is clearly noticed that when the taper separation is increased twice, the period is halved proportionally. Speaking about the fringe bandwidth, it also follows a similar proportion, it reduces from 10 nm, for a distance of L = 5 mm, to 5.10 and 2.15 nm when L increases to 10 and 20 mm, respectively. Using lengths larger than 200 mm, it is possible to reduce the fringe bandwidth to values smaller than 1 nm, however it could be impractical for real-world applications. As it can be seen from Fig. 2.4 the wavelength band and the visibility of the filter did not experience a significant change.

2.1.4.2 Effect of the taper waist diameter

In order to know the effect that has this parameter on the MZFIs, keeping the parameters L_W = 1 mm, and L_T = 2.5 mm, several MZFI devices with the taper waist diameter (D_W) of 100, 90, 80, 70, 60, 50, 40, 30, and 20 μm, separated by a distance L = 10, and 20 mm, were fabricated. Fig. 2.5 shows two of the MZFI, with a D_W of 60, and 65 μm and a separation distance of 20 mm.

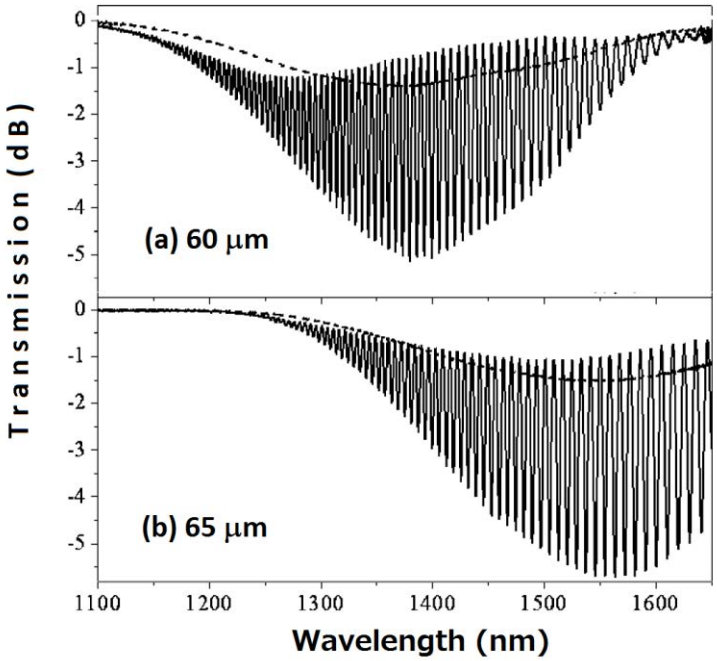

Fig. 2.5. Transmission spectra of two MZFI consisting of two identical tapers with a taper waist diameter of (a) 60 and (b) 65 μm, with a separation between tapers of 20 mm, and keeping L_T = 2.5 mm, D = 125 μm, and L_w = 1mm.

When it is compared both spectra in Fig. 2.5, it can be observed that the effect of varying this parameter on the MZFI transmission spectrum is the shift in the position of the interference pattern, when the fiber taper waist diameter decreases from 65 to 60μm the pattern shifts towards shorter wavelengths, just as this behavior was illustrated in the theoretical spectrum of Fig. 2.2.

When the waist diameter is 60 μm the deepest fringe is located around 1391 nm with a deep of 5 dB, but when the waist diameter is 65 μm the deepest fringe is shifted to around 1550 nm with a deep of 5.5 dB. Another effect to vary the waist diameter is a small change in the visibility of the interference pattern, it is lower for smaller waist diameter.

The effects of the other geometrical parameters (waist length, transition length taper separation) have a small contribution on the position of the interference pattern; however it was found that the waist diameter has the biggest contribution to the position of the interference pattern.

When the taper waist diameter is bigger than 70 μm, the amount of coupling energy is negligible, it means that the tapers are adiabatic and there is not noticeable interference. On the other hand, when the waist diameter is smaller than 50 μm, the insertion losses increase and they can be as high as 15 dB, as the taper waist diameter of the first taper decreases the taper become more non-adiabatic and the fraction of light that is coupled from core to cladding increases, but at the second identical taper, only some of the cladding light is recoupled to the core, as a result of this, the insertion loss increases and the visibility is poor.

2.1.4.3 Effect of the waist length, L_W

In order to know the effect of this parameter on the spectrum transmission of the MZFI, several samples with two identical fiber tapers in series with a waist lengths in the range from 0.5 to 6.5 mm, while the rest of the parameters was kept as D_W = 60 μm, L_t = 2.5 mm, and L = 1 cm. Fig. 2.6 shows the spectra for four MZFI with waist lengths of 1, 3, 4.5, and 6.5 mm.

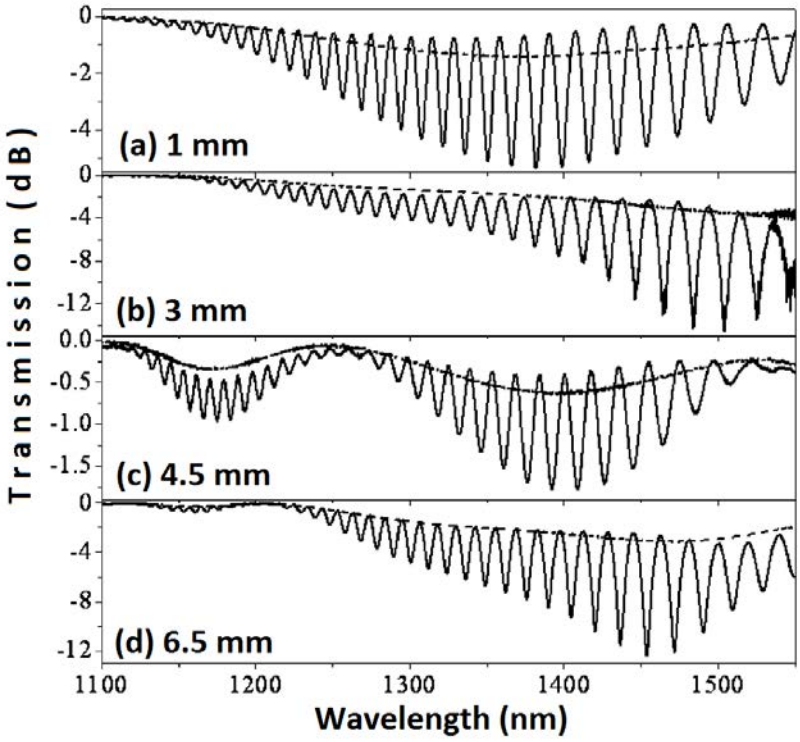

Fig. 2.6. Transmission spectra of four MZFI consisting of two identical tapers with a taper waist length of (a) 1, (b) 3, (c) 4.5, and (d) 6.5 mm, the separation between tapers of 10 mm, L_T = 2.5 mm, D = 125 μm, and D_w = 60 μm.

The main variation of this parameter on the transmission spectrum is the fringe visibility, which is related to the optical path that follows the core and cladding modes when they are propagating through the waist length in both tapers.

Due to the fact that the coupling coefficient is zero in the waist length the only thing to be affected by the waist length is the phase shift experienced by both the fundamental core mode and the higher order cladding modes, before they are affected by the coupling in the next taper transition. As a result of this phase shift, the degree of the interference is affected and it is reflected in a change of the fringe visibility as it can be seen in the spectra of Fig. 2.6.

2.1.4.4 Effect of the taper transition length

The length of the taper transition length is the first responsible for the amount of coupling between the core mode and high order cladding modes, and the effect is reflected in the size of the interference pattern, i.e., the extension of the interference pattern. When the taper transition length is decreased the diameter change is more abrupt, it means it is less adiabatic, as a consequence more energy of the core is coupled to high order cladding modes. Fig 2.7 shows the spectra for taper transition lengths of 1, 1.5, 2, 2.5, 3, and 3.5 mm.

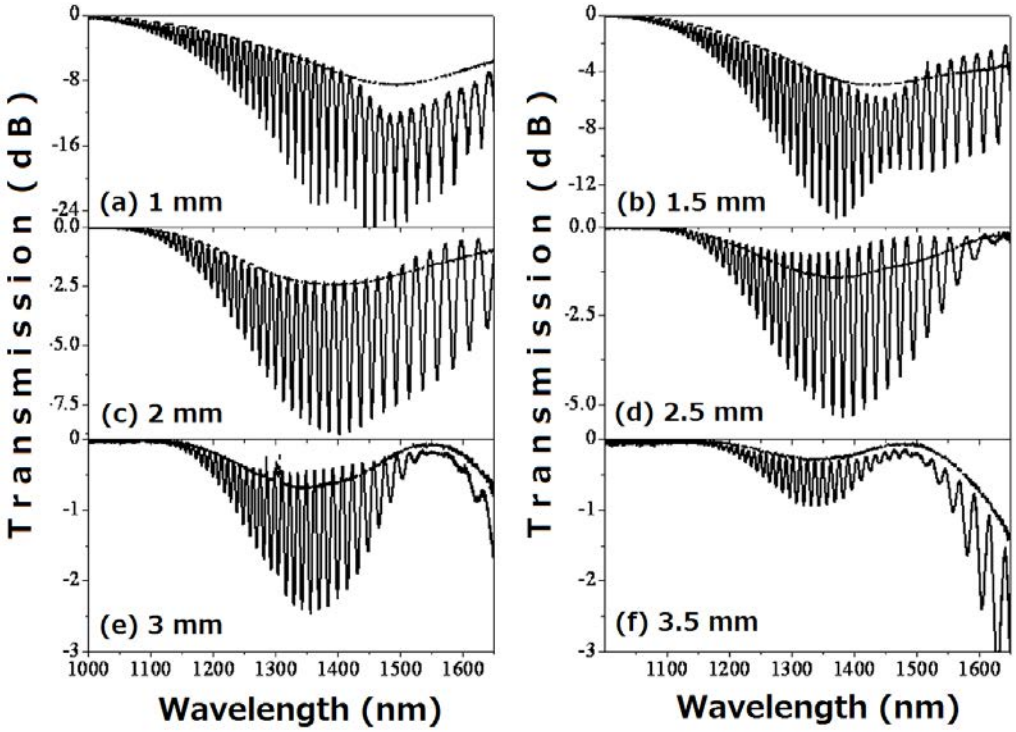

Fig. 2.7. Transmission spectra of six MZFI consisting of two identical tapers with a taper transition length of (a) 1, (b) 1.5, (c) 2, (d) 2.5, (e) 3, and (f) 3.5 mm, L_w = 1 mm, L = 1 cm, D = 125 μm, and D_w = 60 μm.

From Fig. 2.7 it can be seen that as the transmission length increases, the spectral bandwidth of the interference patterns becomes narrower. The extension of the interference pattern is narrower when the transitions are more adiabatic, that is, there is less coupled energy to the high order cladding modes, and vice versa, as the taper transition length decreases, the extension of the interference pattern augments because the coupled energy is larger.

For smaller taper transitions than 2.5 mm the transmission spectra seem to be composed of two interference patterns which differ in their average period and they overlap in the spectral region around 1450 nm.

The taper transition length also affects the fringe visibility, as the taper transition increases, the fringe visibility decreases for a spectral region around 1450 nm, and at the same time the period of the fringes is more homogeneous.

Due to the fact that the two geometrical parameters, transition length and waist length, which are directly responsible for the fringe visibility of the interference pattern, both of them need to be optimized to get the right visibility value for a certain MZFI application. In fact, a similarity is observed in the spectral interference pattern evolution with the increase of the waist length or transition length.

It is necessary to notice that each taper separately acts as an interferometer, where the period of the interference fringe is mainly determined by the waist length, and the core and cladding modes develop independently a different phase shift. Thus, the single taper interferometer length should be at some point inside the taper transition, where the second mode (cladding mode) is already present. Thus, for long enough lengths a second broad spectral fringe will be observed after the first taper, in all the fabricated samples the narrower interference fringes are presented after the second concatenated taper.

2.1.5 Refractive index sensitivity of the fiber comb-filter

The fiber could be weakened after the tapering process, in order to avoid this weakening, the comb filter based on tapers should have to be embedded into a solid protection matrix that in general has a RI higher than 1. Due to the fact that the MZFI is based on the propagation and excitation of cladding modes, a protective material at the surrounding of the cladding may affect the filter behavior. Thus, it is mandatory an analysis of the sensitivity to surrounding RI changes that has the MZFI. To make this analysis, a fiber section of 20 mm, including both tapers where immersed in Cargille oils with a calibrated RI ranging from 1.36 to 1.436. Fig. 2.8 shows the transmission spectra of a concatenated taper pair with the geometrical dimensions of L_T = 2.5, L_W =1 mm, L = 1cm and D_W = 60 μm. Immersed in Cargile oils of 1 (black line) and 1.436 (red line), where it can be noticed that the fringe visibility only changes when the surrounding refractive index is close to the cladding refraction index, hence, the taper pair device can be packaged without significant modification of its spectral transmission characteristics.

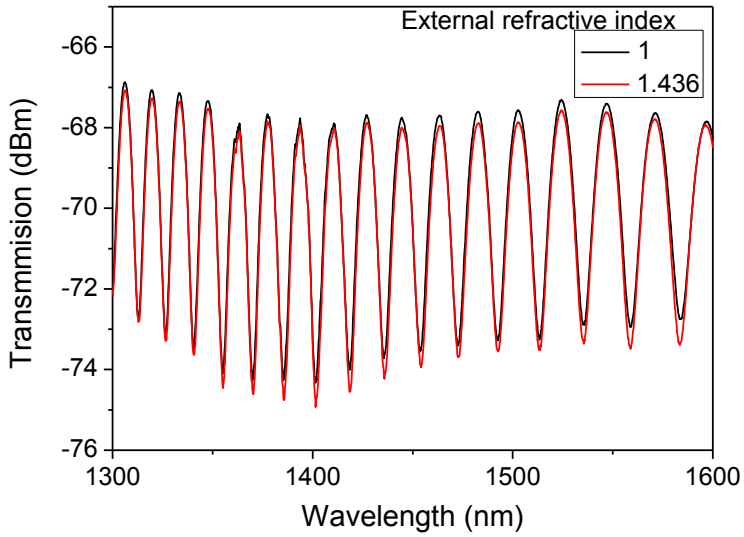

Fig.2.8. Transmission spectrum of aMZFI consisting of two concatenated tapers with a L = 2.5 mm, L_W = 1 mm, L = 1 cm and D_W = 60 m, when it is surrounding by air (black line, RI = 1) and a Cargille oil with a nominal refractive index of 1.436 (red line).

2.1.6 Discussion

So far, the effect of varying the geometrical parameters in the concatenated pair interferometer has been discussed. It was also discussed the modeling of an interferometer with specific geometrical parameters. Nevertheless, the mechanism that leads to the observed interference pattern when it is changed a specific geometrical parameter has not been discussed. In order to discuss this mechanism it is necessary to look at the transmission spectrum after the first taper, as it can be seen from the spectra reported so far, a broad sine-like modulation appears in the spectrum after the first taper, which is a common behavior observed in single tapers [16]. So the concatenated taper device may be seen as two concatenated single taper interferometers. The effective length of the single-taper interferometer can be changed if the waist diameter, waist or transition length is varied, thus allows the transmission spectrum tailoring that of the two-tapers device. It is worth to mention that both of the changes in the transition length and waist diameter change the transition taper angle, so that, different combinations of transition length and waist diameters result in the same transition taper angle. However, even having two different combinations of transition length and waist diameter which produce the same transition taper angle, the length of the coupling zone will result in a modification of the effective length of the single-taper interferometer, causing different spectra for devices with the same transition angle taper.

As it is known, due to the photo-elastic and photo-thermal coefficient, there is a change in the refractive index, since the tapered fiber devices are also sensitive to stress and temperature. In

order to know the temperature sensitivity of the MZFI, it was tested by performing spectrum measurements at different temperatures on the MZFI in a range from 0 to 60^{O} C, observing similar slight changes in the fringe visibility as the case of different surrounding refraction index (Fig. 2.8). For a real world application the effect of the temperature can be compensated or isolated. Variations in visibility were also detected by bending. For very small bending radii, the visibility variations were small, however, after certain limit there was a relatively big variation in visibility. In order to know the bending sensitivity, the displacement was taken as a measurement of bending sensitivity because small bending radii are difficult to measure. For this purpose the concatenated taper pair device was mounted in a flexible sheet that was fixed on one end, while the other end was mounted on a translation stage coupled with a stepper motor. A simple transmission set up was used to measure the spectrum transmission of the taper pair device, using as a source a single-frequency highly stable tunable semiconductor laser, and as a detector a high sensitivity low noise photodetector. After a displacement of 200 μm, the measured power started to demonstrate considerable changes. Fig 2.9 shows these of this power changes that were captured by a computer interface.

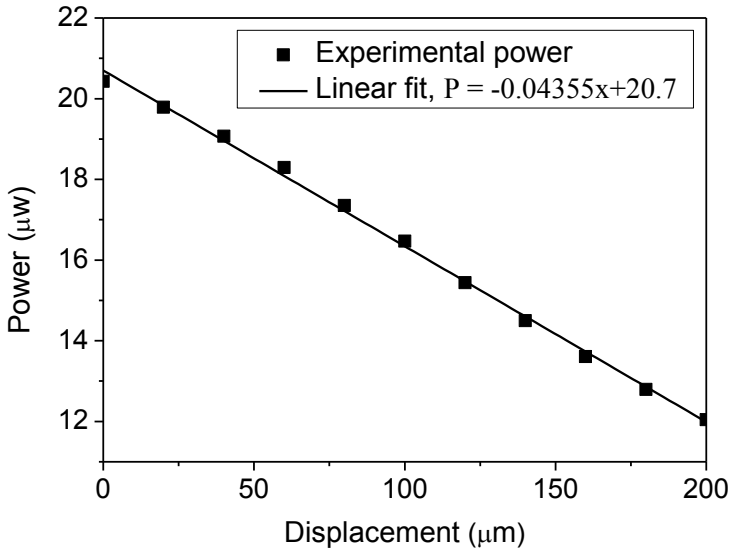

Fig.2.9. Transmitted power as a function of displacement at a wavelength of 1552.5 nm.

The taper parameter used for the displacement characterization of Fig. 2.9 were L_t = 2.5 mm, L_W = 1 mm, L=1 cm, and D_W = 60 μm while the laser source was set at 1552.2 nm. As it can be seen the MZFI shows high sensitivity to bending with a factor of 0.04255 μW/μm, so that, the MZFI can be treated as a micrometer displacement sensor.

2.2 Compact optical fiber curvature sensor based on concatenating two tapers

An optical fiber curvature sensor with low-loss, compact and high sensitivity was fabricated. It consists of two identical low-loss optical fiber tapers separated by a distance L. These tapers are adiabatic when they are kept straight and fixed, so that, no interference pattern appears when the optical fiber device is straight. However, ones the device is bent, the adiabatisity of the device starts to gradually break because of the symmetry of the straight tapers is lost, and the first taper starts to couple light into cladding modes, then a fraction of the cladding modes is recoupled when they reach the second taper, and as a result, an interference pattern in the transmission spectrum is generated, and its visibility magnitude depends of the amount of bending radius that the device maintains. The dynamic range of the device can be tailored by a proper selection of the taper diameter or the separation between tapers.

2.2.1 Introduction

For this device, we used the same MZFI structure as the one used in section 2.1, with the difference that now we call the waist diameter as ρ_w, which consists of two coupling devices separated by an optical fiber with a distance L. As in the case of the previous section, the coupling devices are optical fiber tapers. However, countless MZFI configurations with different coupling devices have been reported so far. Optical fiber mode coupling devices as long period gratings (LPGs) and abrupt fiber tapers have been widely used to construct MZFI sensors [17-20]. Speaking about abrupt tapers, they can be fabricated in almost all kind of fiber using a homemade tapering machining or even a standard fusion splicer machine. The easy fabrication of these abrupt optical fiber tapers has been exploited to construct highly sensitivity refraction index sensors [20]. Nevertheless, the use of these devices was restricted to applications where at least one taper needed to be kept straight and fixed for the device to work well. A MZFI for bending measurement has been reported by Frazao et al. [21]; however the author used a LPG and multimodal interference structure. In this work, we used a MZFI based on two identical fiber tapers to construct a highly sensitive bending sensor. These two tapers behave as adiabatic tapers when they are straight, so, under the straight device condition no interference pattern appears in the transmission spectrum, but when the device is bent the tapers adiabaticity starts to gradually disappear, causing the generation of an interference pattern in the transmission spectrum. The interference fringe of this interference pattern is directly related to the fiber bending radius.

2.2.2 Construction of the bending sensor

The fiber optic structure used to the construction of the bending sensor is shown in Fig. 2.10. It is similar to that shown in fig 2.1

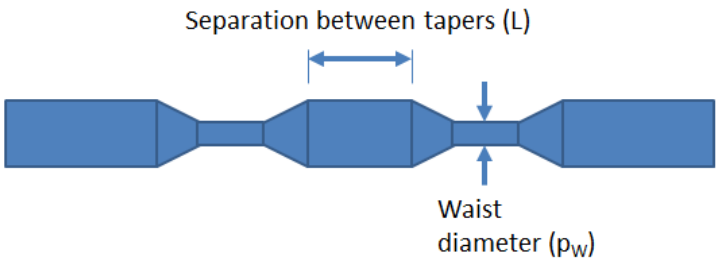

Fig.2.10. MZFI based on two tapers.

Using a glass processor system Vytran 3400 the optical fiber tapers were made. The transmission spectrum of a fabricated device with waist diameter equal to 60 μm, waist length of 1 mm, transition lengths of 2.5 mm, and a separation length of L = 10 mm is shown in Fig. 2.11, the dashed line shows the spectrum after the first taper, and the dotted line shows the spectrum after the two tapers. As it can be noticed no modulation appears in the transmission spectrum and the attenuation of the two tapers is approximately 0.3 dB, which is a very small value and means that the tapers are almost adiabatic.

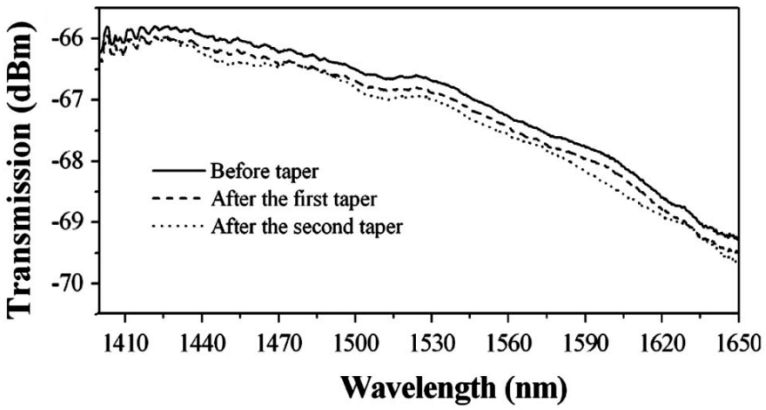

Fig.2.11. Fiber transmission spectrum before tapering (continuous line) and after fabrication of the first (dashed line) and second (dotted line) tapers. Tapers are identical, with ρ_w = 60 μm, and separated by a distance L = 10 mm.

Tapers with waist diameters (ρ_w) of 60 and 50 μm, a waist length of 1 mm and transition lengths of 2.5 mm were fabricated in standard SMF-28 fiber. Then several MZFI were fabricated by concatenating a pair of tapers separated by distances of 5, 10, 20, and 40 mm.

The set up for bending characterization is shown in Fig. 2.12. The MZFI were mounted on a v-groove made in a thin sheet of metal of 315 mm in length. Then using the set up every MZFI was tested to bending. Parameters 2S and d were used to calculate the bending radius using the well-known relationship $1/R=2d/(d^2+S^2)$ [22].

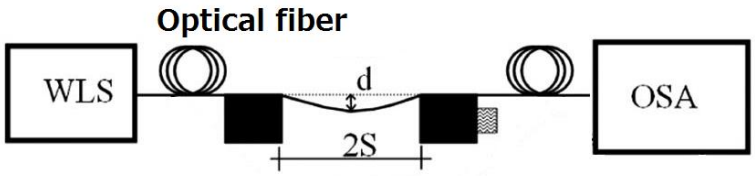

Fig.2.12. the experimental setup for the bending tests.

2.2.3 Working mechanism of the bending sensor

As the structure sensor is the same as the previous section, the working mechanism of this device is exactly the same as the section 2.1.2, as follows: when the light propagates through the down taper transition of the first taper, the fundamental core mode transfer energy into higher order cladding modes, with the same azimuthal symmetry because the taper is axisymmetric [23]. Then both fundamental core and high order cladding modes will propagate through the taper waist, and then, when the light arrives to the up taper transition the high order cladding mode will be coupled to the fundamental core mode. When the light is going through the second taper the same process is repeated, and the transmission interference pattern of the device will depend on the amount of light that is propagated in the cladding of the fiber section between tapers. When there is no cladding light in the section between tapers, there is no interference pattern which is the case when the fiber tapers are kept straight (see Fig. 2.11). But when the MZFI is being bent the refractive symmetric index profile is starting to break, permitting the coupling between the fundamental core and cladding modes which propagate as whispering gallery (WG) modes [24]. Then in the optical fiber section that separate the tapers, the core and WG modes will propagate and they will generate a phase delay, then at second taper, the WG modes will recouple to the core mode, and the interference degree will be determined by the geometrical and elasto-optic changes in the refraction index profile which are related with the MZFI bending radius.

2.2.4 Experimental results

In order to see the change in the interference pattern, Fig 2.13 shows the transmission spectra of two MZFI with a waist diameter of 60 um and a separation distance of 5 (bottom graphs) and 40 mm (upper graphs) for three different curvature radii (0.916, 0.535, and 0.320 m).

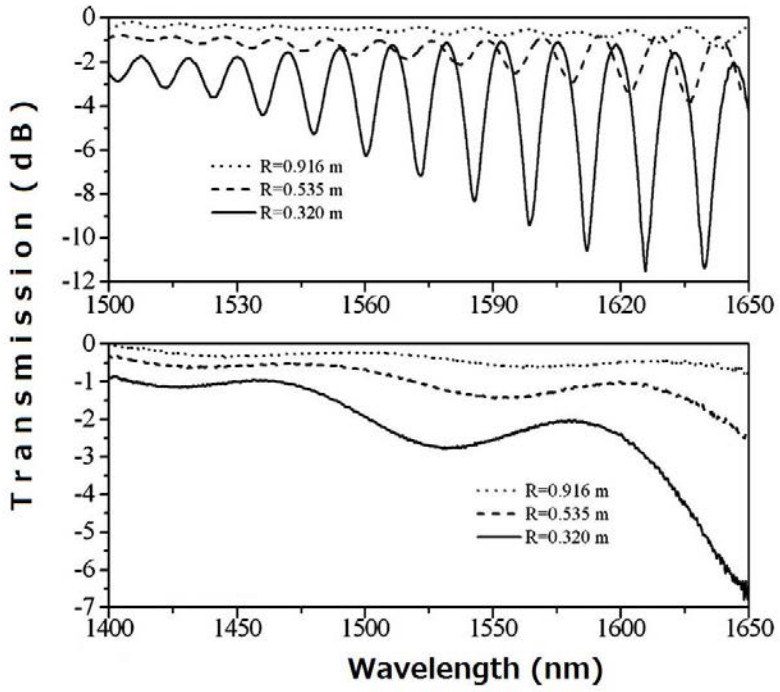

Fig.2.13. MZFI transmission spectra when tapers are separated by a distance of 40 mm (upper graphs) and 5 mm (bottom graphs) for three different bending radii.

From Fig. 2.13, it can be seen that the amplitude modulation is dependent on the curvature bending radius of the fiber and another thing to mention is that the modulation amplitude of the spectra is larger for longer wavelengths because the mode coupling is higher at those wavelengths when the fiber is bent. The presence of losses is due to cladding modes that cannot be recoupled back to the core and cladding modes excited by the second taper. There is an increment of those losses when the bending radius increases, however, even for small bending radius, the insertion losses are small. The spectra also experience a blue shift due to the fiber bending and the period fringe remains almost constant.

Observing Fig. 2.13 the MZFI can be used as an intensity modulated bending sensor or as in-line optical fiber variable attenuator

Fig. 2.14 shows the relationship between fringe separation and taper separation; on the right side, it is shown the inverse of taper separation versus fringe separation, which shows a linear behavior.

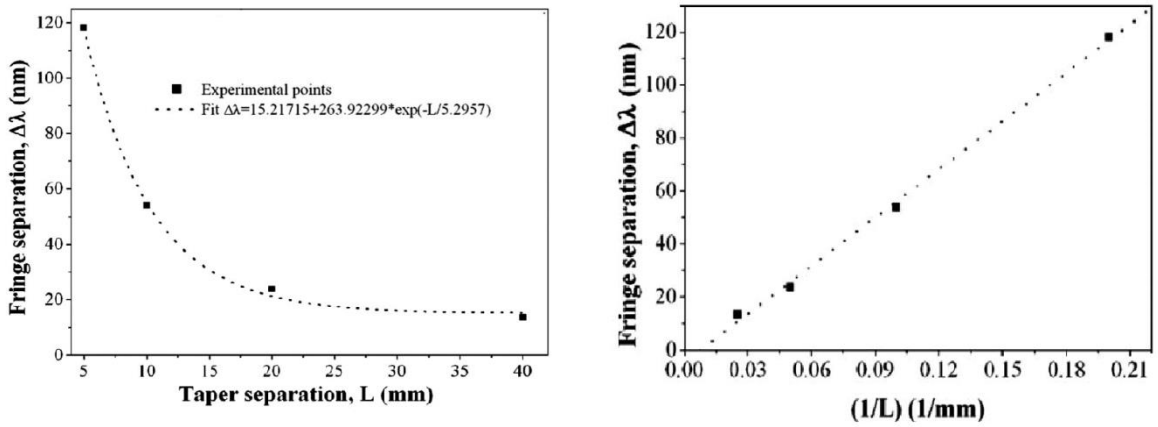

Fig. 2.14. Relationship between taper separation and interference fringe separation of the two-taper MZFIs fabricated. To the right, inverse of taper separation versus interference fringe separation.

In order to evaluate the quality of the fringe pattern, determined mainly by the bending radius, the fringe visibility was calculated by the well-known relationship $V = \frac{I_{\min}^{up} - I_{\min}^{low}}{I_{\min}^{up} + I_{\min}^{low}}$ where $I_{\min}^{up}$ and $I_{\min}^{low}$ are the minimums of the upper and lower envelopes of the transmission spectra, respectively [25, 26].

Fig. 2.15 shows the visibilities for a bending radius ranging from 2.75 to almost zero, for MZFI with 5, 10, and 40mm of separation between tapers, keeping the transition lengths at 2.5 mm, the waist length at 1 mm and the waist diameter at 60 um. Fig. 2.16 shows the visibilities for 60 and 50 μm of waist diameter, keeping the separation between tapers at 10 mm, the transition lengths at 2.5 mm, and the waist length at 1 mm.

When the MZFI was straight the transmission spectrum has no modulation interference, so that, fringe visibility can be considered as zero and it can be used as a zero bending condition in the sensors calibration process.

As it can be seen from Fig. 2.15 and 2.16 the visibility of the fringes grows exponentially as the bending radius decreases. From Fig. 2.15 for the three different separations between tapers, considering that the limiting value of the visibility is the unity, it is inferred that the shorter MZFI are adequate to measure small curvature radii, while bigger MZFI are adequate to measure bigger diameters, so, the sensible dynamic range of the sensor can be tailored.

Another way to change this dynamic range is by means of changing the waist diameter of the tapers. Fig. 2.16 it shows that when the waist diameter of the fiber tapers are reduced the dynamic range of the MZFI is shifted to larger curvature radius.

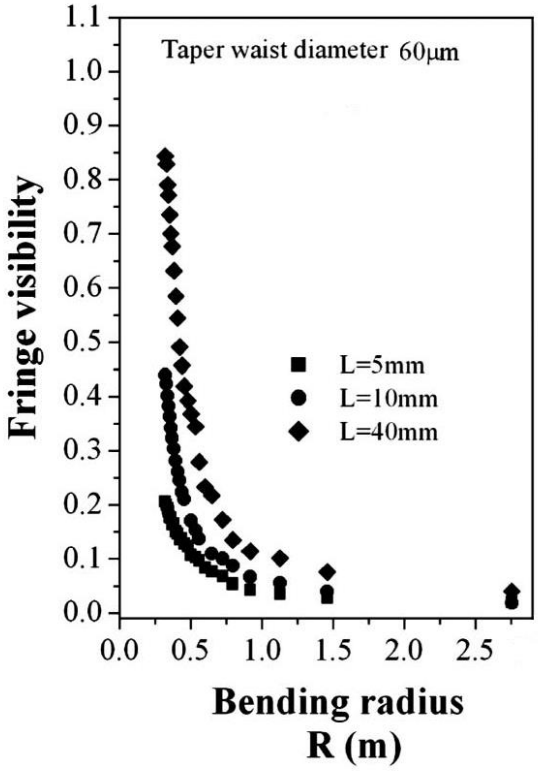

Fig. 2.15. Fringe visibility versus curvature radius of MZFIs formed with (a) two tapers with ρ_w = 60 μm and the L = 5 (squares), 10 (circles), and 40mm (diamonds),

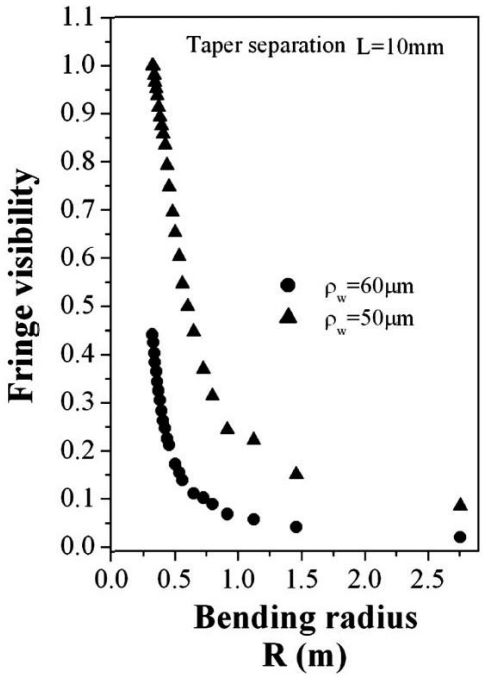

Fig. 2.16 Two tapers with ρ_w = 60 (circles) and 50 μm (up-triangles) and L = 10 mm.

When the sensor MZFI was bent in opposite directions, we observed variations in the transmission spectrum when the bending radius was exactly the same, but the bending direction was opposite. This variation could be caused because of slight variations in both of the tapers profile. Nevertheless, this effect can be exploited to identify the bending direction of the MZFI.

For practical applications, due to the weakening caused by tapering of the fiber, it is necessary to protect the fiber in order to make it robust. So that the MZFI should have to be embedded in a solid protection matrix with a refractive index higher than 1; this could disturb the MZFI because its working principle is based in cladding modes. Fig. 2.17 shows the transmission spectrum of a MZFI, with a waist diameter of 60 μm and a separation between tapers of 10 mm, immersed in Cargille oils with a calibrated refraction index of 1.402 (dashed line), and 1.442 (dotted line). The original spectrum is shown by a continuous line (device without surrounding refractive index).

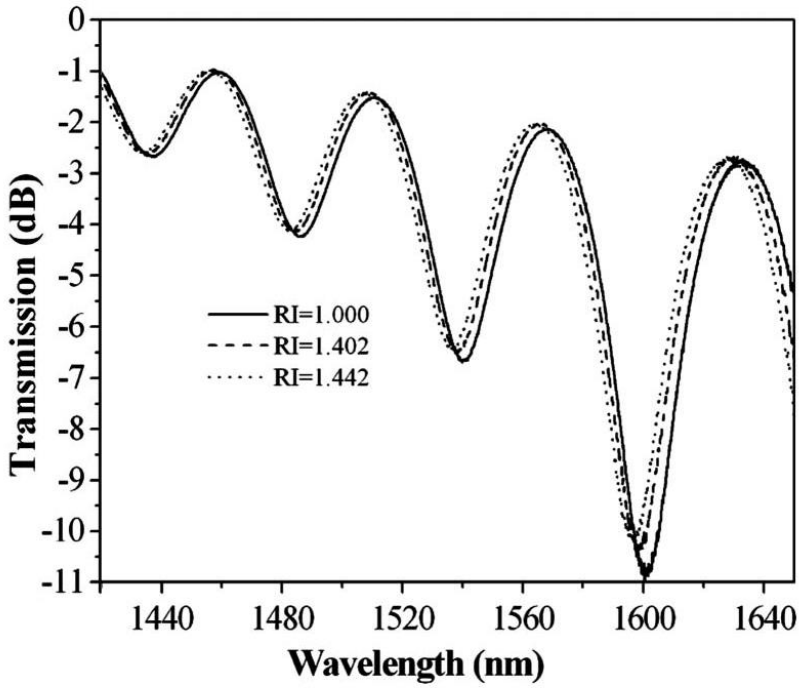

Fig. 2.17. Transmission spectra of the MZFI formed with two tapers with ρ_w = 60 μm and L = 10mm for three different RIs, with a bending radius of 0.2 m.

It is observed that the interference fringe visibility slightly decreases and shifts to shorter wavelengths as the RI augments. These small changes do not affect the general performance of the MZFI, so that, the device can be embedded into a protective matrix.

The effects of the changes caused by the temperature on the MZFI were also analyzed, and it was found that in the range from 20 – 45^{o}C there was no change in the visibility of the interference pattern, and only the pattern was shifted by 2 nm towards longer wavelengths.

2.3 References

[1] Y. W. Lee, K. J. Han, B. Lee, and J. Jung, “Polarization-independent all-fiber multiwavelength-switchable filter based on a polarization-diversity loop configuration,” Opt. Exp., vol. 11, no. 25, pp. 3359–3364, 2003.
[2] Z.-C. Luo, A.-P. Luo, andW.-C. Xu, "Tunable and switchable all-fiber comb filter using a PBS-based two-stage cascaded Mach–Zehnder interferometer," Opt. Commun., vol. 284, pp. 4167–4170, 2011.
[3] A.-P. Luo, Z.-C. Luo, W.-C. Xu, and H. Cui1, "Wavelength switchable flat-top all-fiber comb filter based on a double-loop Mach-Zehnder interferometer," Opt. Exp., vol. 18, no. 6, pp. 6056–6063, 2010.
[4] N. Q. Ngo, D. Liu, S. C. Tjin, X. Dong, and P. Shum, "Thermally switchable and discretely tunable comb filter with a linearly chirped fiber Bragg grating," Opt. Lett., vol. 30, no. 22, pp. 2994–2996, 2005.
[5] H. L. An, X. Z. Lin, E. Y. B. Pun, and H. D. Liu, "Multi-wavelength operation of an erbium-doped fiber ring laser using a dual-pass Mach–Zehnder comb filter," Opt. Commun., vol. 169, pp. 159–165, 1999.
[6] P. Wang, G. Brambilla, M. Ding, Y. Semenova, Q. Wu, and G. Farrell, "The use of a fiber comb filter fabricated by a CO laser irradiation to improve the resolution of a ratiometric wavelength measurement system," J. Lightw. Technol., vol. 30, no. 8, pp. 1143–1149, Apr. 2012.
[7] Z.-C. Luo, W.-J. Cao, A.-P. Luo, and W.-C. Xu, "Polarization-independent, multifunctional all-fiber comb filter using variable ratio coupler- basedMach–Zehnder interferometer," J. Lightw. Technol., vol. 30, no. 12, pp. 1857–1862, Jun. 2012.
[8] K. M. Evoy and D. N. Nikogosyan, "Realization of periodic transmission filter based on a pair of cascaded long-period fiber gratings of different strength/wavelength position," Opt. Laser Technol., vol. 44, pp. 683–687, 2012.
[9] X. Wang, Y. Li, and X. Bao, "C- and L-band tunable fiber ring laser using a two-taper Mach–Zehnder interferometer filter," Opt. Lett., vol. 35, no. 20, pp. 3354–3356, 2010 .
[10] B. Li, L. Jiang, S. Wang, J. Yang, M. Wang, and Q. Chen, "High sensitivity Mach-Zender interferometer sensors based on concatenated ultra-abrupt tapers on thinned fibers," Opt. Laser Technol., vol. 44, pp. 640–645, 2012.
[11] O.Frazão,P.Caldas, F.M.Araújo,L.A.Ferreira, and J.L.Santos, “Optical flowmeter using amodal interferometer based on a single nonadiabatic fiber taper,” Opt. Lett., vol. 32, no. 14, pp. 1974–1976, 2007.
[12] J. Bures, Guided Optics: Optical Fibers and All-Fiber Components. Weinheim, Germany: Wiley-VCH, 2009.
[13] Guillermo Salceda-Delgado, Alejandro Martinez-Rios, and David Monzon-Hernandez, “Tailoring Mach-Zehnder Comb-Filters Based on Concatenated Tapers”, Journal of Lightwave Technology, Vol. 31, No. 5, March 1, 2013.

[14] J. D. Love, W. M. Henry, R. J. Black, S. Lacroix, and F. Gonthier, “Tapered single-mode fibres and devices. Part 1: Adiabaticity Criteria,” Proc. IEEE, vol. 138, no. 5, pp. 343–354, May 1991.
[15] A. W. Snyder and J. D. Love, Optical Waveguide Theory. London, U.K.: Chapman and Hall, 1983.
[16] D. T. Cassidy, D. C. Johnson, and K. O. Hill, “Wavelength-dependent transmission of monomode optical fiber tapers,” Appl. Opt., vol. 24,no. 7, pp. 945–950, 1985.
[17] X. J. Gu, “Wavelength-divicion-multiplexing isolation fiber filter and light source using cascaded long-period fiber gratings”, Opt. Lett. 23, 509 (1998).
[18] O. Frazão, R. Falate, J. L. Fabris, J. L. Santos, L. A. Ferreira, and F. M. Araújo, “Optical inclinometer based on a single long-period fiber grating combined with a fused taper”, Opt. Lett. 31, 2960 (2006).
[19] Z. Tian, S. S. Yam, J. Barnes, W. Bock, P. Greig, J. M. Fraser, H. Loock, and R. D. Oleschuk, “Refractive Index sensing with Mach-Zehnder interferometer Based on Concatenating Two Single-mode Fiber Tapers”, IEEE Photon. Technol. Lett. 20, 626 (2008).
[20] Y. Li, L. Chen, E. Harris, and X. Bao, “Double-Pass In-Line Fiber Taper Mach-Zehnder interferometer Sensor”, IEEE Photon. Technol. Lett. 22, 1750 (2010).
[21] O. Frazão, J. Villegas, P. Caldas, J. L. Santos, F. M. Araújo, L. A. Ferreira, and F. Farahi, “All-fiber Mach-Zehnder curvature sensor based on multimode interference combined with a long-period grating”, Opt. Lett. 32, 3074 (2007).
[22] W. Du, H. Tam, M. Liu, and X. Tao, Proc. SPIE 3330, 284 (1998).
[23] J. D. Love, W. M. Henry, W. J. Stewart, R. J. Black, S. Lacroix, and F. Gonthier, IEE Proceedings J. Optoelectronics 138, 343 (1991).
[24] L. Yao, T. A. Birks, and J. C. Knight, “Low bend loss in tightly-bent fibers through adiabatic bend transitions”, Opt. Express 17, 2962 (2009).
[25] E. H. Hecht, Optics (Addison-Wesley, 1987).
[26] D. Monzon-Hernandez, A. Martinez Rios, I. Torres-Gomez, and G. Salceda-Delgado, “Compact optical fiber curvature sensor based on concatenating two tapers”, Optics Letters, Vol. 36, No. 22, November 15, 2011.

Chapter 3
Modal device based on multicore fiber

Resume

In this chapter will be presented the experimental results that were obtained using a multicore fiber device based on a seven core fiber which was used to measure bending radius, which can be interrogated by either wavelength shift or visibility fringes.

3.1 Compact fiber-optic curvature sensor based on super-mode interference in a seven-core fiber.

An optical curvature sensor which shows low insertion loss and high sensitivity is presented. It is compact; it consists of a few millimeter long piece of seven-core fiber spliced between two single mode fibers. This kind of device has a pronounced interference pattern in its transmission spectrum, and when it is bent the interference pattern is shifted and the visibility of the interference fringes is altered. This sensor can be interrogated by visibility or spectral shift. Through the proper selection of the seven-core fiber length, it is possible to adjust the dynamic range of the sensor. Bending sensitivities of about 3000 nm/mm^{-1} were achieved.

3.2 Introduction

The measurement of curvature radius in structural monitoring applications is of great importance, an efficient way to measure this parameter is by using optical fiber sensors due to the unique characteristics they have, such as, their light weight, compactness, stability, fast response, high sensitivity, repeatability, insensitivity to electromagnetic interference, and so on. The most common optical fiber sensor is the one based on the Mach-Zhender interferometer [1-7]. To date, the presence of specialty optical fibers, such as photonic crystal fiber and multicore fiber, have a good impact for the sensing applications, [1, 7-10]. The sensors constructed by those specialty fibers have shown good performance, simplicity, and great sensitivity to several external parameters.

In this work, the unique light propagation characteristics in a multicore fibers (MCFs) are used to design and fabricate a bending sensor. A MCF supports the propagation of the so-called super-modes [11]. These super-modes are generated in the MCF structure by the energy coupling between light that propagates through the different cores, whose separation is small, making possible the interference between light carried by each core. These super-modes are very sensitive to external mechanical perturbations such as bending. Taking advantage of this sensitivity, it is possible to construct a robust and attractive multicore seven core fiber sensor.

3.3 Construction and working principle of the sensor

The construction of the sensor is based on a seven core fiber. It consists of a few millimeters of sensing fiber, in this case the seven core fiber, spliced between single mode fibers (SMF). Using this sensor structure, it is possible to construct a sensor without the necessity of using specialized equipment; it only takes the use of a fusion splicer machine to make the splices SMF-MCF. This is a good fabrication advantage compared with fabrication processes that require complex glass processing systems.

This kind of structure, a sensing fiber spliced between SMFs has been reported so far in previous works [1, 7, 8, 12-17], which proves that this structure is suitable for sensing applications. Insertion losses around 0.026 dB were registered for this MCF sensor.

The MCF used for the construction of this bending sensor is composed of seven cores doped with germanium, which are strongly coupled between them. Each core has a diameter of 9.2 μm and a NA equal to 0.132. They are separated each other by a distance of 11 μm, and the cladding diameter is 125 μm. In previous experiments this fiber has been used [18, 19] for temperature and optimization of the spectral characteristics. Fig. 3.1 shows the structure of the sensor with the single mode and seven core fiber cross sections obtained with a microscope. Typical insertion losses through the complete device are around 0.026 dB.

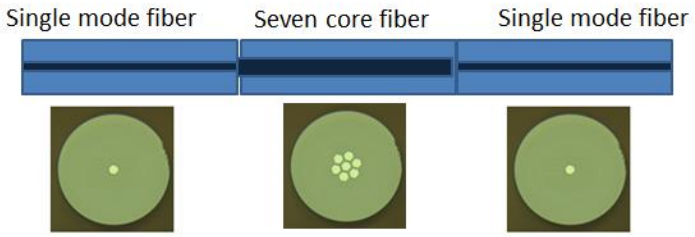

Fig. 3.1. Structure of the sensor (MCF spliced between two SMFs), and fiber cross-section of the MCF used to construct the sensor.

Using a finite difference method mode solver, we obtained the intensity profile of the super-modes supported by the seven core fiber. Fig. 3.2 shows the seven core fiber structure that was used to simulate the super mode electric field distributions. And from Fig. 3.3 to Fig. 3.9, the electric field distribution of every super-mode is shown.

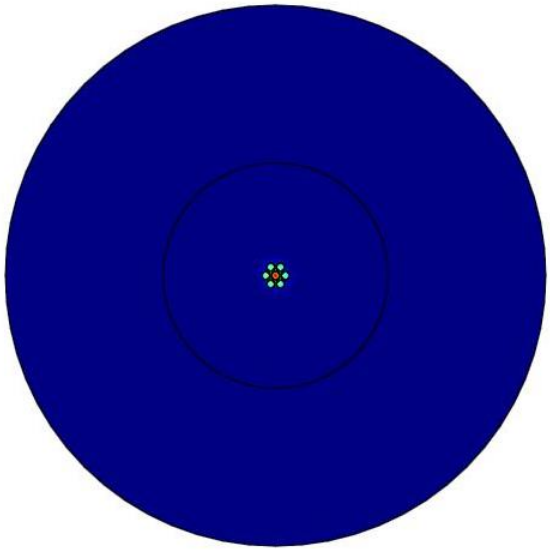

Fig. 3.2. Seven core fiber structure used to make the simulate super-modes density profiles with the geometrical parameters: core diameter 9.2 μm with a NA of 0.132, a core-to-core separation of 11 μm, and a cladding diameter of 125 μm.

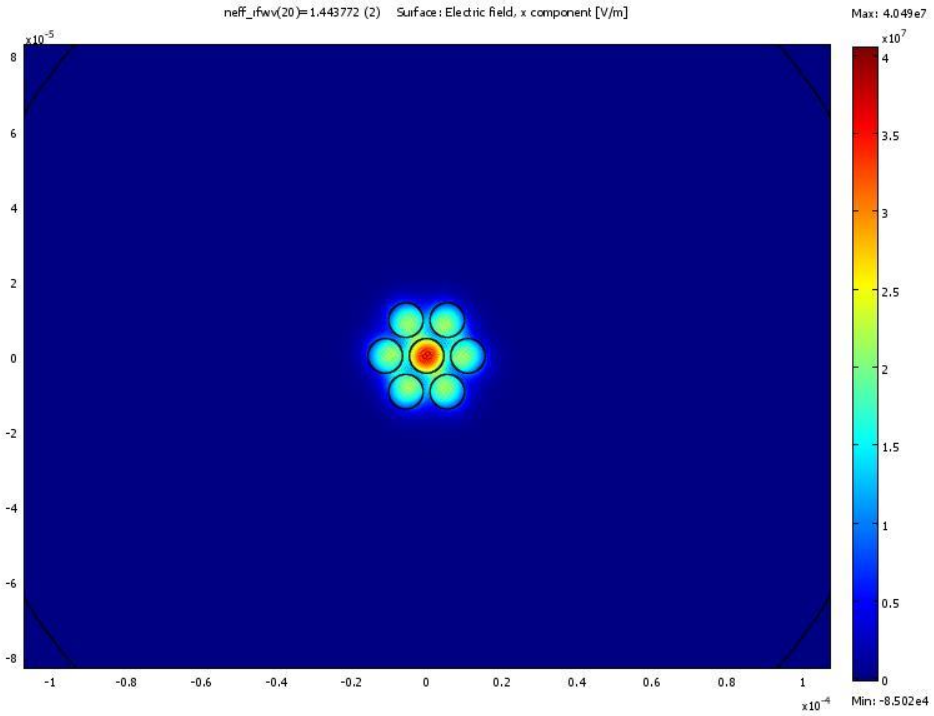

Fig. 3.3. Electric field distribution of the fundamental super-mode with a modal refractive index of 1.443772, found by a finite difference method mode solver

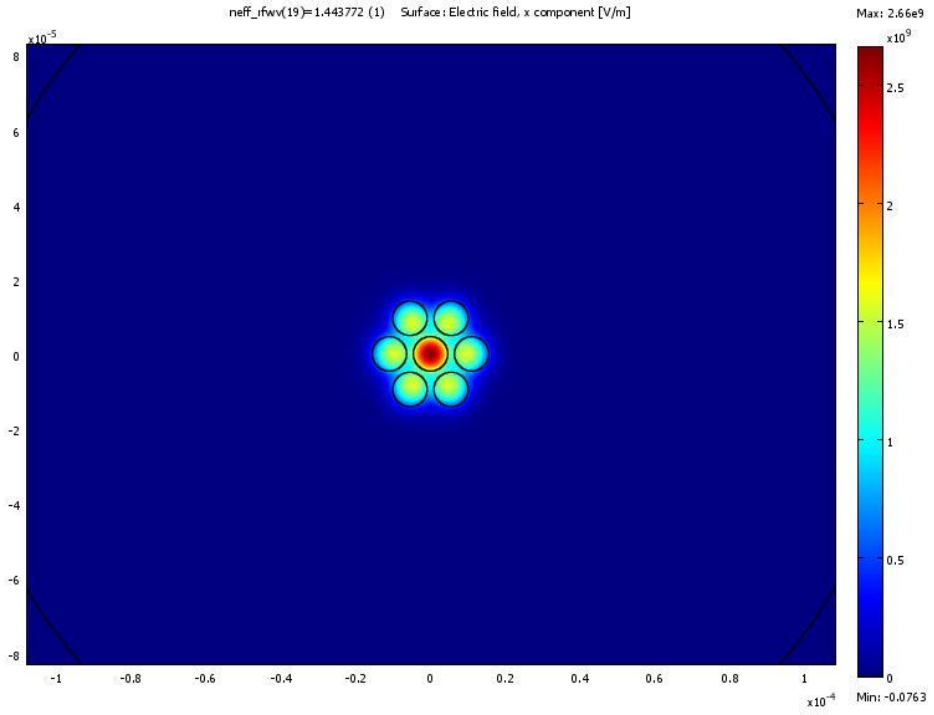

Fig. 3.4. Electric field distribution of the second super-mode with a modal refractive index of 1.443772, found by a finite difference method mode solver.

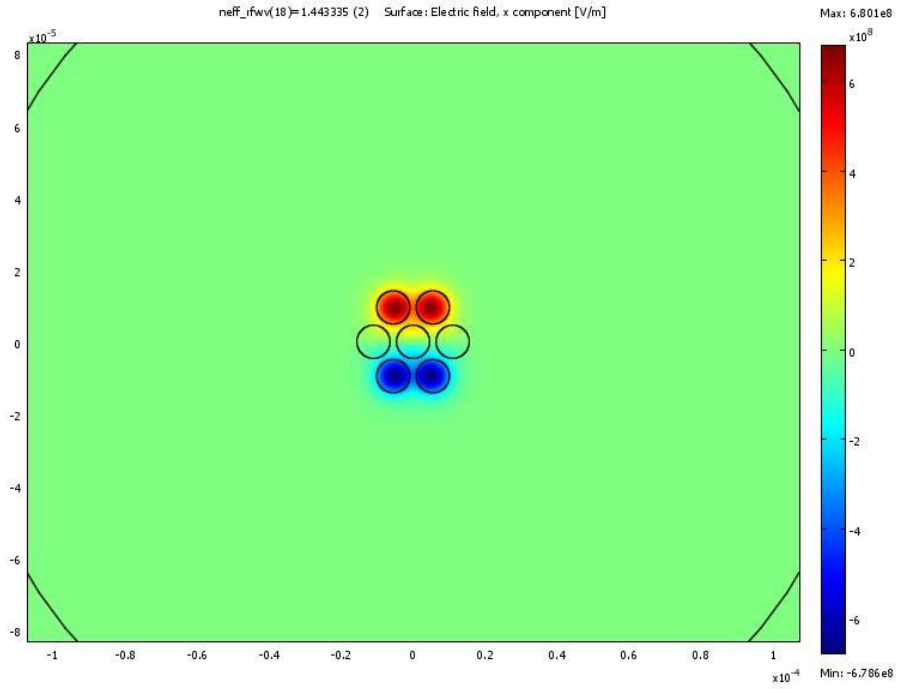

Fig. 3.5. Electric field distribution of the third super-mode with a modal refractive index of 1.443335 found by a finite difference method mode solver.

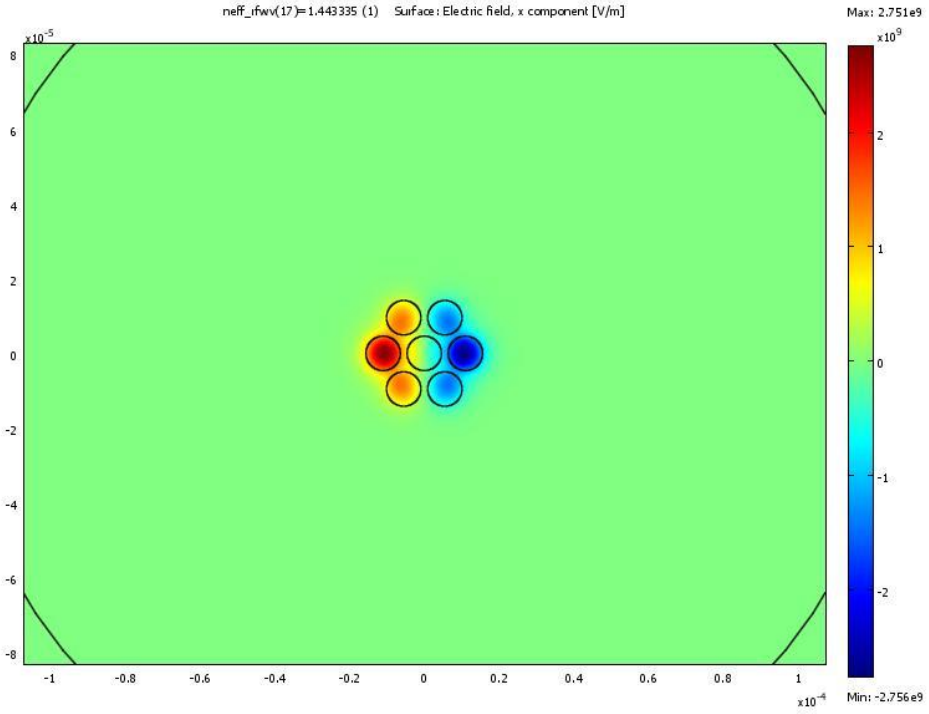

Fig. 3.6. Electric field distribution of the fourth super-mode with a modal refractive index of 1.443335 found by a finite difference method mode solver.

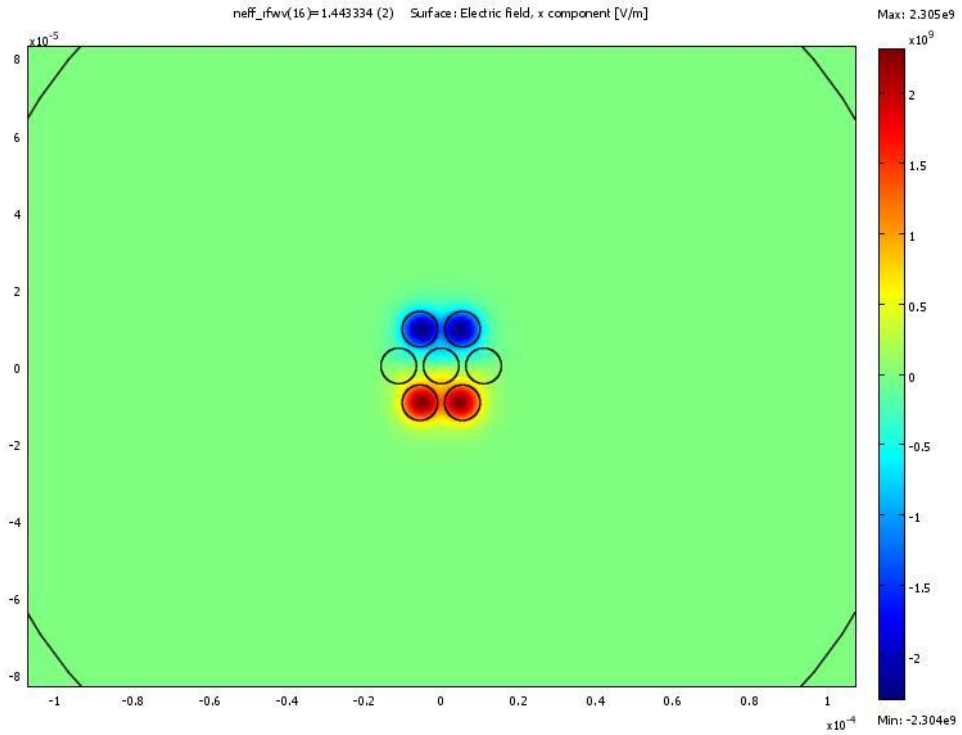

Fig. 3.7. Electric field distribution of the fifth super-mode with a modal refractive index of 1.443334 found by a finite difference method mode solver.

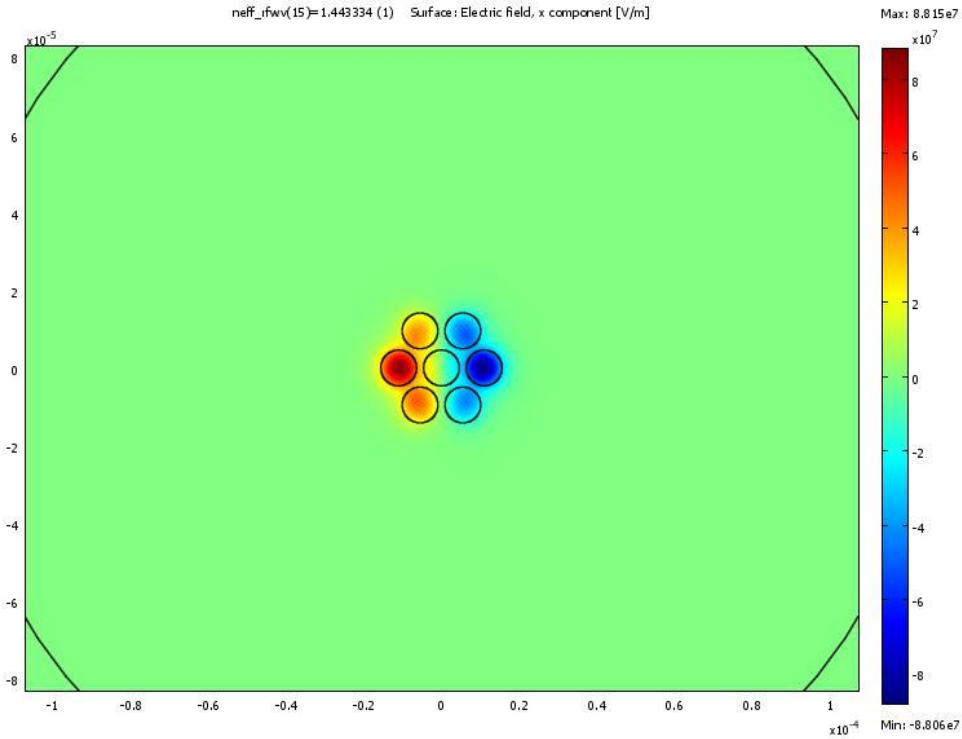

Fig. 3.8. Electric field distribution of the sixth super-mode with a modal refractive index of 1.443334 found by a finite difference method mode solver.

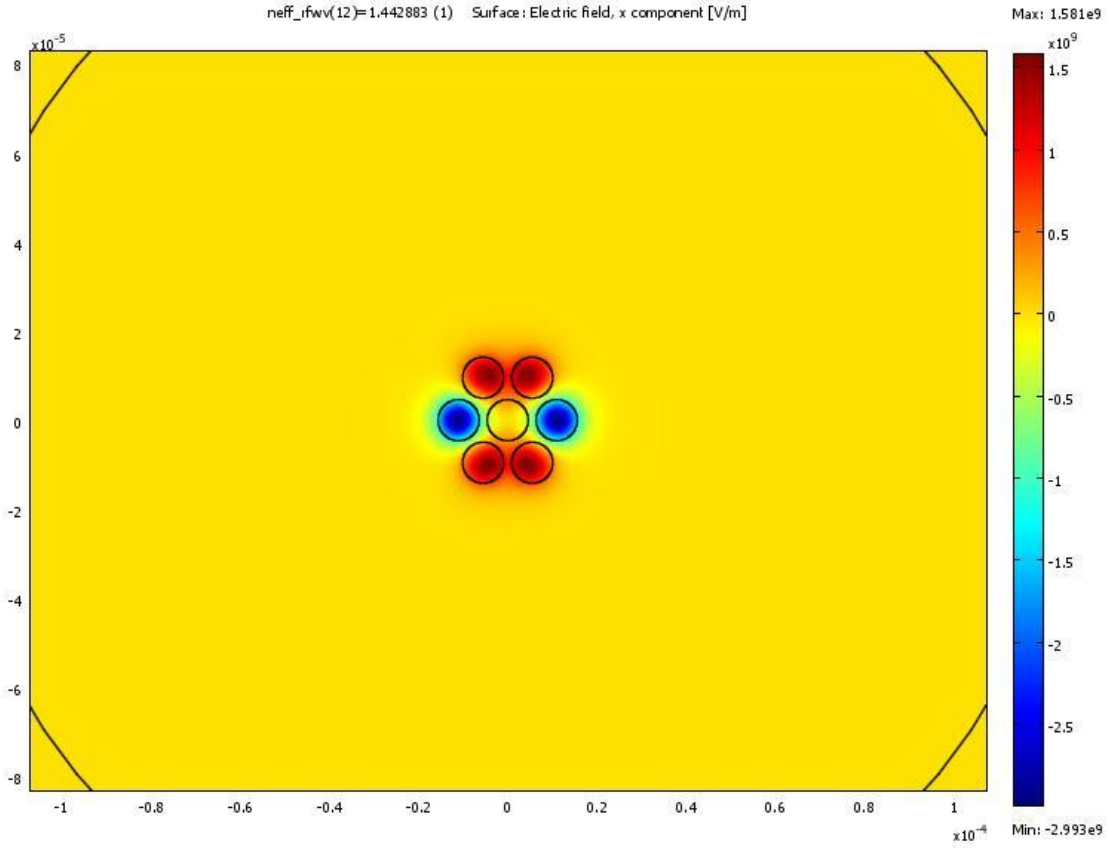

Fig. 3.9. Electric field distribution of the seventh super-mode with a modal refractive index of 1.442883 found by a finite difference method mode solver.

From Fig. 3.3 to 3.9 the electric field distributions of every super-mode supported by the 7 core fiber are shown. As it was observed from the simulation, the seven core fiber supports 7 super-modes. However, when the excitation of light through this MCF is made by a SMF only two super-modes are propagated into the seven-core fiber [18] (Fundamental and second super-modes from Fig. 3.3 and 3.4, due to the central core excitation, since the SMF core matches with the central core of the MCF). These two super-modes travel through the seven core fiber accumulating a phase shift between them. As they arrive to the second SMF, they are recoupled into the SMF core, and as a result a periodic interference pattern, because of the difference modal refractive index of each super-mode, is generated due to the interference between super-modes.

When the fiber is bent, the refractive index structure profile of the MCF becomes asymmetric and there is a refractive index change due to the elasto-optic coefficient, so depending of the bending radius there is a generation of a differential phase delay between the two super-modes. Thus, this allows the correlation of the bending radius with the changes in the transmission spectrum. In this particular case, a change in the wavelength shift and fringes visibility is observed.

3.4 Experimental results

The set up used to characterize the bending response of the sensor is shown in Fig. 3.10

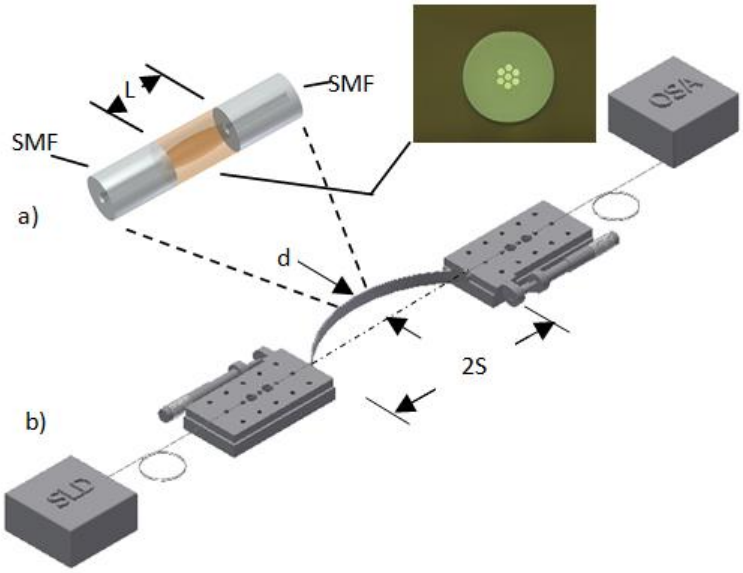

Fig. 3.10. Set up using to characterize the bending response of the MCF sensor

A simple transmission set up was used, as a source, a superluminiscent diode Thorlabs SLD1550S-A1 (~250 nm bandwidth) was used, and as a detector, an optical spectrum analyzer was utilized. The sensors were placed in a v-groove made in a thin metal sheet of 316 mm in length, as it can be observed from Fig.3.2, this thin metal sheet was positioned between the translation stages, keeping static one translation stage and moving the other in direction towards the metal sheet the curvature radius is varied. For the calculation of the bending radius, the parameters S and d where used, applying the relation $1/R=2d/(d^2+S^2)$ [20].

For three different curvature radii, the transmission spectra of two sensor devices with L = 18 and 10 mm of seven core fiber lengths are shown in Fig. 3.11

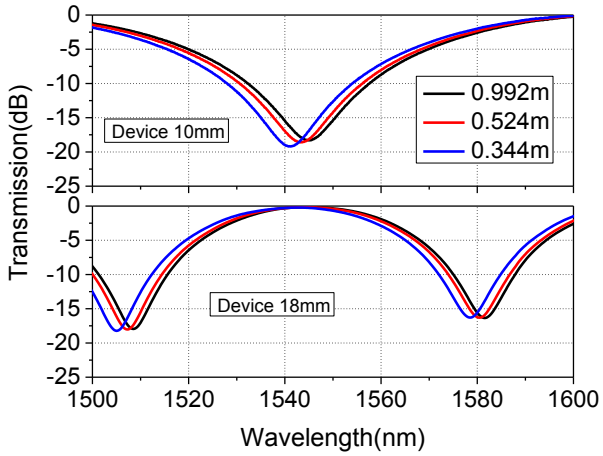

Fig. 3.11. Sensor device spectra of two seven core fiber sensors with L = 10 and 18 mm of seven core fiber length at three different curvature radius (0.992, 0.524, 0.344 mm).

From Fig. 3.11, it can be noticed that the peak wavelength and the amplitude modulation depth is altered by the bending radius of the device, while the fringe period remains almost constant. It is also noticed that there is a dependence of the fringe period with the length of seven core fiber. Fig. 3.12 shows this dependence, which has a linear behavior with a factor of 1294 nm/mm^{-1}

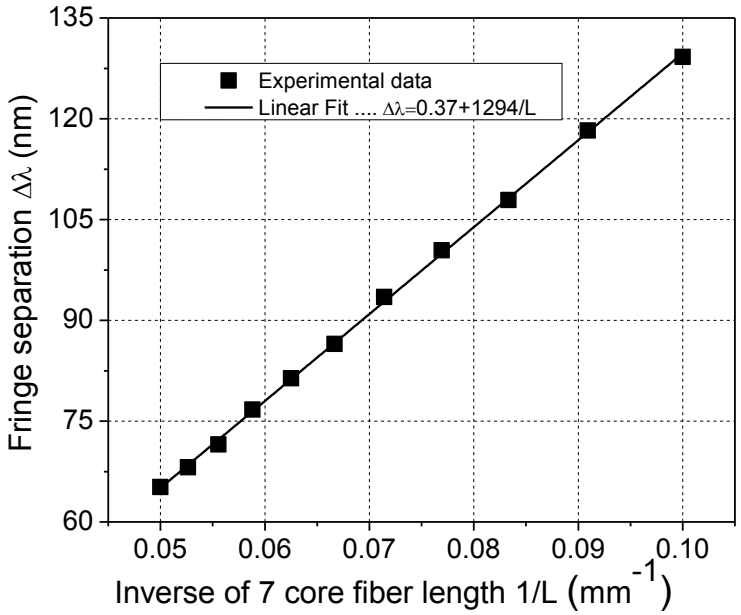

Fig. 3.12. Relationship between inverse length of seven core fiber and interference fringe separation of the fabricated devices.

From Fig. 3.11, we found that both the visibility and wavelength shift in the interference pattern were strongly dependent on the bending radius of the MCF devices. Both of these parameters can be used to find the bending radius of the MCF sensor.

The quality of the fringe pattern is quantified by the fringe visibility [2]. As the MCF is bent, the change in fringe visibility is due to the fact that the field is being radiated out of the MCF structure [21].

For calculating the visibility, the relationship $V = \frac{I_{\min}^{up} - I_{\min}^{low}}{I_{\min}^{up} + I_{\min}^{low}}$ [22] was used

The fringe visibility versus inverse curvature radius for three MCF devices with seven core fiber lengths of 10, 16, and 25 mm is shown in Fig. 3.13. A linear fit was applied and we found slopes of 3.47 a.u./ mm^{-1}, 2.39 a.u./mm^{-1}, and 3.86 a.u./mm^{-1}, for these three lengths of MCF, respectively.

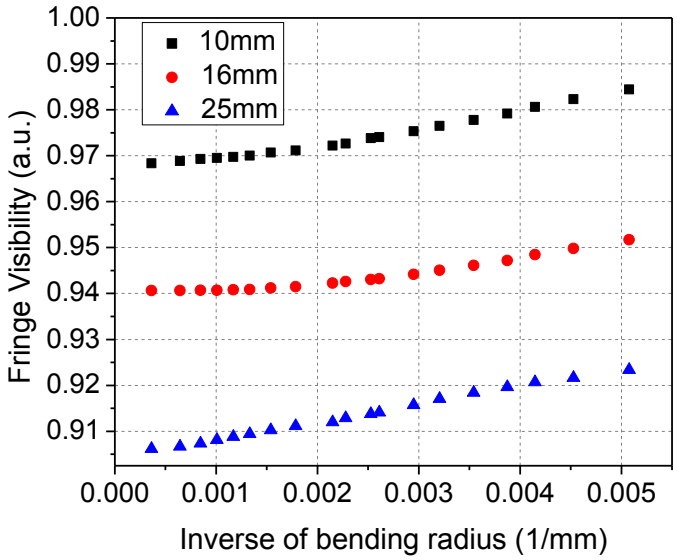

Fig. 3.13. Fringe visibility versus inverse curvature radius for three different seven-core fiber lengths: 10 mm (squares), 16 mm (circles), and 25 mm (triangles).

From Fig. 3.13 it is noticed that when the devices are straight, the transmission spectra have initial visibility values that can be considered as the zero bending condition. As the sensor device is bent, the visibility grows approximately linearly. And considering that the limiting and maximum value of the visibility is unity, it can be inferred that the dynamic range of longer length MCF is appropriated to measure larger inverse radii, while the dynamic range of shorter length MCF is appropriated to measure smaller inverse radii.

Another way to measure the bending radius using this MCF is by the wavelength shift of the transmission spectral. Fig 3.14 shows the dependence of the transmission wavelength notch on the inverse curvature radius of a sensor with 10 mm MCF length.

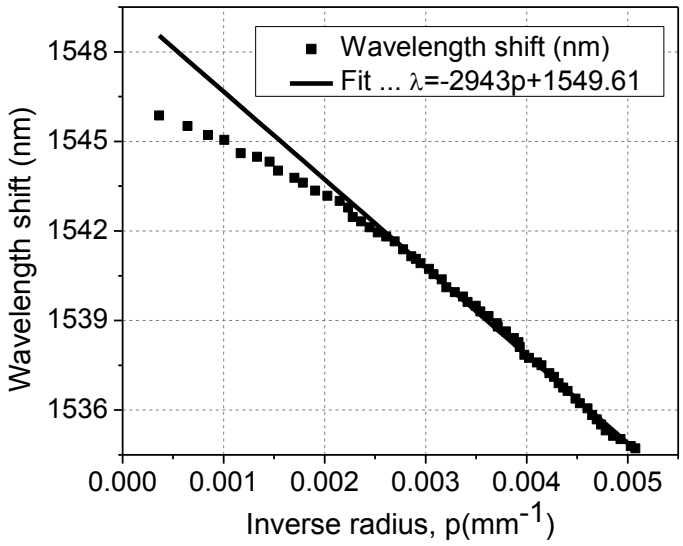

Fig. 3.14. Transmission notch wavelength versus inverse bending radius of the sensor device length with 10 mm of seven-core fiber. The solid line shows a linear fit of the most sensitive range of 0.0022–0.005 mm^{-1} (200 to 450 mm in terms of bending radius).

In the range from 0.0022 mm^{-1} (450mm) to 0.005 mm^{-1} (200mm) is found the most sensitive region for the sensor with a value of -2943 nm/mm^{-1}. The sensitivity drops to -1653.7 nm/mm^{-1} for ranges below to 0.0022 mm^{-1}. Several sensor devices with different seven core fiber lengths were tested and a very similar behavior of that in Fig. 3.7 was obtained.

When the device was bent in opposite directions, slight differences were observed in the transmission spectrum in visibility as well as in wavelength shift. Fig. 3.15 illustrates these spectral differences for a device with 5 mm of seven core fiber length bent at three bending radius (0.00178, 0.00269, and 0.00337 mm^{-1}) in opposite directions. Solid curves are the transmitted spectra for one direction and the dashed curves are the transmitted spectra for the opposite direction. This effect can be exploited to identify the bending direction that experiences the MCF sensor. These differences may be due to small variations in the symmetry of the seven-core fiber when it is bent, since it is difficult to guarantee that the outer core fiber orientation is exactly the same when the bending is in opposite or different direction.

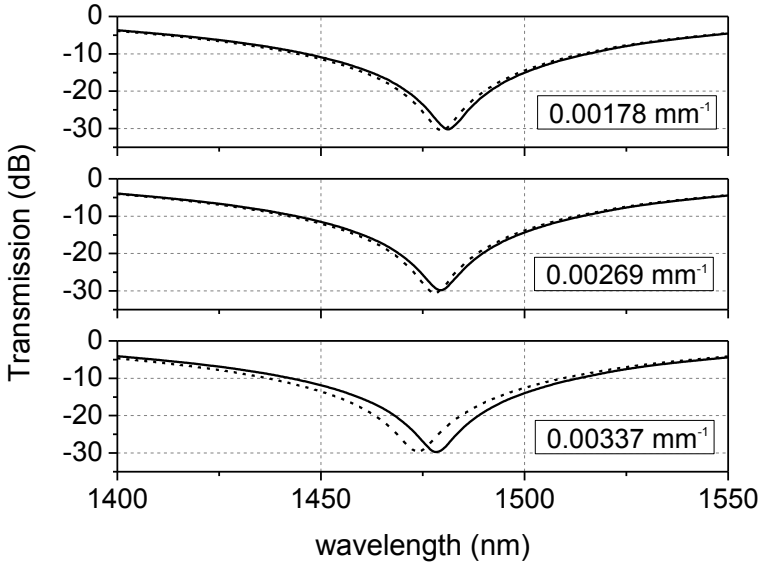

Fig. 3.15. Spectral response of a device with 5 mm of MCF length that has been bent in two opposite directions. The continuous curve is one direction, and the dash curve represents the opposite direction for three different inverse curvature radii (0.00178 mm^{-1}, 0.00269 mm^{-1}, and 0.00337 mm^{-1}).

In this case, with this MCF structure sensor, the super-modes are well confined in the optical waveguide, so that this sensor is no sensible to surrounding refractive indices, allowing the embedding in a solid protection matrix if it is needed. This well confined field is a good advantage over sensors based on the interaction of the evanescent part of the optical fiber modes.

In order to evaluate the thermal response of the device, the MCF (without bending) was tested in the range from room temperature to 100^{o}C, and a wavelength peak shift of about 4 nm was observed, and a very slight variation of the visibility. This effect can be ignored if the temperature stays constant during the bending measurement or it can be isolated by the use of a bending insensitive temperature sensor.

3.5 References

[1] M. Deng, C. P. Tang, T. Zhu, and Y. J. Rao, “Highly sensitive bend sensor based on Mach–Zehnder interferometer using photonic crystal fiber,” Opt. Commun., vol. 284, no. 12, pp. 2849–2853, Jun. 2011.
[2] D. Monzon-Hernandez, A. Martinez-Rios, I. Torres Gomez, and G. Salceda-Delgado, "Compact optical fiber curvature sensor based on concatenating two tapers", Optics Letters, Vol. 36, No. 22, November 15, 2011.
[3] Q. Q. Meng, X. Y. Dong, Y. Zhou, K. Ni, Z. M. Chen, C. L. Zhao and S. Z. Jin, "Simultaneous measurement of curvature and temperature with fiber taper-based MZI Containing fiber Bragg grating", Journal of Electromagnetic Waves and Applications, Vol. 26, Nos. 17-18, December 2012, 2438-2444.
[4] Ruohui Wang, Jing Zhang, Yinyan Weng, Qiangzhou Rong, Yue Ma Zhongyao Feng, Manli Hu, and Xueguang Qiao, "Highly Sensitive Curvature Sensor Using an In-Fiber Mach-Zehnder Interferometer", IEEE Sensors Journal, Vol. 13, No. 5, May 2013.
[5] Zhaobing Tian, Scott S-H. Yam, and Hans-peter Loock, “Single-Mode Fiber Refractive Index Sensor Based on Core-Offset Attenuators”, IEEE Photonics Technology Letters, Vol. 20, No. 16, August 15, 2008.
[6] O. Frazão, J. Viegas, P. Caldas, J. L. Santos, F. M. Araújo, L. A. Ferreira, and F. Farahi, “All-fiber Mach–Zehnder curvature sensor based on multimode interference combined with a long-period grating”, Opt. Lett., vol. 32, no. 21, pp. 3074–3076, Nov. 2007.
[7] Wei Chang Wong, Chi Chiu Chan, Huaping Gong, and Kam Chew Leong,"Mach-Zehnder Photonic Crystal Interferometer in Cavity Ring-Down Loop for Curvature Measurement", IEEE Photonics Technology Letters, Vol. 23, No.12, June 15, 2011.
[8] R.M. Silvia, M.S. Ferreira, J. Kobelke, K. Schuster, and O. Frazão, "Simultaneous measurement of curvature and strain using a suspended multicore fiber", Optics Letters, Vol. 36, No.19, October 1, 2011.
[9] H.P. Gong, C.C. Chan, P.Zu, L.H. Chen, X.Y. Dong, "Curvature measurement by using low-birefrigence photonic crystal fiber based sagnac loop",Optics Communications 283 (2010), 3142-3144.
[10] Rajan Jha, Joel Villatoro, Gonçal Badenes, and Valerio Pruneri, "Refractometry based on a photonic crystal fiber interferometer", Optics Letters, Vol. 34, No. 5, March 1. [11] D. Dorosz and M. Kochanowicz, Opto-Electron. Rev. 19, 40 (2011).
[11] Y. Liu, L. Zhang, J. A. R. Williams, and I. Bennion, “Optical Bend Sensor Based on Measurement of Resonance Mode Splitting of Long-Period Fiber Grating”, Bennion, IEEE Photonics Technology Letters, Vol. 12, No. 5, May 2000.
[12] Susana Silva, O Frazão, J Viegas, L A Ferreira1, F M Araújo, F Xavier Malcata and J L Santos, "Temperature and strain-independent curvature sensr based on a singlemode / multimode fiber optic structure", Measurement science and technology, 22, 085201 (2011).

[13] J. R. Guzman-Sepulveda, R. Dominguez-Cruz, J. J. Sánchez- Mondragón, and D. A. May-Arrioja, “Curvature sensor based on a two-core optical fiber,” in Quantum Electronics and Laser Science Conference (CLEO), OSA Technical Digest (Optical Society of America, 2012), paper JW2A.116.
[14] G. Chunying and Y. Libo, “Supermodes Analysis for linearly distributed multicore fiber,” in The International Symposium on Photonics and Optoelectronics (SOPO), Wuhan, China, August 14–16, 2009, pp. 1–4.
[15] Jinping Chen, Jun Zhou, and Zhenhong Jia, "High-Sensitivity Displacement Sensor Based on a Bent Fiber Mach-Zehnder Interferometer",IEEE Photonics Technology Letters, vol.25, No. 23, December 1, 2013.
[16]. Y. Liu, L. Zhang, J. A. R. Williams, and I. Bennion, “Optical Bend Sensor Based on Measurement of Resonance Mode Splitting of Long-Period Fiber Grating”, Bennion, IEEE Photonics Technology Letters, Vol. 12, No. 5, May 2000.
[17] Luo Niu, Chun-Liu Zhao, Huaping Gong, Yi Li, Shangzhong Jin, “Curvature sensor based on two cascading abrupt-tapers modal interferometer in single mode fiber”, Optics Communications 333 (2014) 11-15
[18] A. Van Newkirk, E. Antonio-Lopez, G. Salceda-Delgado, R. Amezcua-Correa, and A. Schülzgen, "Optimization of multicore fiber for high-temperature sensing", Opt. Lett. 39, 4812 (2014).
[19] J. E. Antonio-Lopez, Z. Sanjabi Eznaveh, P. LikamWa, A. Schülzgen, and R. Amezcua-Correa, “Multicore fiber sensor for high-temperature applications up to 1000 ^{o}C”, Opt. Lett. 39, 4309 (2014).
[20] Weichong Du, H Y Tam, Michael S Y Liu, and X M Tao, "Long-period fiber grating bending sensors in laminated composite structures", Proc. SPIE 3330, 284 (1998).
[21] D. Marcuse, “Curvature loss formula for optical fibers”, J. Opt. Soc. Am. 66, 216 (1976).
[22] E. H. Hecht, Optics (Addison-Wesley, 1987).

Chapter 4

Conclusions

Resume

In this chapter the conclusions of the project will be presented

4.1 Conclusions

In this work, three optical fiber devices based on modal interference were demonstrated, namely, a comb-filter based on two concatenated tapered optical fibers, the application of the comb-filter as bending sensor, and a bending sensor using super-mode interference in a seven core fiber.

The comb-filter, described in chapter two and based in two in-series tapers that form a MZFI, was subject to an optimization process. The optimization process allowed the analysis and study of the tapers geometry on the transmission spectrum, i.e., the effects of transition length, waist length and diameter, separation between tapers. We found that the diameter waist has the greater effect to position the interference pattern, the transition length has the greater effect in the size of the interference band, the waist length affects the fringe visibility (changing the optical path of the two interfering signals), and the period is determined by the separation between tapers. This optimization study allows the selection of the operation wavelength determined by the available source and to select the fringe separation and visibility that are very important in applications such as optical fiber sensors. In particular, the optimized tapers have been used for measuring bending and as tunable elements in fiber lasers.

The application of the comb filter as a bending sensor was described in chapter two. This device had the characteristic that being straight no interference pattern was observed in the transmission spectrum. However, as the device was bent, the interference pattern gradually started to appear, and its strength (visibility) was dependent of the bending radius. The interrogation of this bending sensor was made by the fringe visibility of the interference pattern in the transmission spectrum. It was found that it is possible to set the dynamic range of the sensor by changing the separation between tapers and the waist diameter. One of the main advantages of this sensor was the fact that the zero bending state was clearly identified, as in this case no interference fringes were observed.

The bending sensor using super-mode interference was described in chapter three. This work was realized during my pre-doctoral period at CREOL (Central Florida University), under the guidance of Dr. Rodrigo Amezcua. This sensor had a similar behavior as the comb-filter bending sensor, but in addition to the visibility change, a wavelength shift was observed and can be used as an alternative interrogation method. The wavelength shift sensitivity is a very important characteristic that make this kind of sensor structure very promising in many applications. It is worth to mention that the target application of this device was on the measurement of pressure and temperature for the oil industry, and this work was made in conjunction with the company Faz Technology (Orlando Florida).

As a future work, an improvement of modal interference in optical fibers can be done in order to sense more diverse parameters, such as torsion, strain, compression, refractive index, humidity, cleaning, pressure, position, displacement, velocity, flow, vibration, temperature, and so on. Furthermore, the presence of the evanescent field in tapered optical fiber is another application

field to play with for the construction of novel devices, for example, optical tweezers and sensing environmental parameters. In the case of the super-mode interference, an improvement also can be done by means of the construction of novel devices using the multicore fiber structure with the aim of generate controlled super-mode interference for sensing applications.

Another field to explore with these modal devices will be playing with the polarization in order to find different responses and improvements. Furthermore, modal selection methods in multicore-fibers are also a field that will give rise to interesting and useful studies and applications. Currently, I am exploring some possibilities and making initial experimental work on this topic.

Appendix

Modal solutions for optical fibers

A.1 Fundamental equations

In this section the fundamental concepts for the propagation light in optical fiber will be reviewed. The first step is to derivete the scalar and vector wave equations, which are specialised forms of the Maxwell equations and are applicable to waveguide with arbitrary refraction index profile.

Optical fibers are dielectric material and each layer, thus every fiber layer will be caracterised only by the dielectric constant, which in the SI it is related to the refracion index by

$$\epsilon = \epsilon_0 * n^2 \tag{0.1}$$

Where ϵ_0 is the permittivity in the free space.

Besides, as the material is not magnetic we have

$$\mu = \mu_0 \tag{0.2}$$

for this work only step index refraction profile will be taken in consideration, which means that the refraction index profile is constant in every waveguide layer, just as it is plotted in Fig. A1

```
In[1]:= Graphics[{Circle[{0, 0}, 4.2]}, Axes → True, PlotRange → {{-7, 7}, {-7, 7}},
          AxesLabel → {"r (μm)", "r (μm)"}, PlotLabel → "Step profile"]
        Plot[Piecewise[{{1.4458, 0 < x ≤ 4.2}, {1.4319, x > 4.2}}], {x, 0, 10},
          PlotRange → {{0, 10}, {1.4, 1.45}}, PlotStyle → Thick,
          AxesLabel → {"r (μm)", "Refractive index, n(r)"}]
```

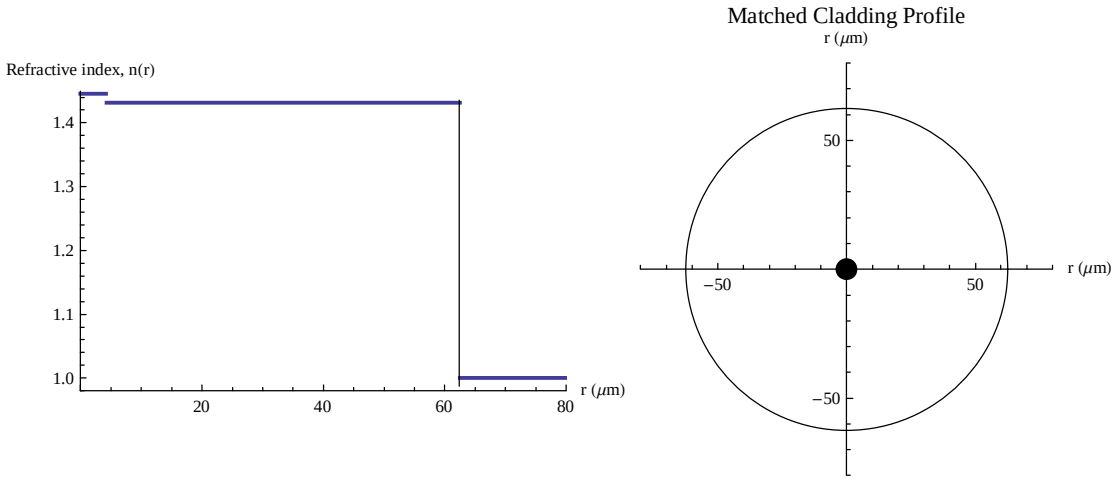

Figure A.1 Refraction index profile for a Matched Cladding fiber.

Refraction index profiles as the ones shown in figures 2.1 to 2.4 are approximated representations of real fiber optics,since the real profiles differ on the refraction index transitions between borders of layers, due to the fact that real optical fiber refraction index profile has not a steepening transitions but a slight and gradual transitions between layers. However most of the observed phenomena in real optical fiber can be predicted using this step index assumption.

Using the step index approximation allows use of the scalar wave equation where the polarizing effects are not taken into consideration, so that solving the homogeneous scalar wave equation for each layer and then matching the solution applying the adequate boundary conditions, we obtain the general propagation light on the optical fiber.

A.2 Solutions to the scalar wave equation for multilayer circular waveguides

In solving the wave equation for the case of a circularly symmetric waveguide, in the scalar approximation, it is customary first to solve the wave equations for the longitudinal components of transverse electric and magnetic fields. In this case, the wave equations for the $e_z(r,\phi)$ and $h_z(r,\phi)$ are simply given by:

$$\left[\nabla_t^2 + k^2\left(n^2 - {n_{\text{eff}}}^2\right)\right] e_z(\boldsymbol{r}_t) = 0 \tag{0.3}$$

$$\left[\nabla_t^2 + k^2\left(n^2 - {n_{\text{eff}}}^2\right)\right] h_z(\boldsymbol{r}_t) = 0 \tag{0.4}$$

where ∇_t is the transverse Laplacian, r_t indicates funcionality on the transverse coordinates with respect to the propagation direction, n is the refractive index, k is the free space propagation constant, and n_{eff} is the effective refractive index of the particular solution of mode of the waveguide. In cylindrical coordinates, the other components may be found from the following relations [1] :

$$e_r(r,\phi) = \frac{1}{k^2(n^2 - {n_{\text{eff}}}^2)}\left\{k\, n_{\text{eff}}\, \frac{\partial\,(i\, e_z(r,\phi)}{\partial\, r} + \frac{k\,\eta_0}{r}\, \frac{\partial\,(i\, h_z(r,\phi)}{\partial\,\phi}\right\} \tag{0.5}$$

$$e_\phi(r,\phi) = \frac{1}{k^2(n^2 - {n_{\text{eff}}}^2)}\left\{\frac{k\, n_{\text{eff}}}{r}\, \frac{\partial\,(i\, e_z(r,\phi)}{\partial\,\phi} - k\,\eta_0\, \frac{\partial\,(i\, h_z(r,\phi)}{\partial\, r}\right\} \tag{0.6}$$

$$h_r(r,\phi) = \frac{1}{k^2(n^2 - {n_{\text{eff}}}^2)}\left\{k\, n_{\text{eff}}\,\eta_0\, \frac{\partial\,(i\, h_z(r,\phi)}{\partial\, r} - \frac{k\, n^2}{r}\, \frac{\partial\,(i\, e_z(r,\phi)}{\partial\,\phi}\right\} \tag{0.7}$$

$$h_\phi(r,\phi) = \frac{1}{k^2(n^2 - {n_{\text{eff}}}^2)}\left\{\frac{k\, n_{\text{eff}}\,\eta_0}{r}\, \frac{\partial\,(i\, h_z(r,\phi)}{\partial\,\phi} + k\, n^2\, \frac{\partial\,(i\, e_z(r,\phi)}{\partial\, r}\right\} \tag{0.8}$$

where η_0 is the free space permitivity.

Eqs. (0.3) and (0.4) have the same form, so that, it is enough to consider an arbitrary function $\Psi(r,\phi)$ which may represent either e_z or h_z. It is assumed that $\Psi(r,\phi)$ is separable in the following form

$$\Psi(r,\phi) = R(r)\, f(\phi) \tag{0.9}$$

Then, the general solution for Ψ(r,ϕ) may fall into two different cases, depending on the relative values of the refractive index in the medium and the effective refractive index corresponding to a particular solution or mode:

$$\Psi(r,\ \phi) = f(\phi) \begin{cases} A_i\, J_m(u_i\, r) + B_i\, Y_m(u_i\, r) & \text{if } n_i > n_{\text{eff}} \ \text{ where } u_i^2 = k^2\left(n_i^2 - n_{\text{eff}}^2\right) \\ C_i\, I_m(w_i\, r) + D_i\, K_m(w_i\, r) & \text{if } n_i < n_{\text{eff}} \ \text{ where } w_i^2 = k^2\left(n_{\text{eff}}^2 - n_i^2\right) \end{cases} \tag{0.10}$$

Here the subscript i refers to the particular layer of the waveguide with material refractive index n_i.

A.2.1 Solutions for a matched cladding profile

The case of interest in this thesis is the matched cladding profile (shown in Fig. (A.1)). For this refraction index profile there will be two distinc possible solutions which corresponds to modes supported by the waveguide structure formed by the core and the cladding (core modes), and the waveguide structure formed by the cladding and the external medium (cladding modes). In this section the solution (A.10) will be particularized to each type of solution, assuming always even modes with:

$$f(\phi) = \begin{cases} \cos(m\,\phi) & \text{for } e_z(r,\ \phi) \\ -\sin(\mathrm{m}\phi) & \text{for } h_z(r,\ \phi) \end{cases} \tag{0.11}$$

A.2.1.1 Core modes

The devices developed in this work are based on tapers whose transverse dimensions are such that the core modes remains guided by the core-cladding structure, i.e., there is no transition from core to cladding guiding in the taper. In this case, it may be assumed an infinite cladding such that the effective refractive index of the core modes has values in the range given by the following condition:

$$n_2 < n_{\text{eff}} < n_1 \tag{0.12}$$

Thus, from (A.10), the solutions for e_z and h_z are given by:

$$e_z(r,\ \phi) = \cos(l\,\phi) \begin{cases} A_1^e\, J_m(u_1\, r) & 0 \le r \le r_1 \\ C_2^e\, K_m(w_2\, r) & r_1 < r \le r_2 \end{cases} \tag{0.13}$$

$$h_z(r,\ \phi) = -\sin(l\,\phi) \begin{cases} A_1^h\, J_m(u_1\, r) & 0 \le r \le r_1 \\ C_2^h\, K_m(w_2\, r) & r_1 < r \le r_2 \end{cases} \tag{0.14}$$

Where A_1^e, C_2^e, A_1^h, C_2^h are constants and J_m, K_m are Bessel functions.

Here, in the second layer it is assumed that the field must be decaying, so that the term involving the Bessel function I_l has been neglected.

Clear all variable definitions

```
Clear["Global`*"]
```

Definition of the electric field in both layers

In[2]:=
```
Ez1[r_, ϕ_] = Cos[m ϕ] * A1e * BesselJ[m, u1 * r];
Ez2[r_, ϕ_] = Cos[m ϕ] * (C2e * BesselK[m, w2 * r]);
```

Definition of the magnetic field in both layers

In[4]:=
```
Hz1[r_, ϕ_] = -Sin[m ϕ] * A1h * BesselJ[m, u1 * r];
Hz2[r_, ϕ_] = -Sin[m ϕ] * (C2h * BesselK[m, w2 * r]);
```

Calculation of the radial compound for the electric field in both layers

In[6]:=
```
Er1[r_, ϕ_] = 1/u1^2 * (k * nef * D[I * Ez1[r, ϕ], r] + k * η0/r * D[I * Hz1[r, ϕ], ϕ]) // Simplify;
Er2[r_, ϕ_] = 1/-w2^2 * (k * nef * D[I * Ez2[r, ϕ], r] + k * η0/r * D[I * Hz2[r, ϕ], ϕ]) // Simplify;

Print["0≤r≤r1:"]
Print["E_r(r,ϕ)= ", Er1[r, ϕ] // TraditionalForm]
Print[""]
Print["r1<r≤r2:"]
Print["E_r(r,ϕ)= ", Er2[r, ϕ] // TraditionalForm]
```

0≤r≤r1:

$$E_r(r,\phi) = \frac{i\, k \cos(m\,\phi)\,(A1e\ nef\ r\ u1\ J_{m-1}(r\ u1) - A1e\ nef\ r\ u1\ J_{m+1}(r\ u1) - 2\ A1h\ \eta 0\ m\ J_m(r\ u1))}{2\ r\ u1^2}$$

r1<r≤r2:

$$E_r(r,\phi) = \frac{i\, k \cos(m\,\phi)\,(C2e\ nef\ r\ w2\ K_{m-1}(r\ w2) + C2e\ nef\ r\ w2\ K_{m+1}(r\ w2) + 2\ C2h\ \eta 0\ m\ K_m(r\ w2))}{2\ r\ w2^2}$$

Calculation of the radial compound for the magnetic field in both layers

In[13]:=
```
Hr1[r_, ϕ_] = 1/u1^2 * (k * nef * η0 * D[I * Hz1[r, ϕ], r] - k * n1^2/r * D[I * Ez1[r, ϕ], ϕ]) // Simplify;
Hr2[r_, ϕ_] = 1/-w2^2 * (k * nef * η0 * D[I * Hz2[r, ϕ], r] - k * n2^2/r * D[I * Ez2[r, ϕ], ϕ]) // Simplify;
Print["0≤r≤r1:"]
Print["H_r(r,ϕ)= ", Hr1[r, ϕ] // TraditionalForm]
Print[""]
Print["r1<r≤r2:"]
Print["H_r(r,ϕ)= ", Hr2[r, ϕ] // TraditionalForm]
```

0≤r≤r1:

$$H_r(r,\phi) = -\frac{i\, k \sin(m\,\phi)\,\left(-2\ A1e\ m\ n1^2\ J_m(r\ u1) + A1h\ \eta 0\ nef\ r\ u1\ J_{m-1}(r\ u1) - A1h\ \eta 0\ nef\ r\ u1\ J_{m+1}(r\ u1)\right)}{2\ r\ u1^2}$$

r1<r≤r2:

$$H_r(r,\phi) = -\frac{i\, k \sin(m\,\phi)\,\left(2\ C2e\ m\ n2^2\ K_m(r\ w2) + C2h\ \eta 0\ nef\ r\ w2\ K_{m-1}(r\ w2) + C2h\ \eta 0\ nef\ r\ w2\ K_{m+1}(r\ w2)\right)}{2\ r\ w2^2}$$

Calculation of the azimuthal compound for the electric field in both layers

In[20]:=
```
Eϕ1[r_, ϕ_] = 1/u1^2 * ((k * nef)/r * D[I * Ez1[r, ϕ], ϕ] - k * η0 * D[I * Hz1[r, ϕ], r]) // Simplify;
Eϕ2[r_, ϕ_] = 1/(-w2^2) * ((k * nef)/r * D[I * Ez2[r, ϕ], ϕ] - k * η0 * D[I * Hz2[r, ϕ], r]) // Simplify;
Print["0≤r≤r1:"]
Print["E_ϕ(r,ϕ)= ", Eϕ1[r, ϕ] // TraditionalForm]
Print[""]
Print["r1<r≤r2:"]
Print["E_ϕ(r,ϕ)= ", Eϕ2[r, ϕ] // TraditionalForm]
```

$0 \le r \le r1:$

$$E_\phi(r,\phi) = \frac{i\, k \sin(m\,\phi)\,\left(-2\,A1e\,m\,nef\,J_m(r\,u1) + A1h\,\eta 0\,r\,u1\,J_{m-1}(r\,u1) - A1h\,\eta 0\,r\,u1\,J_{m+1}(r\,u1)\right)}{2\,r\,u1^2}$$

$r1 < r \le r2:$

$$E_\phi(r,\phi) = \frac{i\, k \sin(m\,\phi)\,\left(2\,C2e\,m\,nef\,K_m(r\,w2) + C2h\,\eta 0\,r\,w2\,K_{m-1}(r\,w2) + C2h\,\eta 0\,r\,w2\,K_{m+1}(r\,w2)\right)}{2\,r\,w2^2}$$

Calculation of the azimuthal compound for the magnetic field in both layers

In[27]:=
```
Hϕ1[r_, ϕ_] = 1/u1^2 * ((k * nef * η0)/r * D[I * Hz1[r, ϕ], ϕ] + k * n1^2 * D[I * Ez1[r, ϕ], r]) // Simplify;
Hϕ2[r_, ϕ_] = 1/(-w2^2) * ((k * nef * η0)/r * D[I * Hz2[r, ϕ], ϕ] - k * n2^2 * D[I * Ez2[r, ϕ], r]) // Simplify;
Print["0≤r≤r1:"]
Print["H_ϕ(r,ϕ)= ", Hϕ1[r, ϕ] // TraditionalForm]
Print[""]
Print["r1<r≤r2:"]
Print["H_ϕ(r,ϕ)= ", Hϕ2[r, ϕ] // TraditionalForm]
```

$0 \le r \le r1:$

$$H_\phi(r,\phi) = \frac{i\, k \cos(m\,\phi)\,\left(A1e\,n1^2\,r\,u1\,J_{m-1}(r\,u1) - A1e\,n1^2\,r\,u1\,J_{m+1}(r\,u1) - 2\,A1h\,\eta 0\,m\,nef\,J_m(r\,u1)\right)}{2\,r\,u1^2}$$

$r1 < r \le r2:$

$$H_\phi(r,\phi) = -\frac{i\, k \cos(m\,\phi)\,\left(C2e\,n2^2\,r\,w2\,K_{m-1}(r\,w2) + C2e\,n2^2\,r\,w2\,K_{m+1}(r\,w2) - 2\,C2h\,\eta 0\,m\,nef\,K_m(r\,w2)\right)}{2\,r\,w2^2}$$

From the application of the boundary conditions at the core radius we obtain

In[34]:=
```
ec1 = Flatten[Coefficient[(Ez1[r1, ϕ] - Ez2[r1, ϕ]) /. Cos[m ϕ] → 1, {A1e, A1h, C2e, C2h}], 4];
ec2 = Flatten[Coefficient[(Hz1[r1, ϕ] - Hz2[r1, ϕ]) /. Sin[m ϕ] → 1, {A1e, A1h, C2e, C2h}], 4];
ec3 = Flatten[Coefficient[(Eϕ1[r1, ϕ] - Eϕ2[r1, ϕ]) /. Sin[m ϕ] → 1, {A1e, A1h, C2e, C2h}], 4];
ec4 = Flatten[Coefficient[(Hϕ1[r1, ϕ] - Hϕ2[r1, ϕ]) /. Cos[m ϕ] → 1, {A1e, A1h, C2e, C2h}], 4];
matriz = {ec1, ec2, ec3, ec4};
% // MatrixForm // TraditionalForm
```

Out[39]//TraditionalForm=

$$\begin{pmatrix} J_m(\mathrm{r1\,u1}) & 0 & -K_m(\mathrm{r1\,w2}) & 0 \\ 0 & -J_m(\mathrm{r1\,u1}) & 0 & K_m(\mathrm{r1\,w2}) \\ -\frac{i\,k\,m\,\mathrm{nef}\,J_m(\mathrm{r1\,u1})}{\mathrm{r1\,u1}^2} & \frac{i\,\eta 0\,k\,J_{m-1}(\mathrm{r1\,u1})}{2\,\mathrm{u1}}-\frac{i\,\eta 0\,k\,J_{m+1}(\mathrm{r1\,u1})}{2\,\mathrm{u1}} & -\frac{i\,k\,m\,\mathrm{nef}\,K_m(\mathrm{r1\,w2})}{\mathrm{r1\,w2}^2} & -\frac{i\,\eta 0\,k\,K_{m-1}(\mathrm{r1\,w2})}{2\,\mathrm{w2}}-\frac{i\,\eta 0\,k\,K_{m+1}(\mathrm{r1\,w2})}{2\,\mathrm{w2}} \\ \frac{i\,k\,\mathrm{n1}^2\,J_{m-1}(\mathrm{r1\,u1})}{2\,\mathrm{u1}}-\frac{i\,k\,\mathrm{n1}^2\,J_{m+1}(\mathrm{r1\,u1})}{2\,\mathrm{u1}} & -\frac{i\,\eta 0\,k\,m\,\mathrm{nef}\,J_m(\mathrm{r1\,u1})}{\mathrm{r1\,u1}^2} & \frac{i\,k\,\mathrm{n2}^2\,K_{m-1}(\mathrm{r1\,w2})}{2\,\mathrm{w2}}+\frac{i\,k\,\mathrm{n2}^2\,K_{m+1}(\mathrm{r1\,w2})}{2\,\mathrm{w2}} & -\frac{i\,\eta 0\,k\,m\,\mathrm{nef}\,K_m(\mathrm{r1\,w2})}{\mathrm{r1\,w2}^2} \end{pmatrix}$$

In order to have a non-trivial solution the determinant of the above matrix should be equal zero:

In[40]:=
```
det1 = Det[matriz] // Simplify;
% /. {BesselJ[1 + m, r1 u1] → -BesselJ[-1 + m, r1 u1] + (2 * m)/(r1 * u1) * BesselJ[m, r1 * u1],
    BesselK[1 + m, r1 w2] → BesselK[-1 + m, r1 w2] + (2 * m)/(r1 * w2) * BesselK[m, r1 * w2]};
(% / ((1/(4 r1^2 u1^4 w2^4)) k^2 η0 * BesselJ[-1 + m, r1 u1] BesselJ[m, r1 u1]
      BesselK[-1 + m, r1 w2] BesselK[m, r1 w2])) // Expand;
det1n = ((% / (4 n1^2 r1^2 u1^3 w2^3)) // Expand) /. {u1 → U1/r1, w2 → W2/r1};
Print[det1n // TraditionalForm, "  = 0"]
```

$$\frac{m^2\,\mathrm{n2}^2\,\mathrm{U1}\,J_m(\mathrm{U1})\,K_m(\mathrm{W2})}{\mathrm{n1}^2\,\mathrm{W2}^3\,J_{m-1}(\mathrm{U1})\,K_{m-1}(\mathrm{W2})}+\frac{m^2\,\mathrm{n2}^2\,J_m(\mathrm{U1})\,K_m(\mathrm{W2})}{\mathrm{n1}^2\,\mathrm{U1}\,\mathrm{W2}\,J_{m-1}(\mathrm{U1})\,K_{m-1}(\mathrm{W2})}+\frac{m^2\,\mathrm{nef}^2\,\mathrm{W2}\,J_m(\mathrm{U1})\,K_m(\mathrm{W2})}{\mathrm{n1}^2\,\mathrm{U1}^3\,J_{m-1}(\mathrm{U1})\,K_{m-1}(\mathrm{W2})}+$$
$$\frac{m^2\,\mathrm{nef}^2\,\mathrm{U1}\,J_m(\mathrm{U1})\,K_m(\mathrm{W2})}{\mathrm{n1}^2\,\mathrm{W2}^3\,J_{m-1}(\mathrm{U1})\,K_{m-1}(\mathrm{W2})}+\frac{2\,m^2\,\mathrm{nef}^2\,J_m(\mathrm{U1})\,K_m(\mathrm{W2})}{\mathrm{n1}^2\,\mathrm{U1}\,\mathrm{W2}\,J_{m-1}(\mathrm{U1})\,K_{m-1}(\mathrm{W2})}-\frac{m^2\,\mathrm{W2}\,J_m(\mathrm{U1})\,K_m(\mathrm{W2})}{\mathrm{U1}^3\,J_{m-1}(\mathrm{U1})\,K_{m-1}(\mathrm{W2})}-$$
$$\frac{m^2\,J_m(\mathrm{U1})\,K_m(\mathrm{W2})}{\mathrm{U1}\,\mathrm{W2}\,J_{m-1}(\mathrm{U1})\,K_{m-1}(\mathrm{W2})}+\frac{2\,m\,\mathrm{n2}^2\,\mathrm{U1}\,J_m(\mathrm{U1})}{\mathrm{n1}^2\,\mathrm{W2}^2\,J_{m-1}(\mathrm{U1})}+\frac{\mathrm{n2}^2\,\mathrm{U1}\,J_m(\mathrm{U1})\,K_{m-1}(\mathrm{W2})}{\mathrm{n1}^2\,\mathrm{W2}\,J_{m-1}(\mathrm{U1})\,K_m(\mathrm{W2})}+\frac{m\,\mathrm{n2}^2\,J_m(\mathrm{U1})}{\mathrm{n1}^2\,\mathrm{U1}\,J_{m-1}(\mathrm{U1})}-$$
$$\frac{m\,\mathrm{n2}^2\,K_m(\mathrm{W2})}{\mathrm{n1}^2\,\mathrm{W2}\,K_{m-1}(\mathrm{W2})}+\frac{2\,m\,\mathrm{W2}\,K_m(\mathrm{W2})}{\mathrm{U1}^2\,K_{m-1}(\mathrm{W2})}-\frac{\mathrm{W2}\,J_{m-1}(\mathrm{U1})\,K_m(\mathrm{W2})}{\mathrm{U1}\,J_m(\mathrm{U1})\,K_{m-1}(\mathrm{W2})}-\frac{m\,J_m(\mathrm{U1})}{\mathrm{U1}\,J_{m-1}(\mathrm{U1})}+\frac{m\,K_m(\mathrm{W2})}{\mathrm{W2}\,K_{m-1}(\mathrm{W2})}-\frac{\mathrm{n2}^2}{\mathrm{n1}^2}+1 \;=\; 0$$

where $U_1 = r_1\,u_1$, $W_2 = r_1\,w_2$.

If we define

$$\xi = \frac{J_m(U_1)}{U_1\,J_{m-1}(U_1)}$$

$$\chi = \frac{K_m(W_2)}{W_2\,K_{m-1}(W_2)}$$

Then the above determinant leads to a quadratic equation in ξ:

In[45]:=
```
((det1n /. { BesselJ[m, U1] → ξ * U1 * BesselJ[-1 + m, U1],
        BesselK[m, W2] → χ * W2 * BesselK[-1 + m, W2]}) * (χ * ξ)) // Expand;
tra = Collect[%, ξ^2];
tra[[3]][[2]] = Collect[tra[[3]][[2]], χ^2];
tra[[3]][[2]][[3]][[1]] = tra[[3]][[2]][[3]][[1]] // Simplify;
tra[[3]][[2]][[2]][[1]] = tra[[3]][[2]][[2]][[1]] // Simplify;
tra[[2]][[2]] = Collect[tra[[2]][[2]], χ^2];
tra[[2]][[2]][[2]][[1]] = tra[[2]][[2]][[2]][[1]] // Simplify;
Print[tra, " =0"]
```

$$-\frac{W2^2\,\chi^2}{U1^2}+\xi\left(\left(1-\frac{n2^2}{n1^2}\right)\chi+m\left(1-\frac{n2^2}{n1^2}+\frac{2\,W2^2}{U1^2}\right)\chi^2\right)+$$
$$\xi^2\left(\frac{n2^2\,U1^2}{n1^2\,W2^2}+m\left(-1+\frac{n2^2\,\left(2\,U1^2+W2^2\right)}{n1^2\,W2^2}\right)\chi+\frac{m^2\,\left(U1^2+W2^2\right)\,\left(n2^2\,U1^2-n1^2\,W2^2+nef^2\,\left(U1^2+W2^2\right)\right)\,\chi^2}{n1^2\,U1^2\,W2^2}\right)=0$$

Each of the possible solutions of this equation may be associated with an HE or EH mode. By defining:

$$c_1=\left(\frac{n2^2\,U1^2}{n1^2\,W2^2}+m\left(-1+\frac{n2^2\,(2\,U1^2+W2^2)}{n1^2\,W2^2}\right)\chi+\frac{m^2\,(U1^2+W2^2)\,(n2^2\,U1^2-n1^2\,W2^2+nef^2\,(U1^2+W2^2))\,\chi^2}{n1^2\,U1^2\,W2^2}\right)$$

$$c_2=\left(\left(1-\frac{n2^2}{n1^2}\right)\chi+m\left(1-\frac{n2^2}{n1^2}+\frac{2\,W2^2}{U1^2}\right)\chi^2\right)$$

$$c_3=-\frac{W2^2\,\chi^2}{U1^2}$$

Then the determinant will lead to two solutions of the form:

In[53]:=
```
(tra /. {(n2^2 U1^2)/(n1^2 W2^2) + m (-1 + (n2^2 (2 U1^2 + W2^2))/(n1^2 W2^2)) χ +
        1/(n1^2 U1^2 W2^2) m^2 (U1^2 + W2^2) (n2^2 U1^2 - n1^2 W2^2 + nef^2 (U1^2 + W2^2)) χ^2 → c1,
    ((1 - n2^2/n1^2) χ + m (1 - n2^2/n1^2 + (2 W2^2)/U1^2) χ^2) → c2} /. -(W2^2 χ^2)/U1^2 → c3;
Solve[% == 0, ξ]
ξ1 = %[[1]][[1]][[2]];
ξ2 = %%[[2]][[1]][[2]];
Print["ξ1=  ", ξ1]
Print["ξ2=  ", ξ2]
```

Out[54]=
$$\left\{\left\{\xi\to\frac{-c_2-\sqrt{c_2^2-4\,c_1\,c_3}}{2\,c_1}\right\},\left\{\xi\to\frac{-c_2+\sqrt{c_2^2-4\,c_1\,c_3}}{2\,c_1}\right\}\right\}$$

$$\xi_1=\frac{-c_2-\sqrt{c_2^2-4\,c_1\,c_3}}{2\,c_1}$$

$$\xi_2=\frac{-c_2+\sqrt{c_2^2-4\,c_1\,c_3}}{2\,c_1}$$

In[59]:=
$$C1 = \left(\frac{n2^2\,U1^2}{n1^2\,W2^2} + m\left(-1 + \frac{n2^2\left(2\,U1^2 + W2^2\right)}{n1^2\,W2^2}\right)\chi + \frac{1}{n1^2\,U1^2\,W2^2}\,m^2\left(U1^2 + W2^2\right)\left(n2^2\,U1^2 - n1^2\,W2^2 + nef^2\left(U1^2 + W2^2\right)\right)\chi^2\right);$$

$$C2 = \left(\left(1 - \frac{n2^2}{n1^2}\right)\chi + m\left(1 - \frac{n2^2}{n1^2} + \frac{2\,W2^2}{U1^2}\right)\chi^2\right);$$

$$C3 = -\frac{W2^2\,\chi^2}{U1^2};$$

Then we have two characteristic equations for EH and HE modes:

In[62]:=
$$Ec1 = \left(\xi 1 /. \xi 1 \to \frac{\text{BesselJ}[m, U1]}{U1 * \text{BesselJ}[m-1, U1]}\right) - \left(\left(\frac{C2}{2 * C1} * \left(1 - \text{Sqrt}\left[C2^2 - 4 * C1 * C3\right]\right)\right) /. \chi \to \frac{\text{BesselK}[m, W2]}{\text{BesselK}[m-1, W2]}\right);$$

$$Ec2 = \left(\xi 2 /. \xi 2 \to \frac{\text{BesselJ}[m, U1]}{U1 * \text{BesselJ}[m-1, U1]}\right) - \left(\left(\frac{C2}{2 * C1} * \left(1 + \text{Sqrt}\left[C2^2 - 4 * C1 * C3\right]\right)\right) /. \chi \to \frac{\text{BesselK}[m, W2]}{\text{BesselK}[m-1, W2]}\right);$$

Now we consider the specific case of a single mode fiber with 4.15 μm core radius, and 0.13 NA:

In[64]:=
```
Needs["PhysicalConstants`"]
SpeedOfLight;
clight = SpeedOfLight[[1]] * 10^6;
ϵ0 = VacuumPermittivity[[1]] * 10^-6;
μ0 = VacuumPermeability[[1]] * 10^-6;
k = 2 * Pi / λ;
ω = 2 * Pi * clight / λ;
nco = 1.445;
NA = 0.13;
ncla = Sqrt[nco^2 - NA^2];
V = k * rco * NA;
next = 1;
rco = 4.15;
rcla = 62.5;
η0 = 377;
u1c = k^2 * (nco^2 - nef^2);
U1c = rco * u1c;
w2c = k^2 * (nef^2 - ncla^2);
W2c = w2c * r1;
W2nc = w2c * r2;
w3c = k^2 * (nef^2 - next^2);
W3c = w3c * r2;
```

Characteristic Equations:

In[86]:=
```
caracCO[r1_, r2_, n1_, n2_, n3_, λ_, m_, nef_] = Ec1 /. {U1 → u1c * rco, W2 → W2c * rco};
caracCOn[r1_, r2_, n1_, n2_, n3_, λ_, m_, nef_] = Ec2 /. {U1 → u1c * rco, W2 → W2c * rco};
```

The roots or the allowed effective index values are found at the points where the functions are zero.

In[88]:=
```
Manipulate[Plot[{caracCOn[rco, rcla, nco, ncla, next, λ, 1, nef]}, {nef, ncla, nco},
  PlotRange → {{ncla, nco}, {-20, 20}}, Frame → True, FrameLabel → {"n_eff"}],
 {λ, 1.3, 1.7}, FrameLabel → "Mode HE_1m or LP_0m"]
```

Out[88]=

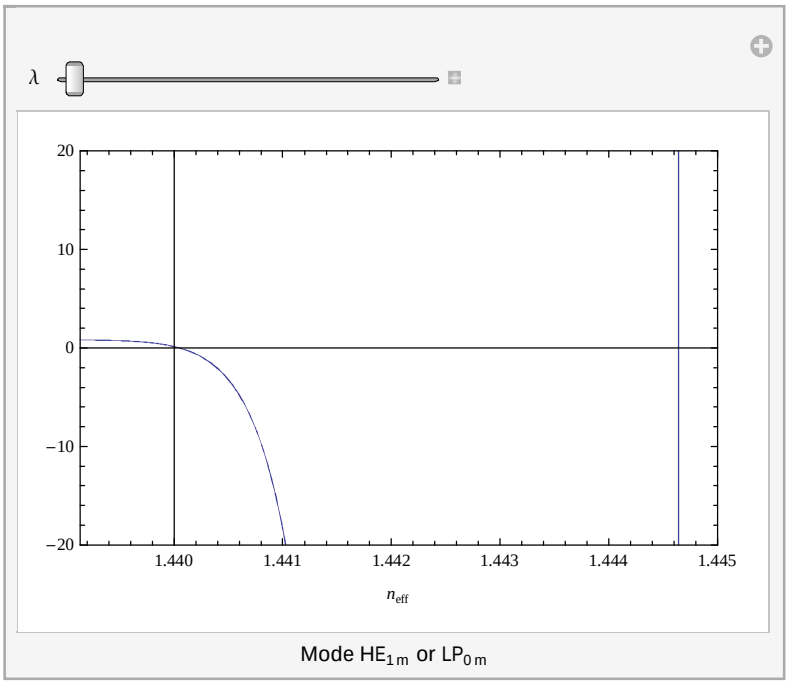


```
FindRoot[caracCOn[rco, rcla, nco, ncla, next, 1.7, 1, nef], {nef, 1.441}][[1]][[2]]
```

```
1.43992
```

Now we obtain the dispersion curve for the effective index of the fundamental core mode:

```
nefini = 1.4396931567610167;
Core = Table[
    {λ, FindRoot[caracCOn[rco, rcla, nco, ncla, next, λ, 1, nef], {nef, 1.441}][[1]][[2]]},
    {λ, 1.3, 1.7, 0.01}];
ListPlot[Core, Joined → True, Frame → True, FrameLabel →
  {"Wavelength (μm)", "Effective index n_eff"}, PlotStyle → {Black, Thick}]
```

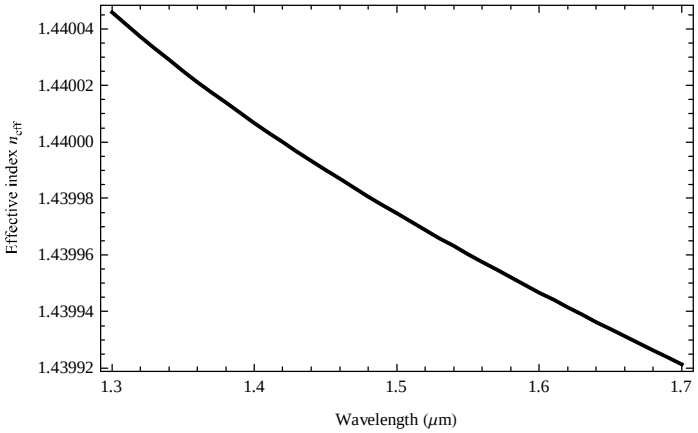

Figure A2. Dispersion curve for the fundamental core mode.

The relationship for the propagation constant which is related to the effective refraction index is the following

$$\beta = k\, n_{\text{eff}} = \frac{2\pi}{\lambda} n_{\text{eff}} \tag{0.15}$$

A.2.1.2 Cladding modes

The cladding modes in an optical fiber can be excited by a perturbation which couples part of the energy from the core mode to energy of cladding modes. There are several perturbations which causes this coupling, but in this work we will be focused in the perturbation caused by a taper made in the optical fiber. Depending of the taper dimensions and processing conditions these tapers in optical fibers can effectively couple light from the core to the cladding mode and vice versa.

The fabrication of optical fiber tapers involves removing the protective coating leading to a stripped optical fiber which has a refraction index profile such as that shown in figure A.1 (Refraction index profile for a Matched Cladding fiber). This profile comprises a core embedded in the cladding surrounded by air, due to this, unlike the core modes now it is necessary to consider a finite cladding for solving the wave equation in the whole structure.

Every clading mode will has a value in the range given by the following condition:

$$n_3 < n_{\text{eff}} < n_2 \tag{0.16}$$

Where n_3 is the refraction index in the air and n_2 is the refraction index in the cladding. It can be assumed that there is no light in the air due to the great difference between the refraction index of cladding and air.

In a tapered fiber optic the translational invariance is lost due to the variation of the whole fiber optic diameter. The ration of cladding to core radii is kept constant at the non tapered optical fiber value because when the diameter of the whole fiber decreases or increases, the cladding and core radii change by a factor of exactly the same amount and the ration of cladding to core radii remains constant.

$$S \equiv \frac{\rho_{\text{cl}}}{\rho_{\text{co}}} \quad \text{Ration core to cladding radii} \tag{0.17}$$

As the core radius varies, the normalized frequency V (which is given by equation 2.17) varies too, due to the fact that the normalised frequency is directly proportional to the core radius which depends of the longitudinal component z through the taper length.

$$V(z) = k \sqrt{\left(n_{\text{co}}^2 - n_{\text{cl}}^2\right)}\ \rho(z) \tag{0.18}$$

Where k=$\frac{2\pi}{\lambda}$ is the wavenumber in terms of the free-space wavelength λ. For this analisys it is necesary to introduce the normalised radial co-ordinate:

$$R = \frac{r}{\rho} \tag{0.19}$$

Where ρ is the core radius

Taking in consideration the three layer structure for the matched cladding profile and using the normalized radial co-ordinate, the solutions for equations 2.3 and 2.4 for every layer will be of the following form:

For the electric field

$$e_z(r, \phi) = \cos(l\,\phi) \begin{cases} A_c^e\, J_m(u_1\, R) & 0 \le R \le 1 \\ B_c^e\, J_m(u_2\, R) + C_c^e\, Y_m(u_2\, R) & 1 \le R \le \frac{\rho_{cl}}{\rho} \\ D_c^e\, K_m(w_3\, r) & R > \frac{\rho_{cl}}{\rho} \end{cases} \tag{0.20}$$

For the magnetic field

$$h_z(r, \phi) = -\sin(l\,\phi) \begin{cases} A_c^h\, J_m(u_1\, R) & 0 \le R \le 1 \\ B_c^h\, J_m(u_2\, R) + C_c^h\, Y_m(u_2\, R) & 1 \le R \le \frac{\rho_{cl}}{\rho} \\ D_c^h\, K_m(w_3\, R) & R > \frac{\rho_{cl}}{\rho} \end{cases} \tag{0.21}$$

Where A_c^e, B_c^e, C_c^e, D_c^e, A_c^h, B_c^h, C_c^h and D_c^h are constants, J_m, K_m, C_c^e, Y_m are Bessel functions, u_i and w_i are defined in equation 2.10

```
ClearAll["Global`*"]
```

The solutions when 1 ≤ neff < ncl for every layer are the following

```
F1[R_] = Ac * BesselJ[0, U * R];
F2[R_] = Bc * BesselJ[0, Q * R] + Cc * BesselY[0, Q * R];
F3[R_] = Dc * BesselK[0, T * R];
```

where U = u_1, Q = u_2 and T = w_3

The solutions are derived with respect to the normalized radial-coordinate

```
DF1[R_] = D[F1[R], R];
DF2[R_] = D[F2[R], R];
DF3[R_] = D[F3[R], R];
```

Applying boundary condition at R=1 (in the core radius), and at R=S (in the cladding radius)

```
ec1 = F1[1] - F2[1];
ec2 = DF1[1] - DF2[1];
ec3 = F2[S] - F3[S];
ec4 = DF2[S] - DF3[S];
```

Making a matrix for the solution of the equations system

```
fila1 = Coefficient[ec1, {Ac, Bc, Cc, Dc}];
fila2 = Coefficient[ec2, {Ac, Bc, Cc, Dc}];
fila3 = Coefficient[ec3, {Ac, Bc, Cc, Dc}];
fila4 = Coefficient[ec4, {Ac, Bc, Cc, Dc}];
```

```
Matriz = MatrixForm[{fila1, fila2, fila3, fila4}]
```

$$\begin{pmatrix} \text{BesselJ}[0, U] & -\text{BesselJ}[0, Q] & -\text{BesselY}[0, Q] & 0 \\ -U\,\text{BesselJ}[1, U] & Q\,\text{BesselJ}[1, Q] & Q\,\text{BesselY}[1, Q] & 0 \\ 0 & \text{BesselJ}[0, Q\,S] & \text{BesselY}[0, Q\,S] & -\text{BesselK}[0, S\,T] \\ 0 & -Q\,\text{BesselJ}[1, Q\,S] & -Q\,\text{BesselY}[1, Q\,S] & T\,\text{BesselK}[1, S\,T] \end{pmatrix}$$

Calculation of determinant matrix in several functions

```
Funcion[S_, U_, T_] = Expand[Det[Matriz[[1]]]]
```

$$
\begin{aligned}
&-Q\,U\,\text{BesselJ}[1, Q\,S]\,\text{BesselJ}[1, U]\,\text{BesselK}[0, S\,T]\,\text{BesselY}[0, Q] + \\
&\ T\,U\,\text{BesselJ}[0, Q\,S]\,\text{BesselJ}[1, U]\,\text{BesselK}[1, S\,T]\,\text{BesselY}[0, Q] + \\
&\ Q\,T\,\text{BesselJ}[0, U]\,\text{BesselJ}[1, Q]\,\text{BesselK}[1, S\,T]\,\text{BesselY}[0, Q\,S] - \\
&\ T\,U\,\text{BesselJ}[0, Q]\,\text{BesselJ}[1, U]\,\text{BesselK}[1, S\,T]\,\text{BesselY}[0, Q\,S] + \\
&\ Q^2\,\text{BesselJ}[0, U]\,\text{BesselJ}[1, Q\,S]\,\text{BesselK}[0, S\,T]\,\text{BesselY}[1, Q] - \\
&\ Q\,T\,\text{BesselJ}[0, Q\,S]\,\text{BesselJ}[0, U]\,\text{BesselK}[1, S\,T]\,\text{BesselY}[1, Q] - \\
&\ Q^2\,\text{BesselJ}[0, U]\,\text{BesselJ}[1, Q]\,\text{BesselK}[0, S\,T]\,\text{BesselY}[1, Q\,S] + \\
&\ Q\,U\,\text{BesselJ}[0, Q]\,\text{BesselJ}[1, U]\,\text{BesselK}[0, S\,T]\,\text{BesselY}[1, Q\,S]
\end{aligned}
$$

The determinant is separated into two functions f1 and f2, and then f3, f4, f5, and f6 are the determinant expresed in terms of the functions f1 and f2

$$
\begin{aligned}
\text{f1}[S\_, Q\_, U\_, T\_] = {} & Q\,U + T\,U\,\frac{\text{BesselJ}[0, Q]\,\text{BesselK}[1, S\,T]\,\text{BesselY}[0, Q\,S]}{\text{BesselJ}[1, Q\,S]\,\text{BesselK}[0, S\,T]\,\text{BesselY}[0, Q]} + \\
& Q\,T\,(\text{BesselJ}[0, Q\,S]\,\text{BesselJ}[0, U]\,\text{BesselK}[1, S\,T]\,\text{BesselY}[1, Q])\,/ \\
& \text{BesselJ}[1, Q\,S]\,\text{BesselJ}[1, U]\,\text{BesselK}[0, S\,T]\,\text{BesselY}[0, Q] + \\
& Q^2\,\frac{\text{BesselJ}[0, U]\,\text{BesselJ}[1, Q]\ \text{BesselY}[1, Q\,S]}{\text{BesselJ}[1, Q\,S]\,\text{BesselJ}[1, U]\ \text{BesselY}[0, Q]};
\end{aligned}
$$

$$
\begin{aligned}
\text{f2}[S\_, Q\_, U\_, T\_] = {} & T\,U\,\frac{\text{BesselJ}[0, Q\,S]\ \text{BesselK}[1, S\,T]}{\text{BesselJ}[1, Q\,S]\ \text{BesselK}[0, S\,T]} + \\
& Q\,T\,(\text{BesselJ}[0, U]\,\text{BesselJ}[1, Q]\,\text{BesselK}[1, S\,T]\,\text{BesselY}[0, Q\,S])\,/ \\
& \text{BesselJ}[1, Q\,S]\,\text{BesselJ}[1, U]\,\text{BesselK}[0, S\,T]\,\text{BesselY}[0, Q] + \\
& Q^2\,\frac{\text{BesselJ}[0, U]\,\text{BesselJ}[1, Q\,S]\ \text{BesselY}[1, Q]}{\text{BesselJ}[1, Q\,S]\,\text{BesselJ}[1, U]\ \text{BesselY}[0, Q]} + Q\,U\,\frac{\text{BesselJ}[0, Q]\ \ \text{BesselY}[1, Q\,S]}{\text{BesselJ}[1, Q\,S]\ \ \text{BesselY}[0, Q]};
\end{aligned}
$$

$$
\text{f3}[S\_, Q\_, U\_, T\_] = \frac{\text{f1}[S, Q, U, T] - \text{f2}[S, Q, U, T]}{\text{f1}[S, Q, U, T] + \text{f2}[S, Q, U, T]};
$$

$$
\text{f4}[S\_, Q\_, U\_, T\_] = \frac{\text{f1}[S, Q, U, T] - \text{f2}[S, Q, U, T]}{\text{f1}[S, Q, U, T]};
$$

$$
\text{f5}[S\_, Q\_, U\_, T\_] = \frac{\text{f1}[S, Q, U, T] - \text{f2}[S, Q, U, T]}{\text{f2}[S, Q, U, T]};
$$

$$
\text{f6}[S\_, Q\_, U\_, T\_] = \frac{\text{f1}[S, Q, U, T] - \text{f2}[S, Q, U, T]}{\text{f2}[S, Q, U, T] - \text{f1}[S, Q, U, T]};
$$

After having the equation, the determinant that involves the solution for the three layer optical fiber, which represents the mode solutions for the optical fiber, what is left to do is find the roods of a shuch equation. The calculation of the effective refractive index for every mode supported in the three layer optical fiber are described below.

Optical fiber data used for the calculation of the effective refractive index for every mode

```
NA = 0.2; (*SMF28*)
λ = 1.2 ;
λ1 = 1.2;
rco = 9.84 / 2;
S1 = 12.703;
rcla = S1 rco;
n2 = 1.450588;
Δ = 0.002176;
n1 = Sqrt[(-n2^2)/(2 Δ - 1)] ;
k = 2 * Pi / λ;
V1 = (V λ)/(2 Sqrt[-n2^2 + n1^2] π) * k * Sqrt[n1^2 - n2^2];
U1 = (V λ)/(2 Sqrt[-n2^2 + n1^2] π) * k * Sqrt[n1^2 - neco^2];
Q1 = (V λ)/(2 Sqrt[-n2^2 + n1^2] π) * k * Sqrt[n2^2 - neco^2];
T1 = (V λ)/(2 Sqrt[-n2^2 + n1^2] π) * k * Sqrt[neco^2 - 1];
n1
```

```
1.45375
```

Refraction index for the cladding and core fiber

```
lista1 = Table[{x, 1.450588}, {x, 0.5, 1.8, 0.1}];
lista2 = Table[{x, 1.4537548197445296}, {x, 0.5, 1.8, 0.1}];
```

In order to find the solution for the determinant it is used the graphical solution method, for this, it is plotted f1 and f2 for a normalized frecuency of 0.5 and with a wavelength of 1.2 μm to find the intersections of the function curves which represent the solutions

```
V = 0.5;
Plot[{Re[f1[S1, Q1 /. {λ → λ1, r → V λ / (2 Sqrt[-n2^2 + n1^2] π)}],
    U1 /. {λ → λ1, r → V λ / (2 Sqrt[-n2^2 + n1^2] π)}, T1 /. {λ → λ1, r → V λ / (2 Sqrt[-n2^2 + n1^2] π)}]],
  Re[f2[S1, Q1 /. {λ → λ1, r → V λ / (2 Sqrt[-n2^2 + n1^2] π)}], U1 /. {λ → λ1, r → V λ / (2 Sqrt[-n2^2 + n1^2] π)},
    T1 /. {λ → λ1, r → V λ / (2 Sqrt[-n2^2 + n1^2] π)}]]}, {neco, 1.44, 1.45},
 PlotRange → {{1.442, 1.4505}, {-1000, 1000}}, Frame → True,
 FrameLabel → {"Effective index n_eff", ""}, PlotLegends → "Expressions",
 Epilog → {PointSize[Large], Point[{1.450225695752853`, 0.495`}],
   Point[{1.4483621256990902`, 0.492`}], Point[{1.4450948787356985`, 0.4995`}]}]
```

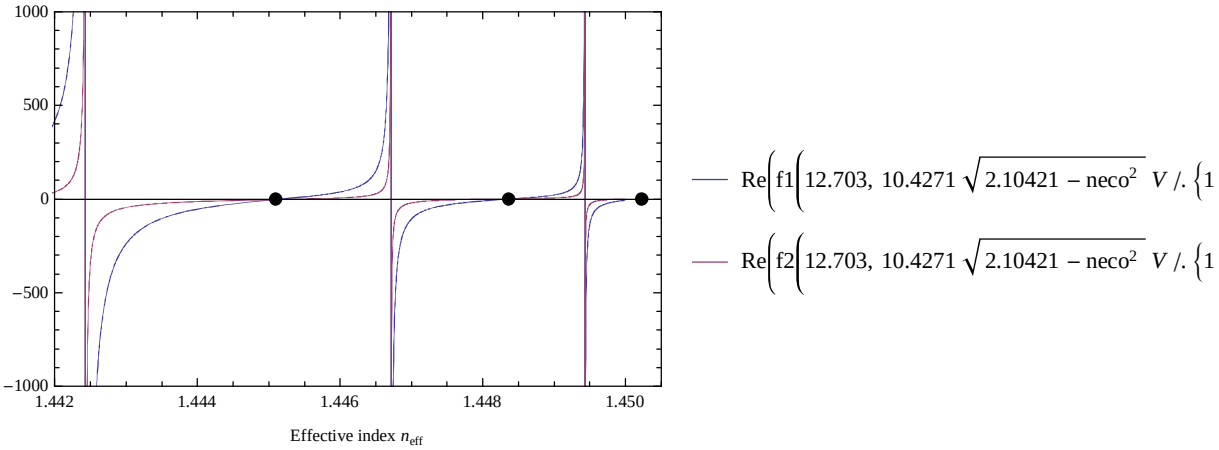

Figure A.3 Plotting of the determinant solution for the three layer structure optical fiber for finding the roots using f1 and f2 for a graphical solution method. The three black points are the roots for the LP_{01}, LP_{02}, and LP_{03} modes numbered from right to left respectively.

For the same normalized frecuency of 0.5 and with a wavelength of 1.2 μm, it is found the root for the effective refractive index of the LP_{01} mode which is the closed value to the core refraction index, due to the fact that is the mode that propagates more confined in the core.

```
V = 0.5;
Chop[FindRoot[f1[S1, Q1 /. {λ → λ1, r → V λ / (2 √(-n2^2 + n1^2) π)},
    U1 /. {λ → λ1, r → V λ / (2 √(-n2^2 + n1^2) π)}, T1 /. {λ → λ1, r → V λ / (2 √(-n2^2 + n1^2) π)}] ==
  f2[S1, Q1 /. {λ → λ1, r → V λ / (2 √(-n2^2 + n1^2) π)}, U1 /. {λ → λ1, r → V λ / (2 √(-n2^2 + n1^2) π)},
    T1 /. {λ → λ1, r → V λ / (2 √(-n2^2 + n1^2) π)}], {neco, 1.451}][[1]][[2]]]
```

```
1.45024
```

The finding of the root for the LP_{02} is shown below:

```
V = 0.5;
Chop[FindRoot[f1[S1, Q1 /. {λ → λ1, r → V λ / (2 √(-n2^2 + n1^2) π)},
    U1 /. {λ → λ1, r → V λ / (2 √(-n2^2 + n1^2) π)}, T1 /. {λ → λ1, r → V λ / (2 √(-n2^2 + n1^2) π)}] ==
  f2[S1, Q1 /. {λ → λ1, r → V λ / (2 √(-n2^2 + n1^2) π)}, U1 /. {λ → λ1, r → V λ / (2 √(-n2^2 + n1^2) π)},
    T1 /. {λ → λ1, r → V λ / (2 √(-n2^2 + n1^2) π)}], {neco, 1.448}][[1]][[2]]]
```

```
1.44844
```

The finding of the root for the LP_{03} is shown below:

```
V = 0.5;
Chop[FindRoot[f1[S1, Q1 /. {λ → λ1, r → V λ / (2 √(-n2^2 + n1^2) π)},
    U1 /. {λ → λ1, r → V λ / (2 √(-n2^2 + n1^2) π)}, T1 /. {λ → λ1, r → V λ / (2 √(-n2^2 + n1^2) π)}] ==
  f2[S1, Q1 /. {λ → λ1, r → V λ / (2 √(-n2^2 + n1^2) π)}, U1 /. {λ → λ1, r → V λ / (2 √(-n2^2 + n1^2) π)},
    T1 /. {λ → λ1, r → V λ / (2 √(-n2^2 + n1^2) π)}], {neco, 1.445}][[1]][[2]]]
```

```
1.44511
```

With the purpose of find the cladding modes it is necessary to make a perturbation. The perturbation used in this work is the taper in the optical fiber, for doing a taper in the optical fiber it is needed to vary the optical fiber radius, it is done by varying the normalized frequency, which has a diretly proporsionality with the radius of the optical fiber, as the length of the fiber increases. In the following steps it is calculated the refractive indexes (roots of the determinant) for the LP_{01}, LP_{02}, LP_{03}, LP_{04}, and LP_{05} as the parameter V (normalized frequency) is increased.

Searching of roots from the first mode LP_{01} or HE_{11}

```
neffs1 = {};
vbusqueda1 = {1.45023};
V = 0.49;
For[j = 0, j ≤ 250, j++,
  V = V + 0.005;
  R = Chop[
    FindRoot[f3[S1, Q1 /. {λ → λ1, r → V λ / (2 √(-n2^2 + n1^2) π)}, U1 /. {λ → λ1, r → V λ / (2 √(-n2^2 + n1^2) π)},
      T1 /. {λ → λ1, r → V λ / (2 √(-n2^2 + n1^2) π)}] == 0, {neco, vbusqueda1[[j + 1]]}][[1]][[2]]];
  neffs1 = Append[neffs1, {V, R}];
  vbusqueda1 = Append[vbusqueda1, R];
 ];
```

Searching of roots from the second mode LP_{02} or HE_{12}

```
neffs2 = {};
vbusqueda2 = {1.446};
V = 0.49;
For[j = 0, j ≤ 600, j++,
  V = V + 0.002;
  R = Chop[
    FindRoot[f3[S1, Q1 /. {λ → λ1, r → V λ / (2 √(-n2^2 + n1^2) π)}, U1 /. {λ → λ1, r → V λ / (2 √(-n2^2 + n1^2) π)},
      T1 /. {λ → λ1, r → V λ / (2 √(-n2^2 + n1^2) π)}] == 0, {neco, vbusqueda2[[j + 1]]}][[1]][[2]]];
  neffs2 = Append[neffs2, {V, R}];
  vbusqueda2 = Append[vbusqueda2, R];
 ];
```

Searching of roots from the third mode LP_{03} or HE_{13}

```
neffs3 = {};
vbusqueda3 = {1.445};
V = 0.499;
For[j = 0, j ≤ 593, j++,
  V = V + 0.0005;
  R = Chop[
    FindRoot[f3[S1, Q1 /. {λ → λ1, r → V λ / (2 √(-n2^2 + n1^2) π)}, U1 /. {λ → λ1, r → V λ / (2 √(-n2^2 + n1^2) π)},
      T1 /. {λ → λ1, r → V λ / (2 √(-n2^2 + n1^2) π)}] == 0, {neco, vbusqueda3[[j + 1]]}][[1]][[2]]];
  neffs3 = Append[neffs3, {V, R}];
  vbusqueda3 = Append[vbusqueda3, R];
 ];
```

```
V = 0.9;
neffs3a =
  FindRoot[f4[S1, Q1 /. {λ → λ1, r → V λ / (2 √(-n2^2 + n1^2) π)}, U1 /. {λ → λ1, r → V λ / (2 √(-n2^2 + n1^2) π)},
    T1 /. {λ → λ1, r → V λ / (2 √(-n2^2 + n1^2) π)}] == 0, {neco, 1.447}][[1]][[2]];
neffs3 = Append[neffs3, {V, neffs3a}];
```

```
V = 1.0;
neffs3b =
  FindRoot[f4[S1, Q1 /. {λ → λ1, r → V λ / (2 √(-n2^2 + n1^2) π)}, U1 /. {λ → λ1, r → V λ / (2 √(-n2^2 + n1^2) π)},
    T1 /. {λ → λ1, r → V λ / (2 √(-n2^2 + n1^2) π)}] == 0, {neco, 1.447}][[1]][[2]];
neffs3 = Append[neffs3, {V, neffs3b}];
```

```
V = 1.1;
neffs3c =
  FindRoot[f5[S1, Q1 /. {λ → λ1, r → V λ / (2 √(-n2^2 + n1^2) π)}, U1 /. {λ → λ1, r → V λ / (2 √(-n2^2 + n1^2) π)},
    T1 /. {λ → λ1, r → V λ / (2 √(-n2^2 + n1^2) π)}] == 0, {neco, 1.45}][[1]][[2]];
neffs3 = Append[neffs3, {V, neffs3c}];
```

```
V = 1.2;
neffs3d =
  FindRoot[f5[S1, Q1 /. {λ → λ1, r → V λ / (2 Sqrt[-n2^2 + n1^2] π)}, U1 /. {λ → λ1, r → V λ / (2 Sqrt[-n2^2 + n1^2] π)},
      T1 /. {λ → λ1, r → V λ / (2 Sqrt[-n2^2 + n1^2] π)}] == 0, {neco, 1.45}][[1]][[2]];
neffs3 = Append[neffs3, {V, neffs3d}];
V = 1.4;
neffs3e =
  FindRoot[f5[S1, Q1 /. {λ → λ1, r → V λ / (2 Sqrt[-n2^2 + n1^2] π)}, U1 /. {λ → λ1, r → V λ / (2 Sqrt[-n2^2 + n1^2] π)},
      T1 /. {λ → λ1, r → V λ / (2 Sqrt[-n2^2 + n1^2] π)}] == 0, {neco, 1.45}][[1]][[2]];
neffs3 = Append[neffs3, {V, neffs3e}];
V = 1.7;
neffs3f =
  FindRoot[f5[S1, Q1 /. {λ → λ1, r → V λ / (2 Sqrt[-n2^2 + n1^2] π)}, U1 /. {λ → λ1, r → V λ / (2 Sqrt[-n2^2 + n1^2] π)},
      T1 /. {λ → λ1, r → V λ / (2 Sqrt[-n2^2 + n1^2] π)}] == 0, {neco, 1.4501525577461194`}][[1]][[2]];
neffs3 = Append[neffs3, {V, neffs3f}];
```

Searching of roots from the fourth mode LP_{04} or HE_{14}

```
neffs4 = {};
vbusqueda4 = {1.44};
V = 0.49;
For[j = 0, j ≤ 150, j++,
  V = V + 0.005;
  R = Chop[
    FindRoot[f5[S1, Q1 /. {λ → λ1, r → V λ / (2 Sqrt[-n2^2 + n1^2] π)}, U1 /. {λ → λ1, r → V λ / (2 Sqrt[-n2^2 + n1^2] π)},
        T1 /. {λ → λ1, r → V λ / (2 Sqrt[-n2^2 + n1^2] π)}] == 0, {neco, vbusqueda4[[j + 1]]}][[1]][[2]]];
  neffs4 = Append[neffs4, {V, R}];
  vbusqueda4 = Append[vbusqueda4, R];
 ];
```

```
V = 1.5;
neffs4a = Quiet[
    FindRoot[f6[S1, Q1 /. {λ → λ1, r → V λ / (2 √(-n2^2 + n1^2) π)}, U1 /. {λ → λ1, r → V λ / (2 √(-n2^2 + n1^2) π)},
        T1 /. {λ → λ1, r → V λ / (2 √(-n2^2 + n1^2) π)}] == 0, {neco, 1.44952}][[1]][[2]]];
neffs4 = Append[neffs4, {V, neffs4a}];
V = 1.7;
neffs4b = Quiet[
    FindRoot[f6[S1, Q1 /. {λ → λ1, r → V λ / (2 √(-n2^2 + n1^2) π)}, U1 /. {λ → λ1, r → V λ / (2 √(-n2^2 + n1^2) π)},
        T1 /. {λ → λ1, r → V λ / (2 √(-n2^2 + n1^2) π)}] == 0, {neco, 1.44972}][[1]][[2]]];
neffs4 = Append[neffs4, {V, neffs4b}];
```

Searching of roots from the fifth mode LP_{04} or HE_{125}

```
neffs5 = {};
vbusqueda5 = {1.43};
V = 0.49;
For[j = 0, j ≤ 125, j++,
  V = V + 0.01;
  R = Chop[
    FindRoot[f3[S1, Q1 /. {λ → λ1, r → V λ / (2 √(-n2^2 + n1^2) π)}, U1 /. {λ → λ1, r → V λ / (2 √(-n2^2 + n1^2) π)},
      T1 /. {λ → λ1, r → V λ / (2 √(-n2^2 + n1^2) π)}] == 0, {neco, vbusqueda5[[j + 1]]}][[1]][[2]]];
  neffs5 = Append[neffs5, {V, R}];
  vbusqueda5 = Append[vbusqueda5, R];
 ];
```

Plotting of the refractive index for the first five $LP_{0\,m}$ modes when a taper perturbation is current

```
Show[ListPlot[{neffs1, neffs2, neffs3, neffs4, neffs5, lista1, lista2}, Joined → True,
  Frame → True, FrameLabel → {"Parameter, V(z)", "Effective index, n_eff"},
  PlotRange → {1.44, 1.455}, PlotStyle → {Thick}],
 Graphics[{Text["for λ = 1.2 μm", {1.5, 1.442}], Text["LP05", {0.73, 1.441}],
   Text["LP04", {0.65, 1.443}], Text["LP03", {0.57, 1.445}], Text["LP02", {0.56, 1.448}],
   Text["LP01", {1.6, 1.452}], Text["Core refractive index", {1.144, 1.4542}],
   Text["Cladding refractive index", {0.7, 1.451}],
   Text["Standard single mode fiber", {1.5, 1.443}]}]]
```

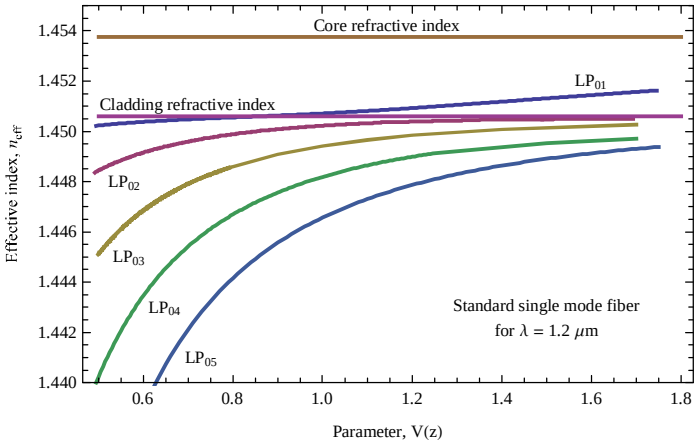

Fig.A.4 Refractive index for the first five cladding modes as a function of the parameter V, which is directly proportional to the core radius, for a range from V = 0.49 (ρ = 0.9765 μm) to V = 1.8 (ρ = 3.5873 μm) when λ=1.2 um.

From figure A.4 we can notice that the high order modes n_{eff} values are below of the cladding index which means that the condition of equation 2.16 is carried out, thus, these high order modes are cladding modes. However, the efective index of the fundamental mode, which is guided in the core at the begining of the taper, moves below the cladding index at a V(z) value of 0.84 (this value corresponds to a core radius value of 1.67μm for a wavelength of 1.2μm) which is called the core cladding transition value V_{cc} (Core mode cutoff[2]) due to the fact that the fundamental mode which is guided in the core before the taper becomes a cladding mode when V(z) = V_{cc}. Thus, for V values slightly greater than V_{cc} the mode will be propagated in the core and guidance is determaned only by the interface core-cladding, while for V values smaller than V_{cc} the mode will be propagated in the cladding and guidance is determined by the interface cladding air and the effects of the interface core cladding can be neglected (due to the weak guided condition $n_{co} \approx n_{cl}$) and it can be setting $n_{co} = n_{cl}$, hence, the three layer refraction index profile is approximeted to a two layer refracion index profile with a core of refraction index $n_{co} = n_{cl}$ and cladding of refraction index equal to 1 which is the refraction index of the air. And the developmen for finding the solutions for the efective refraction indexes is exactly the same that was used for the calculation of the core modes in section A.2.1.1 but now with a core radius equal to the cladding radius and the $n_{co} = n_{cl}$ and $n_{cl} = 1$.

A.3 Coupling between modes

As it was mentioned in section A.2.1.2 for the cladding modes, coupling can be done by a perturbation in the optical fiber waveguide, and for this work, the perturbation I will take in acount for coupling is tapering optical fiber. There are two kind of coupling depending on the taper symmetry. If the taper is axisymmetric the fundamental core mode will couple energy only to modes that have the same azimuthal symmetry and this coupling will be predominant to that cladding mode which has the higher and closest propagation constant to that of the fundamental mode, (i. e. coupling between the LP_{01} core mode and the LP_{02} core mode). Otherwise if the taper is nonaxisymetric, such is the case of bent tapers, the coupling will be predominantly between the fundamental core mode LP_{01} and the closest propagation constant to the fundamental mode, i.e. to the LP_{11} cladding mode. This work will be focused on a axisymetric tapers.

when an optical fiber is tapered it is presented a break of the translational invariance from the uniform fiber. This leads to the possibility of a loss of the power from the fundamental core mode. This possibility means if the taper is or is not an adiabatic taper. A taper is adiabatic if there is no power loss from the fundamental core mode which is guided through the fiber. On the other hand, if power loss from the fundamental core mode is presented the taper will be a nonadiabatic taper and this power loss is represented by coupling from the fundamental core mode to cladding modes of a finite cladding optical fiber.

Depending on the geometrical characteristics of the optical fiber taper, it will be determined wether or not the taper is geometrical enough to generate coupling between modes. If the taper angle $\Omega(z)$, see figure 1.2, is small enough everywhere to make sure that there is insignificant power losses from the core mode as it is propagated through the tapered length of the optical fiber, it will take into account that we are dealing with an adiabatic optical fiber taper. Otherwise, if the taper angle is not small enough there will be power losses from the fundamental core and

it will lead us to a nonadiabatic optical fiber taper.

In the literature, there is two basic criteria based on simple physical principles to determine wether or not a taper is adiabatic. They are length-scale criterion (section 1.3.1 of chapter 1) and weak power transfer criterion.

The simple physical principle for the weak power transfer criterion is based in the fact that the loss from the fundamental mode in a tapered optical fiber can be quantified by the superposition of the fundamental and cladding local modes. The amplitude for each mode is related by a set of coupled local mode equations [3-5].

If it is assumed that the coupling is predominantly to the mode with a propagation constant closest to that of the fundamental mode, then the amplitudes of this to modes are well aproximated by [5]

$$a_1(z) = a_1(0)\exp\left\{i\int_0^z \beta_1(z')\,dz'\right\} \tag{0.22}$$

$$a_2(z) = a_1(0)\exp\left\{i\int_0^z \beta_2(z')\,dz'\right\}\int_0^z C(z')\exp\left\{i\int_0^{z'}(\beta_1(z'')-\beta_2(z''))\,dz''\right\}dz' \tag{0.23}$$

where a_1 is the amplitude of the fundamental mode at the bigining of the taper, and C is the coupling coefficient between the two modes and it is given by

$$C = \frac{1}{2}\frac{k}{\beta_1-\beta_2}\frac{d\rho}{dz}\frac{1}{n_{co}}\frac{\int_{A\infty}\psi_1\psi_2\frac{\partial n^2}{\partial\rho}\,dA}{\sqrt{\int_{A\infty}\psi_1^2\,dA\int_{A\infty}\psi_2^2\,dA}} \tag{0.24}$$

Where n_{co} is the maximum core index, $\rho=\rho(z)$ is the local core radius, $k=2\pi/\lambda$ is the free space wavenumber, λ is the free space wavelength, $A\infty$ is the infinite cross-section and ψ_1, ψ_2 are the scalar wave equation fields for the fundamental and second modes.

If we look at the second integral of equation (2.23), $\int_0^z C(z')\exp\left\{i\int_0^{z'}(\beta_1(z'')-\beta_2(z''))\,dz''\right\}dz'$, it is worth noting that the exponential factor causes an oscilation in fase of the same integral. Thus the fraction of power of the second mode depends on this oscilation term, the maximum power transfer is after half a beat length ($\pi/(\beta_1-\beta_2)$).

At the end of the taper (z = L) the fraction of power for the second mode will be small and we have the following inequality

$$\left|\int_0^z C(z')\exp\left\{i\int_0^{z'}(\beta_1(z'')-\beta_2(z''))\,dz''\right\}dz'\right| << 1 \tag{0.25}$$

At this distance the integrals are approximately constant and the inequality is reduced to

$$\frac{Cz_b}{\pi} << 1 \tag{0.26}$$

A delineation criterion for determining whether a taper is so or not comes from assuming $Cz_b=1$ and knowing that the the fraction of power if the second mode is given by the square of the left hand of equation 2.26, hence, the loss is $1/\pi^2$ which is approximately 10% per half beat length [2].

When the index profile has a step variation, the coupling coefficient C is proportional to the relative taper slope $(1/\rho)d\rho/dz$ [5]; therefore the supposition $Cz_b=1$ can be recast in the explicit form [4,6]

$$\Omega = \frac{1}{\vec{C}}\frac{\rho(\beta_1-\beta_2)}{2\pi} \tag{0.27}$$

Where $\vec{C}$ is the dimensionless normalised coupling coefficient given by

$$\vec{C} = \frac{C\rho}{\frac{d\rho}{dz}} \tag{0.28}$$

A.3.1 Coupling coefficient calculation

Considering the coupling coefficient in the following way

$$C_{mn} = -\frac{1}{2}\frac{1}{n_{m,eff}-n_{n,eff}}\frac{d\rho}{dz}\frac{(n_1^2-n_2^2)\psi_{core}(r_1)\psi_{clad}(r_1)+(n_2^2-n_3^2)\psi_{core}(r_2)\psi_{clad}(r_2)}{\left(\int_0^r \Psi_{core}^2(r)\;r\;dr\right)^{1/2}\left(\int_0^r \Psi_{clad}^2(r)\,r\;dr\right)^{1/2}} \tag{0.29}$$

For a spesific shape of a conical optical fiber starting from the initial dimentions of the untapered optical fiber such as the cladding and core radius, we will have the final core and cladding radius with smaller values than the initial dimentions which forms the decreasing conical

reduction for the optical fiber taper. The final cladding radius is setting manually in the software of the Vytran glass procesor, and the core radius will be proportianal to the same reduction than the cladding had, for the conservation of mass, following a linear proportionality it follows for the final tapered core radius.

$$r_{\text{final core}} = r_{\text{final clad}}\left(\frac{r_{\text{initial core}}}{r_{\text{clad initial}}}\right) \tag{0.30}$$

Another importan parameter is the conical optical fiber taper length which can be set manually just as the cladding radius, it is in the software of the Vytran glass procesor.

Taking an optical fiber conical shape with a starter untapered cladding radius of 125μm, a final cladding diameter of 30 μm, and a conical optical fiber taper length of 1000 μm (see Fig A.3). The initial core diameter is the untapered core radius equal to 1.76073 and the final core radius (μm) and the slope (dimensionless) of the conical optical fiber tapered will be:

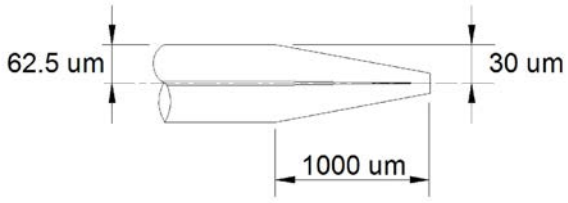

Figure A5. Fiber conical shape cor the calculation of rhe coupling coefficient

```
r_finalcore = rco * 30 / 62.5
```

```
2.3616
```

```
mco1 = (rco - r_finalcore) / 1000
```

$$\frac{4.92 - r_{\text{core final}}}{1000}$$

With the aim of calculating the coupling coefficient it is needed to know the mode fields, for this, once that the effective indixes are found it is posible to find the constants which are in the field solutions in every layer of the optical fiber. Assuming Ac=1 all the constants are found and the solution field for the core and cladding layers of the optical fiber are the following become as it follows:

In the core layer for values of $n_{\text{eff}} < n_{\text{co}}$ the field will be

```
F01A[U_, R_] = BesselJ[0, U * R];

F02A[U_, R_] = BesselJ[0, U * R];
```

In the cladding layer for core modes which has values in the range of $n_{\text{cl}} < n_{\text{eff}} < n_{\text{co}}$ the field will be

```
F01B[U_, W_, R_] =
  (-U BesselJ[1, U] BesselK[0, W] + W BesselJ[0, U] BesselK[1, W]) * BesselI[0, W * R] +
   (W BesselI[1, W] BesselJ[0, U] + U BesselI[0, W] BesselJ[1, U]) * BesselK[0, W * R];
```

In the cladding layer for cladding modes which has values in the range of $1 < n_{\text{eff}} < n_{\text{cl}}$ the field will be

```
F02B[U_, Q_, R_] =
  (1/2 π (U BesselJ[1, U] BesselY[0, Q] - Q BesselJ[0, U] BesselY[1, Q])) * BesselJ[0, Q * R] +
   (1/2 π (Q BesselJ[0, U] BesselJ[1, Q] - U BesselJ[0, Q] BesselJ[1, U])) * BesselY[0, Q * R];
```

Remembering the core to cladding ration

```
S1 = rcla / rco;
```

The definition of the modal parameters for the field solution are

```
U1n[λ2_, R_, r1_, n1a_, neco_] = r1 * R * 2 π / λ2 * Sqrt[n1a^2 - neco^2];
W1n[λ2_, R_, r1_, n2a_, neco_] = r1 * R * 2 π / λ2 * Sqrt[neco^2 - n2a^2];
Q1n[λ2_, R_, r1_, n2a_, neco_] = r1 * R * 2 π / λ2 * Sqrt[n2a^2 - neco^2];
```

With the intention of have two Arrays with the same size for the LP_{01} and LP_{02} effective refraction indexes, polynomial adjustments are made just as follows below:

For the mode LP_{01} a polynomial fit of order 5 for the array, normalized frequency parameter "V" versus effective refraction index, is made as follows

```
neffs1;
neffs1fit = Fit[neffs1, {1, x, x^2, x^3, x^4, x^5}, x]
```

$$1.44694 + 0.0147403\,x - 0.0247844\,x^2 + 0.0207865\,x^3 - 0.00820351\,x^4 + 0.00123912\,x^5$$

Plotting this adjusment

```
Show[Plot[{neffs1fit}, {x, 0.666, 1.743}, Frame → True,
  AxesOrigin → Automatic, Axes → False, PlotStyle → {Thick},
  PlotLegends → "Expressions", FrameLabel → {"Normalized frequency parameter V(z)",
    "Effective refraction index for the LP01 mode"}],
 Graphics[{Text["for λ = 1.2 μm", {1.5, 1.4507}],
   Text["Standard single mode fiber", {1.5, 1.4508}]}]]
```

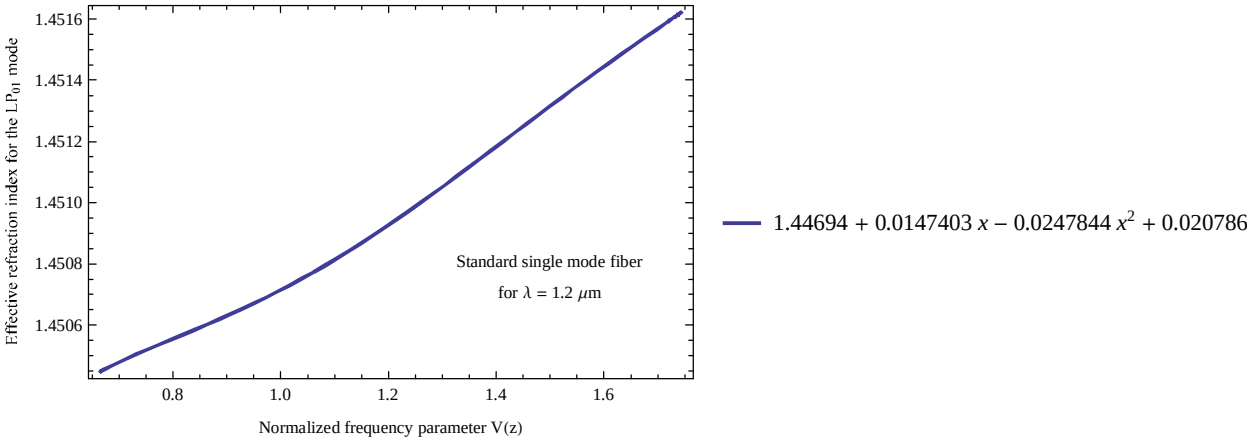

Figure A.6. Plot of the polynomial fit of 5 order for the normalized frequency parameter "V" versus effective refraction index of the LP_{01} mode, where the abscissa is effective refraction index for the LP_{01} mode and the odinate is the normalizad frequency parameter "V".

Plotting both the original array and the polynomial fit to see if the polynomial fit is adjusted well to the original array

```
neffs1fittab = Table[{x, neffs1fit}, {x, 0.492, 1.692, 0.002}];
```

```
Show[ListPlot[{neffs1fittab, neffs1}, Frame → True, PlotLegends → {"Fit", "Original array"},
  FrameLabel → {"Normalized frequency parameter V(z)",
    "Effective refraction index for the LP01 mode"}],
 Graphics[{Text["for λ = 1.2 μm", {1.5, 1.4505}],
   Text["Standard single mode fiber", {1.5, 1.4506}]}]]
```

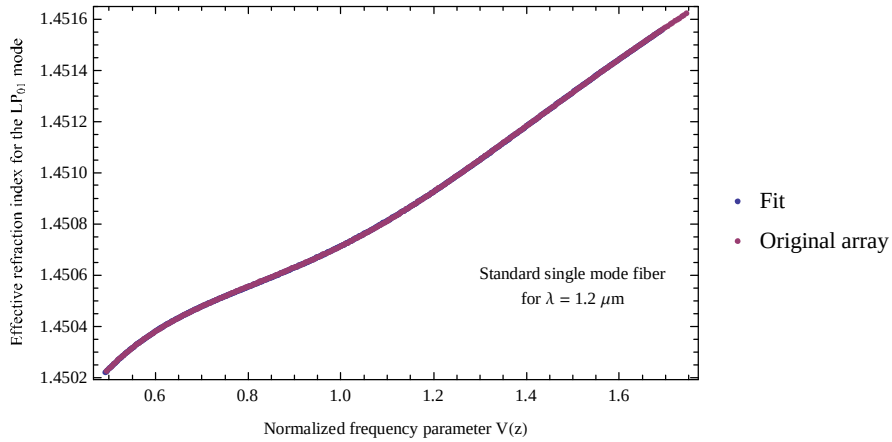

Figure A.7. Plot of both arrays, fit and original for the effective refraction index of the LP_{01} vs. the normalized frequency parameter "V".

In figure 2.12 it is noticed that the polinomial fit of order 5 for the refractive index of the LP_{01} vs. parameter "V" is a good adjustment, both curves match one above the other.

It is done the a same polynomial fit f order 4 for the LP_{02} mode

```
neffs2;
neffs2fit = Fit[neffs2, {1, x, x^2, x^3, x^4, x^5, x^6}, x]
```

$$1.43067 + 0.0861193\,x - 0.169473\,x^2 + 0.185867\,x^3 - 0.116634\,x^4 + 0.0390985\,x^5 - 0.00542584\,x^6$$

$$1.4306710237747478` + 0.08611929174241299`\,x - 0.1694728153499366`\,x^2 + 0.18586741184912703`\,x^3 - 0.11663373333133929`\,x^4 + 0.03909847864575565`\,x^5 - 0.0054258410494067546`\,x^6$$

$$1.43067 + 0.0861193\,x - 0.169473\,x^2 + 0.185867\,x^3 - 0.116634\,x^4 + 0.0390985\,x^5 - 0.00542584\,x^6$$

```
neffs2fittab = Table[{x, neffs2fit}, {x, 0.492, 1.692, 0.002}];
```

```
Show[ListPlot[{neffs2fittab, neffs2}, Frame → True,
  FrameLabel → {"Normalized frequency parameter V(z)",
    "Effective refraction index for the LP02 mode"}, PlotLegends →
   {"Fit", "Original array"}], Graphics[{Text["for λ = 1.2 μm", {1.4, 1.4490}],
   Text["Standard single mode fiber", {1.4, 1.4492}]}]]
```

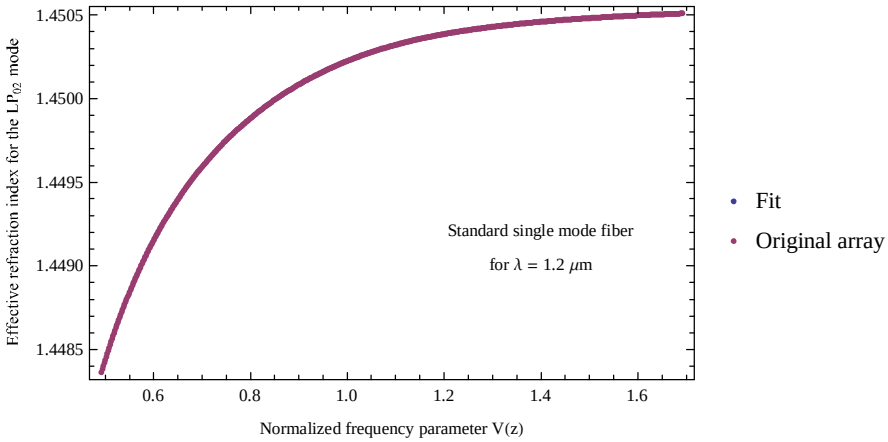

Figure A.8. Plot of both arrays, fit and original for the effective refraction index of the LP_{02} vs. the normalized frequency parameter "V".

In figure A.8 it is noticed that the polinomial fit of order 5 for the refractive index of the LP_{02} vs. parameter "V" is a good adjustment, both curves match one above the other as in figure A7.

For the evaluation of the coupling coefficient, the equation (0.29) is separated in three parts as follows

$$C_{1-2} = \text{Part1} * \text{Part2} * \text{Part3} \tag{0.31}$$

The solution for every part is:

$$\text{Part1} = -\frac{1}{2}\frac{d\rho}{dz}\frac{1}{n_{eff1} - n_{eff2}} \tag{0.32}$$

```
Part1 = Table[{neffs2[[iii]][[1]],
    -(0.5 * mco1 / (neffs1fittab[[iii]][[2]] - neffs2[[iii]][[2]]))}, {iii, 1, 601}];
```

$$\text{Part2} = \frac{1}{\left(\sqrt{\int_0^r \psi_{core}^2(r)\, r\, dr}\right)\left(\sqrt{\int_0^r \psi_{clad}^2(r)\, r\, dr}\right)} \tag{0.33}$$

```
Part2 = Chop[Table[{neffs2[[iii]][[1]],
    1 / ((Sqrt[NIntegrate[R * F01A[U1n[λ1, R, rco, n1, neffs1fittab[[iii]][[2]]], R]^2,
          {R, 0, 1}] + NIntegrate[R * F01B[U1n[λ1, R, rco, n1, neffs1fittab[[iii]][[2]]],
          W1n[λ1, R, rco, n2, neffs1fittab[[iii]][[2]]], R]^2, {R, 1, S1}]]) *
      (Sqrt[NIntegrate[R * F02A[U1n[λ1, R, rco, n1, neffs2[[1]][[2]]], R]^2, {R, 0, 1}] +
        NIntegrate[R * F02B[U1n[λ1, R, rco, n1, neffs2[[1]][[2]]], Q1n[λ1, R,
          rco, n2, neffs2[[1]][[2]]], R]^2, {R, 1, S1}]]))}, {iii, 1, 601}]];
```

$$\text{Part3} = (n_1^2 - n_2^2)\psi_{core}(r_1)\psi_{clad}(r_1) + (n_2^2 - n_3^2)\psi_{core}(r_2)\psi_{clad}(r_2)$$

```
Part3 = Chop[Table[{neffs2[[iii]][[1]],
    (((n1^2 - n2^2) * F01A[U1n[λ1, 1, rco, n1, neffs1fittab[[iii]][[2]]], 1] *
        F02A[U1n[λ1, 1, rco, n1, neffs2[[1]][[2]]], 1]) +
      ((n2^2 - 1) * F01B[U1n[λ1, S1, rco, n1, neffs1fittab[[iii]][[2]]], W1n[λ1, S1, rco,
          n2, neffs1fittab[[iii]][[2]]], S1] * F02B[U1n[λ1, S1, rco, n1, neffs2[[1]][[2]]],
        Q1n[λ1, S1, rco, n2, neffs2[[1]][[2]]], S1]))}, {iii, 1, 601}]];
```

The coupling coefficient will be:

```
coumplingcoefficient = Table[{neffs2[[iii]][[1]](*Parametro V*),
    Part1[[iii]][[2]] * Part2[[iii]][[2]] * Part3[[iii]][[2]]}, {iii, 1, 601}];

Show[ListPlot[{coumplingcoefficient},
  AxesLabel → {"Parameter V(z)", "Coupling coefficient"},
  PlotStyle → {Black, Thick}, Frame → True,
  FrameLabel → {"Normalized frequency parameter V(z)", "Coupling coefficient"}],
 Graphics[{Text["λ = 1.2 μm", {1.4, 0.015}], Text["Taper slope = 0.0025584", {1.4, 0.013}],
   Text["Length transition = 1000 μm", {1.4, 0.011}]}]]
```

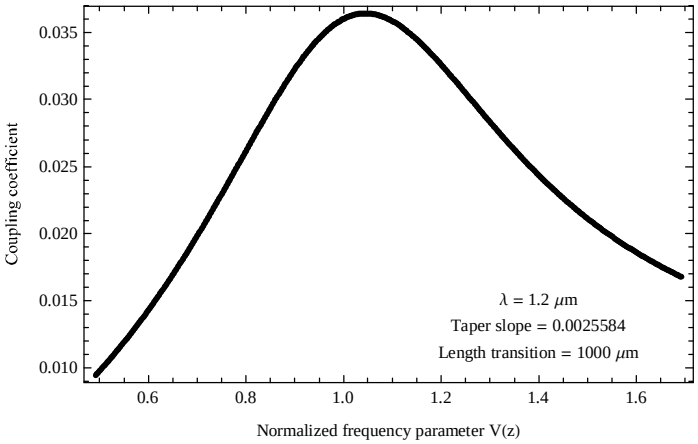

Figure A9. Coupling coefficient vs. the normalized frequency parameter for a wavelength of 1.2 μm and a taper slope of 0.0025584 corresponding to a transition length of 1000 μm.

The coupling coefficient has a directly dependence on the slope of the tapered optical fiber, if the transition length is small the slope will be large and vice versa if the transition length is large the slope will be small, in the following calculation it is shown how the coupling coefficient displays different responces for several transitions lengths (100, 500, 1000, 1500, 2000, 2500, 3000, 3500, 4000, 4500, 5000, 5500, 6000, 6500, and 7000 μm) at a wavelength of 1.2 μm.

List of the different slopes for every transition length 100, 500, 1000, 1500, 2000, 2500, 3000, 3500, 4000, 4500, 5000, 5500, 6000, 6500, and 7000 μm

$$\text{int} = \frac{\text{rco} - r_{\text{final core}}}{100};$$

$$\text{mco2} = \text{Flatten}\left[\text{Append}\left[\{\text{int}\}, \text{Table}\left[\frac{\text{rco} - r_{\text{final core}}}{\text{transsiotionlength}}, \{\text{transsiotionlength}, 500, 7000, 500\}\right]\right]\right]$$

$$\left\{\frac{1}{100}(4.92 - r_{\text{core final}}), \frac{1}{500}(4.92 - r_{\text{core final}}), \frac{4.92 - r_{\text{core final}}}{1000}, \frac{4.92 - r_{\text{core final}}}{1500}, \frac{4.92 - r_{\text{core final}}}{2000}, \frac{4.92 - r_{\text{core final}}}{2500}, \frac{4.92 - r_{\text{core final}}}{3000}, \frac{4.92 - r_{\text{core final}}}{3500}, \frac{4.92 - r_{\text{core final}}}{4000}, \frac{4.92 - r_{\text{core final}}}{4500}, \frac{4.92 - r_{\text{core final}}}{5000}, \frac{4.92 - r_{\text{core final}}}{5500}, \frac{4.92 - r_{\text{core final}}}{6000}, \frac{4.92 - r_{\text{core final}}}{6500}, \frac{4.92 - r_{\text{core final}}}{7000}\right\}$$

The coupling coefficient splited in three parts for the calculation is shown in equation (2.34)

$$C_{1-2} = -\frac{1}{2}\frac{d\rho}{dz}\frac{1}{n_{eff1} - n_{eff2}} * \frac{1}{\left(\sqrt{\int_0^r \psi_{core}^2(r)\, r\, dr}\right)\left(\sqrt{\int_0^r \psi_{clad}^2(r)\, r\, dr}\right)} * \left(n_1^2 - n_2^2\right)\psi_{core}(r_1)\,\psi_{clad}(r_1) + \left(n_2^2 - n_3^2\right)\psi_{core}(r_2)\,\psi_{clad}(r_2) \tag{0.34}$$

Calculation of the coupling coefficient for the diferents slopes is as follows

```
couplingcoefficientslope = Chop[ParallelTable[{neffs2[[iii]][[1]],
     -(0.5 * mco2[[k]] / (neffs1fittab[[iii]][[2]] - neffs2[[iii]][[2]])) * (1 /
        ((Sqrt[NIntegrate[R * F01A[U1n[λ1, R, rco, n1, neffs1fittab[[iii]][[2]]], R]^2, {R,
                0, 1}] + NIntegrate[R * F01B[U1n[λ1, R, rco, n1, neffs1fittab[[iii]][[2]]],
                  W1n[λ1, R, rco, n2, neffs1fittab[[iii]][[2]]], R]^2, {R, 1, S1}]]) *
          (Sqrt[NIntegrate[R * F02A[U1n[λ1, R, rco, n1, neffs2[[1]][[2]]], R]^2,
              {R, 0, 1}] + NIntegrate[R * F02B[U1n[λ1, R, rco, n1, neffs2[[1]][[2]]],
                Q1n[λ1, R, rco, n2, neffs2[[1]][[2]]], R]^2, {R, 1, S1}]]))) *
       (((n1^2 - n2^2) * F01A[U1n[λ1, 1, rco, n1, neffs1fittab[[iii]][[2]]], 1] *
           F02A[U1n[λ1, 1, rco, n1, neffs2[[1]][[2]]], 1]) +
         ((n2^2 - 1) * F01B[U1n[λ1, S1, rco, n1, neffs1fittab[[iii]][[2]]],
            W1n[λ1, S1, rco, n2, neffs1fittab[[iii]][[2]]], S1] *
           F02B[U1n[λ1, S1, rco, n1, neffs2[[1]][[2]]], Q1n[λ1, S1, rco, n2,
             neffs2[[1]][[2]]], S1])), mco2[[k]]}, {k, 1, 15}, {iii, 1, 601}]];

coupling100 = Table[{couplingcoefficientslope[[1]][[dd]][[1]],
    couplingcoefficientslope[[1]][[dd]][[2]]}, {dd, 1, 601}];

coupling500 = Table[{couplingcoefficientslope[[2]][[dd]][[1]],
    couplingcoefficientslope[[2]][[dd]][[2]]}, {dd, 1, 601}];

coupling1000 = Table[{couplingcoefficientslope[[3]][[dd]][[1]],
    couplingcoefficientslope[[3]][[dd]][[2]]}, {dd, 1, 601}];

coupling1500 = Table[{couplingcoefficientslope[[4]][[dd]][[1]],
    couplingcoefficientslope[[4]][[dd]][[2]]}, {dd, 1, 601}];

coupling2000 = Table[{couplingcoefficientslope[[5]][[dd]][[1]],
    couplingcoefficientslope[[5]][[dd]][[2]]}, {dd, 1, 601}];

coupling2500 = Table[{couplingcoefficientslope[[6]][[dd]][[1]],
    couplingcoefficientslope[[6]][[dd]][[2]]}, {dd, 1, 601}];

coupling3000 = Table[{couplingcoefficientslope[[7]][[dd]][[1]],
    couplingcoefficientslope[[7]][[dd]][[2]]}, {dd, 1, 601}];

coupling3500 = Table[{couplingcoefficientslope[[8]][[dd]][[1]],
    couplingcoefficientslope[[8]][[dd]][[2]]}, {dd, 1, 601}];

coupling4000 = Table[{couplingcoefficientslope[[9]][[dd]][[1]],
    couplingcoefficientslope[[6]][[dd]][[2]]}, {dd, 1, 601}];

coupling4500 = Table[{couplingcoefficientslope[[10]][[dd]][[1]],
    couplingcoefficientslope[[10]][[dd]][[2]]}, {dd, 1, 601}];

coupling5000 = Table[{couplingcoefficientslope[[11]][[dd]][[1]],
    couplingcoefficientslope[[11]][[dd]][[2]]}, {dd, 1, 601}];

coupling5500 = Table[{couplingcoefficientslope[[12]][[dd]][[1]],
    couplingcoefficientslope[[12]][[dd]][[2]]}, {dd, 1, 601}];

coupling6000 = Table[{couplingcoefficientslope[[13]][[dd]][[1]],
    couplingcoefficientslope[[13]][[dd]][[2]]}, {dd, 1, 601}];

coupling6500 = Table[{couplingcoefficientslope[[14]][[dd]][[1]],
    couplingcoefficientslope[[14]][[dd]][[2]]}, {dd, 1, 601}];
```

```
coupling7000 = Table[{couplingcoefficientslope[[14]][[dd]][[1]],
    couplingcoefficientslope[[14]][[dd]][[2]]}, {dd, 1, 601}];
```

The coupling coefficient vs. the normalized frequency parameter "V" for the transition length of 100 μm is shown in figure 2.15

```
Show[ListPlot[{coupling100}, AxesLabel → {"Parameter V(z)", "Coupling coefficient"},
  PlotRange → All, Frame → True, FrameLabel → {"Parameter V(z)", "Coupling coefficient"}],
 Graphics[{Text["λ = 1.2 μm", {1.4, 0.17}], Text["Taper slope = 0.025584", {1.4, 0.15}],
   Text["Length transition = 100 μm", {1.4, 0.13}]}]]
```

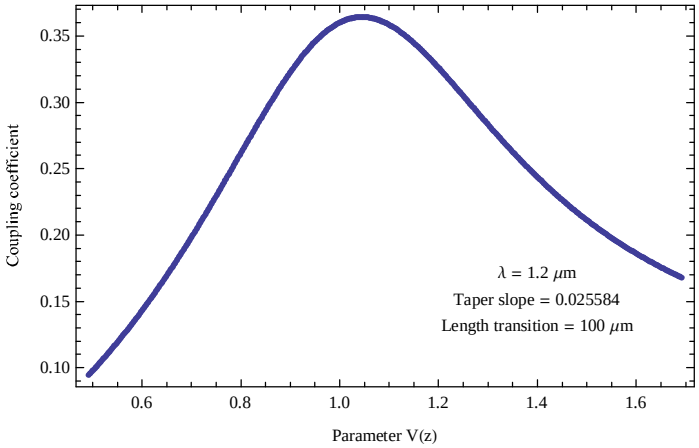

Figure A10. Coupling coefficient vs. the normalized frequency parameter for a wavelength of 1.2 μm and a taper slope of 0.025584 corresponding to a transition length of 100 μm.

```
Show[ListPlot[{coupling500, coupling1000, coupling1500, coupling2000,
   coupling2500, coupling3000, coupling3500, coupling4000, coupling4500,
   coupling5000, coupling5500, coupling6000, coupling6500, coupling7000},
  Frame → True, FrameLabel → {"Parameter V(z)", "Coupling coefficient"},
  PlotLegends → {"500 μm of transition length", "1000 μm of transition length",
    "1500 μm of transition length", "2000 μm of transition length",
    "2500 μm of transition length", "3000 μm of transition length",
    "3500 μm of transition length", "4000 μm of transition length",
    "4500 μm of transition length", "5000 μm of transition length",
    "5500 μm of transition length", "6000 μm of transition length",
    "6500 μm of transition length", "7000 μm of transition length"},
  PlotRange → All], Graphics[{Text["λ = 1.2 μm", {1.48, 0.06374}]}]]
```

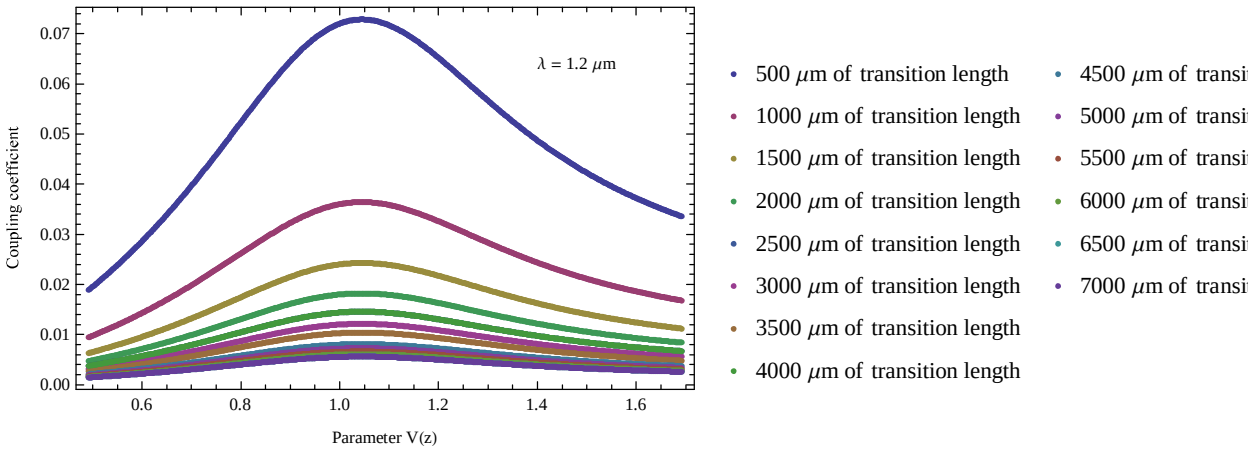

Figure A11. Coupling coefficient vs. the normalized frequency parameter for a wavelength of 1.2 μm and a taper slopes of 0.025584, 0.0051168, 0.0025584, 0.0017056 ,0.0012792, 0.00102336, 0.0008528, 0.000730971, 0.0006396, 0.000568533, 0.00051168, 0.000465164, 0.0004264, 0.0003936, 0.000365486

corresponding to a transition lengths of 100, 500, 1000, 1500, 2000, 2500, 3000, 3500, 4000, 4500, 5000, 5500, 6000, 6500, and 7000 μm.

From figures A9-11, it is noticed that as the transition length is increased (or more accurately the taper slope decreases) the coupling coefficient decreases, which means that the longer is the transition length the more adiabatic is the taper.

A.4 Light propagation through a biconical tapered fiber

The field on a perturbed optical fiber, such as a tapered fiber, at a determined z position can be expressed as the superposition of the complite set of bound and radiation mode fields of the unperturbed optical fiber [1]. One only mode of all the modes is not satisfactory for the Maxwell equations for the perturbed fiber, and the perturbed fields must be distributed between all modes of the set. This distribution varies with positions along the fiber and is described by a set of coupled mode equations, wich determine the amplitude of every mode [7-9].

A.4.1 Coupled local mode equations

The coupling mode equations are obtained by substituying a modal expansion of the fields for the perturbed fiber into Maxwell equations, wich results in a set of coupled differential equation of first order with dependence on the length z. This set of coupled mode equations is a reformulation of the Maxwel equations, which means that they describe the exactly field of the perturbed fiber. However, this new reformulation comprised by those coupled differential equations for the Maxwell equations do not have an analytical solution, Nevertheless, assuming only two modes in the superposition, wich, in our case, it can be implicit by the reason of taking in consideration what is explined in section A.3, the solution of the resulting set of equations will be uncomplicated and there will be simple perturbation solutions.

If the electric field is expresed as

$$E(x,\ y,\ z) = \sum_n b_n(z)\ \hat{e}_n(x,\ y,\ \beta(z)) \tag{0.35}$$

Where $\hat{e}_n$ denotes the orthonormal local-mode electric field for the nth local mode, $b_n(z)$ is the amplitud and phase-dependence of the scalar mode, and the sum denotes the superposition of all the bound and radiation modes.

Hence, the Maxwell equation can be reformulated as a set of coupled local-mode equations of the form [1]

$$\frac{d\ b_m}{d\ z} - i\beta_m\ b_m = \sum_n C_{\mathrm{mn}}\ b_n \tag{0.36}$$

Where C_{mn} are the coupling coefficients between the mth and nth local modes

Restricting equation 2.35 to only bound modes is a good approximation for finite-cladding
fibres which support a large number of cladding modes. This provides a reasonably complete basis for representation of the total field [2].

Taking into accound only two local-modes the equation 2.36 becomes into the next two equations

$$\frac{d\ b_1}{d\ z} - i\beta_1\ b_1 = C_{12}\ b_2 \tag{0.37}$$

$$\frac{d\ b_2}{d\ z} - i\beta_2\ b_2 = C_{21}\ b_1 \tag{0.38}$$

Where the coupling coefficient C_{12} = - C_{21}

A.4.2 Solution of the local mode equations for two modes for a simulation of propagation light through a tapered optical fiber

The equations for solving in this section are the equations 0.37 and 0.38, which correspond to the reformulation of the Maxwell equations for a system which is adequately represented by the case where only two local modes will be interecting with each other, by means of power exchange between them caused by a perturbation in the optical fiber , their solution describes the precise field of a perturbed fiber.

In order to find the spectral response of the propagation ligth through a tapered fiber it will be solved the system equation formed by equations 0.37 and 0.38 using the Runge-Kutta method.

Definition of the wavelength range, it will be from 1.2 μm to 1.6 μm

```
λλ = Table[wavelength, {wavelength, 1.2, 1.6, 0.001}];

Length[λλ]

401
```

Finding the effective refractive inder for all the wavelengths in the range and for frequency normalized “V” vaues from 0.5 to 1.7

```
(*neffs1λ={};
V=0.49;
For[l=1,l≤ 401,l++,λ2=λλ[[l]];
 vbusqueda1λ=
  {Chop[FindRoot[f1[S1,Q1/.{λ→λ2,r→ V λ2/(2 √(-n2^2+n1^2) π)},U1/.{λ→λ2,r→ V λ2/(2 √(-n2^2+n1^2) π)},T1/.{λ→λ2,
          r→ V λ2/(2 √(-n2^2+n1^2) π)}]==f2[S1,Q1/.{λ→λ2,r→ V λ2/(2 √(-n2^2+n1^2) π)},U1/.{λ→λ2,r→ V λ2/(2 √(-n2^2+n1^2) π)},
        T1/.{λ→λ2,r→ V λ2/(2 √(-n2^2+n1^2) π)}],{neco,1.451}][[1]][[2]]]};

 For[j=0,j≤250,j++,
  V=V+0.005;
  R=Chop[FindRoot[f3[S1,Q1/.{λ→λ2,r→ V λ2/(2 √(-n2^2+n1^2) π)},U1/.{λ→λ2,r→ V λ2/(2 √(-n2^2+n1^2) π)},
          T1/.{λ→λ2,r→ V λ2/(2 √(-n2^2+n1^2) π)}]==0,{neco,vbusqueda1[[j+1]]}][[1]][[2]]];
  neffs1λ=Append[neffs1λ,{λ2,V,R}];
  vbusqueda1λ=Append[vbusqueda1λ,R];
 ];V=0.49;];*)
(*neffs1λ>>"neffs1λ";*)
(*neffs2λ={};

V=0.49;
For[l=1,l≤ 401,l++,λ2=λλ[[l]];
 vbusqueda1λ=
  {Chop[FindRoot[f1[S1,Q1/.{λ→λ2,r→ V λ2/(2 √(-n2^2+n1^2) π)},U1/.{λ→λ2,r→ V λ2/(2 √(-n2^2+n1^2) π)},T1/.{λ→λ2,
          r→ V λ2/(2 √(-n2^2+n1^2) π)}]==f2[S1,Q1/.{λ→λ2,r→ V λ2/(2 √(-n2^2+n1^2) π)},U1/.{λ→λ2,r→ V λ2/(2 √(-n2^2+n1^2) π)},
        T1/.{λ→λ2,r→ V λ2/(2 √(-n2^2+n1^2) π)}],{neco,1.451}][[1]][[2]]]};
 For[j=0,j≤600,j++,
  V=V+0.002;
  R=Chop[FindRoot[f3[S1,Q1/.{λ→λ2,r→ V λ2/(2 √(-n2^2+n1^2) π)},U1/.{λ→λ2,r→ V λ2/(2 √(-n2^2+n1^2) π)},
          T1/.{λ→λ2,r→ V λ2/(2 √(-n2^2+n1^2) π)}]==0,{neco,vbusqueda2[[j+1]]}][[1]][[2]]];
  neffs2λ=Append[neffs2λ,{λ2,V,R}];
  vbusqueda2λ=Append[vbusqueda2λ,R];
 ];V=0.49;];*)
(*neffs2λ>>"neffs2λ";*)
```

```
neff1 = << neffs1λ;
A = Interpolation[neff1]
B[Xr_, Yl_] = A[Xr, Yl]
```

```
InterpolatingFunction[{{1.2, 1.6}, {0.495, 1.745}}, <>]
```

```
InterpolatingFunction[{{1.2, 1.6}, {0.495, 1.745}}, <>][Xr, Yl]
```

```
neff2 = << neffs2λ;
F = Interpolation[neff2]
G[xr_, yl_] = F[xr, yl]
```

```
InterpolatingFunction[{{1.2, 1.6}, {0.492, 1.692}}, <>]
```

```
InterpolatingFunction[{{1.2, 1.6}, {0.492, 1.692}}, <>][xr, yl]
```

Calculating the coupling coefficients for the diferent wavelengths for a length transition of 100 μm

```
mco2[[1]]
```

```
0.025584
```

```
λλ = Table[wavelength, {wavelength, 1.2, 1.6, 0.001}];
C12 = {};


Coup = Chop[ParallelTable[{λλ[[ll]], neffs2[[iii]][[1]],
     -(0.5 * mco2[[1]] / (neffs1fittab[[iii]][[2]] - neffs2[[iii]][[2]])) *
      (1 / ((Sqrt[NIntegrate[
                R * F01A[U1n[λλ[[ll]], R, rco, n1, neffs1fittab[[iii]][[2]]], R]^2, {R, 0, 1}] +
              NIntegrate[R * F01B[U1n[λλ[[ll]], R, rco, n1, neffs1fittab[[iii]][[2]]],
                  W1n[λλ[[ll]], R, rco, n2, neffs1fittab[[iii]][[2]]], R]^2, {R, 1, S1}]]) *
           (Sqrt[NIntegrate[R * F02A[U1n[λλ[[ll]], R, rco, n1, neffs2[[1]][[2]]], R]^2,
               {R, 0, 1}] + NIntegrate[R * F02B[U1n[λλ[[ll]], R, rco, n1, neffs2[[1]][[2]]],
                  Q1n[λλ[[ll]], R, rco, n2, neffs2[[1]][[2]]], R]^2, {R, 1, S1}]]))) *
      (((n1^2 - n2^2) * F01A[U1n[λλ[[ll]], 1, rco, n1, neffs1fittab[[iii]][[2]]], 1] *
          F02A[U1n[λλ[[ll]], 1, rco, n1, neffs2[[1]][[2]]], 1]) +
        ((n2^2 - 1) * F01B[U1n[λλ[[ll]], S1, rco, n1, neffs1fittab[[iii]][[2]]],
           W1n[λλ[[ll]], S1, rco, n2, neffs1fittab[[iii]][[2]]], S1] *
          F02B[U1n[λλ[[ll]], S1, rco, n1, neffs2[[1]][[2]]], Q1n[λλ[[ll]], S1,
            rco, n2, neffs2[[1]][[2]]], S1]))}, {ll, 1, 401}, {iii, 1, 601}]]
```

```
(*C12>>"C12trans100";*)
```

```
de = Flatten[Coup]
```

```
N[Length[de] / 3]
```

```
241001.
```

```
copling = ArrayReshape[de, {241001, 3}];
```

```
copling >> "C12trans100"
```

```
coupling = << C12trans100;
```

```
Ff = Interpolation[coupling]
Cte12[xr_, yl_] = Ff[xr, yl]
```

```
InterpolatingFunction[{{1.2, 1.6}, {0.492, 1.692}}, <>]
```

```
InterpolatingFunction[{{1.2, 1.6}, {0.492, 1.692}}, <>][xr, yl]
```

```
Vv[r_] = 2 π / 1.21 Sqrt[(-n2^2 + n1^2)] r;

ParallelNeeds["DifferentialEquations`NDSolveProblems`"];
ParallelNeeds["DifferentialEquations`NDSolveUtilities`"];
```

mco1 is for a length transition of 1000 μm

```
ycod1[x_] = rco - mco2[[1]] * x;

ClassicalRungeKutta[___]["Step"[f_, t_, h_, y_, yp_]] := Block[{deltay, k1, k2, k3, k4},
   k1 = yp; k2 = f[t + 1 / 2 h, y + 1 / 2 h k1]; k3 = f[t + 1 / 2 h, y + 1 / 2 h k2];
   k4 = f[t + h, y + h k3]; deltay = h (1 / 6 k1 + 1 / 3 k2 + 1 / 3 k3 + 1 / 6 k4); {h, deltay}];
```

This defines the function for computing the coefficients to a desired precision to using the Runge-Kutta method for solving the diferential equations.

```
Fehlbergamat = {
   {1 / 4},
   {3 / 32, 9 / 32},
   {1932 / 2197, -7200 / 2197, 7296 / 2197},
   {439 / 216, -8, 3680 / 513, -845 / 4104}, {-8 / 27, 2, -3544 / 2565, 1859 / 4104, -11 / 40}};
Fehlbergbvec = {25 / 216, 0, 1408 / 2565, 2197 / 4104, -1 / 5, 0};
Fehlbergcvec = {1 / 4, 3 / 8, 12 / 13, 1, 1 / 2};
Fehlbergevec = {-1 / 360, 0, 128 / 4275, 2197 / 75240, -1 / 50, -2 / 55};

FehlbergCoefficients[4, p_] :=
  N[{Fehlbergamat, Fehlbergbvec, Fehlbergcvec, Fehlbergevec}, p];

ClassicalRungeKutta[___]["Step"[f_, t_, h_, y_, yp_]] := Block[{deltay, k1, k2, k3, k4},
   k1 = yp; k2 = f[t + 1 / 2 h, y + 1 / 2 h k1]; k3 = f[t + 1 / 2 h, y + 1 / 2 h k2];
   k4 = f[t + h, y + h k3]; deltay = h (1 / 6 k1 + 1 / 3 k2 + 1 / 3 k3 + 1 / 6 k4); {h, deltay}];

solu1 = ParallelTable[
   res = Quiet[NDSolve[{A1'[z] - I * (2 * Pi / (λλ[[i]])) * B[(λλ[[i]]), Vv[ycod1[z]]] * A1[z] -
           Cte12[(λλ[[i]]), Vv[ycod1[z]]] * B1[z] == 0,
         B1'[z] - I * (2 * Pi / (λλ[[i]])) * G[(λλ[[i]]), Vv[ycod1[z]]] * B1[z] +
           Cte12[(λλ[[i]]), Vv[ycod1[z]]] * A1[z] == 0, A1[0] == 1, B1[0] == 0}, {A1, B1},
        {z, 0, 100}, Method → {"ExplicitRungeKutta", "Coefficients" → FehlbergCoefficients,
          "DifferenceOrder" → 4, "EmbeddedDifferenceOrder" → 5,
          "StiffnessTest" → False}, MaxSteps → 10^1 000 000]][[1]],
   {i,
    1,
    401}];

Plot[Abs[solu1[[1]][[1]][[2]][z]], {z, 0, 100}]


Plot[Abs[solu1[[1]][[2]][[2]][z]], {z, 0, 100}]


ListPlot[Table[{λλ[[ii]], Abs[solu1[[ii]][[1]][[2]][100]]}, {ii, 1, 401}],
 Joined → True, PlotRange → {All, All}, Frame → True]


ListPlot[Table[{λλ[[ii]], Abs[solu1[[ii]][[2]][[2]][100]]}, {ii, 1, 401}],
 Joined → True, PlotRange → {All, All}, Frame → True]
```

```
solu2A = Table[{λλ[[i]], Abs[solu1[[i]][[1]][[2]][100]]}, {i, 1, 401}];
solu2B = Table[{λλ[[i]], Abs[solu1[[i]][[2]][[2]][100]]}, {i, 1, 401}];
ListPlot[{Abs[solu2A], Abs[solu2B]}, Joined → True, PlotRange → {All, All}, Frame → True]
```

References

[1] Snyder, A.W., Love, J., Chapman and Hall “Optical Waveguide Theory”, 1984,

[2] J. D. Love, W. M. Henrry, W. J. Stewart, R. J. Black, S. Lacroix, F. Gonthier, “Tapered single mode fiberes and devices Part 1: Adiabaticity criteria”, IEE Proceedings-J Vol.138, No 5, October 1991

[3] Black, R.J., Gonthier, F., Lacroix, S., and Love, J.D.,”Tapered single mode fibers and devices: II Local-mode power evolution”, IEE Proc. J, 1991, 38, (5), pp 355-364.

[4] Henry , W.M., “Tapered optical waveguides and metal-clad polarisers”, Australian National University, 1989)

[5] Snyder A.W., and Love, J.D., “Optical waveguide theory ”, Chapman and hall, London,1983.

[6] Black, R.J. Gonthier , F., Lacroix, S., Lapierre, J., and Bures, J."Tapered fibers: an overview", Symposium on Fibre optics and optoelectronics, O-E/Fibres'87, Tekippe, San Diego, 1987, pp 2-19

[7] Snyder, A. W., “Coupled-mode theory for optical fibers”, J. Opt. Soc. Am., 62, 1267-77, 1972.

[8] Marcuse, D., “Coupled mode theory for round optical fibers”, Bell Syst. Tech. J., 52, 817-18, 1973.

[9] Marcuse, D., “Theory of Dielectric Optical Waveguides”, Academic Press, New York, p. 101, 1974.

PUBLICATIONS

1. **Compact optical fiber curvature sensor based on concatenating two tapers**
   Authors D Monzon-Hernandez, A Martinez-Rios, I Torres-Gomez, G Salceda-Delgado, Publication date 2011/11/15, Journal Optics letters, Volume 36, Issue 22, Pages 4380-4382, Publisher Optical Society of America, Cited by 38

2. **Optical microfiber mode interferometer for temperature-independent refractometric sensing**
   Authors G Salceda-Delgado, D Monzon-Hernandez, A Martinez-Rios, GA Cardenas-Sevilla, J Villatoro, Publication date 2012/6/1, Journal Optics letters, Volume 37, Issue 11, Pages 1974-1976, Publisher Optical Society of America, Cited by 30

3. **Tailoring Mach–Zehnder comb-filters based on concatenated tapers**
   Authors Guillermo Salceda-Delgado, Alejandro Martinez-Rios, David Monzón-Hernández Publication date 2013/3/1, Journal Journal of Lightwave Technology, Volume 31, Issue 5 Pages 761-767, Publisher IEEE, Cited by 7

4. **Multiple continuous-wave and pulsed modes of a figure-of-eight fibre laser**
   Authors O Pottiez, A Martinez-Rios, D Monzon-Hernandez, G Salceda-Delgado, JC Hernandez-Garcia, B Ibarra-Escamilla, EA Kuzin, Publication date 2013/3/1, Journal Laser Physics, Volume 23, Issue 3, Pages 035103, Publisher IOP Publishing, Cited by 6

5. **Random period arc-induced long-period fiber gratings**
   Authors A Martinez-Rios, I Torres-Gomez, D Monzon-Hernandez, G Salceda-Delgado, VM Duran-Ramirez, G Anzueto-Sanchez, Publication date 2012/6/30, Journal Optics & Laser Technology, Volume 44, Issue 4, Pages 1176-1179, Publisher Elsevier, Cited by 6

6. **Robust optical fiber bending sensor to measure frequency of vibration**
   Authors Arturo Ignacio Hernández-Serrano, Guillermo Salceda-Delgado, David Moreno-Hernández, Alejandro Martínez-Ríos, David Monzón-Hernández, Publication date 2013/9/30 Journal Optics and Lasers in Engineering, Volume 51, Issue 9, Pages 1102-1105, Publisher Elsevier

7. **An intrinsic fiber-optic single loop micro-displacement sensor**
   Authors Alejandro Martinez-Rios, David Monzon-Hernandez, Ismael Torres-Gomez, Guillermo Salceda-Delgado, Publication date 2012/1/4, Journal Sensors, Volume 12, Issue 1, Pages 415-428, Publisher Molecular Diversity Preservation International, Cited by 5

8. **Optimization of multicore fiber for high-temperature sensing**
   Authors Amy Van Newkirk, Enrique Antonio-Lopez, Guillermo Salceda-Delgado, Rodrigo Amezcua-Correa, Axel Schülzgen, Publication date 2014/8/15, Journal Optics letters, Volume 39 Issue 16, Pages 4812-4815, Publisher Optical Society of America, Cited by 4

9. **Multiwavelength switching of an EDFL by using a fixed fiber-comb filter and a broadband tunable S-bent fiber filter**
   Authors A Martinez-Rios, G Anzueto-Sanchez, D Monzon-Hernandez, G Salceda-Delgado, J Castrellon-Uribe, Publication date 2014/6/30, Journal Optics & Laser Technology, Volume 58 Pages 197-201, Publisher Elsevier, Cited by 4

10. **Arc-induced long-period fiber gratings inscribed in asymmetric transition tapers**
    Authors Alejandro Martínez-Rios, Guillermo Salceda-Delgado, David Monzón-Hernández, Gilberto Anzueto-Sánchez, Publication date 2013/8/1, Journal Optical Engineering, Volume 52 Issue 8, Pages 086111-086111, Publisher International Society for Optics and Photonics, Cited by 3

11. **Long-period cascaded fiber taper filters**
    Authors A Martinez-Rios, G Salceda-Delgado, JA Guerrero-Viramontes, Publication date 2014/2/10, Journal Applied optics, Volume 53, Issue 5, Pages 944-950, Publisher Optical Society of America, Cited by 1

12. **Raman response function and Raman fraction of phosphosilicate fibers**
    Authors Guillermo Salceda-Delgado, Alejandro Martinez-Rios, Boaz Ilan, David Monzon-Hernandez, Publication date 2012/11/1, Journal Optical and Quantum Electronics, Volume 44 Issue 14, Pages 657-671, Publisher Springer US, Cited by 1

13. **Simple method for measuring the cleave angle of optical fiber facets by using the nodal points of a cylindrical lens**
    AuthorsVictor M Durán-Ramírez, Alejandro Martínez-Ríos, Guillermo Salceda-Delgado, Ismael Torres-Gómez, Publication date 2012/5/1, Journal Optical Engineering, Volume 51, Issue 5 Pages 059702-1-059702-5, Publisher International Society for Optics and Photonics, Cited by 1

14. **Compact fiber-optic curvature sensor based on super-mode interference in a seven-core fiber**
    Authors G Salceda-Delgado, A Van Newkirk, JE Antonio-Lopez, A Martinez-Rios, A Schülzgen, R Amezcua Correa, Publication date 2015/4/1, Journal Optics letters, Volume 40, Issue 7, Pages 1468-1471, Publisher Optical Society of America

15. **Compact Sensors Based on Cascaded Single-Mode–Multimode–Single-Mode Fiber Structures**
    Authors David Monzón-Hernández, Alejandro Martínez-Ríos, Guillermo Salceda-Delgado, Joel Villatoro, Publication date 2013/3/1, Journal Applied Physics Express, Volume 6, Issue 3, Pages 032502, Publisher IOP Publishing

16. **Multicore Fiber Sensors for Simultaneous Measurement of Force and Temperature**
    Authors Amy Van Newkirk, Enrique Antonio-Lopez, Guillermo Salceda-Delgado, Mohammad Umar Piracha, Rodrigo Amezcua Correa, Axel Schulzgen, Publisher IEEE

CONGRESS

1. **Optical Fiber curvature sensors based on single mode-7 core-single mode fiber structures**
   Authors Guillermo Salceda, Amy Van Newkirk, Jose E Antonio-Lopez, Axel Schulzgen, Rodrigo Amezcua-Correa, Publication date 2014/7/27, Conference Optical Sensors, Pages SeW3C. 2, Publisher Optical Society of America, Cited by 1

2. **Optical fiber sensor to measure the bending of a flexible sheet**
   Authors Guillermo Salceda-Delgado, Alejandro Martínez-Ríos, David Monzón-Hernández, Publication date 2012/6/13, Conference 10TH INTERNATIONAL CONFERENCE ON VIBRATION MEASUREMENTS BY LASER AND NONCONTACT TECHNIQUES-AIVELA 2012 Volume 1457, Issue 1, Pages 419-425, Publisher AIP Publishing, Cited by 1

3. **Multicore Optical Fiber Point Sensors**
   Authors Amy Van Newkirk, Guillermo Salceda-Delgado, J Enrique Antonio-Lopez, Rodrigo Amezcua-Correa, Axel Schulzgen, Publication date 2014/10/19, Conference Frontiers in Optics Pages FTu4B. 3, Publisher Optical Society of America

4. **Supermode Interference in Multicore Fiber Optimized for use in Sensing Applications**
   Authors Amy Van Newkirk, Enrique Antonio-Lopez, Guillermo Salceda-Delgado, Rodrigo Amezcua-Correa, Axel Schulzgen, Publication date 2014/7/27, Conference Specialty Optical Fibers, Pages SoW2B. 4, Publisher Optical Society of America

5. **Multiplexed High Temperature Sensor Based on Multicore Fiber**
   Authors Jose E Antonio-Lopez, Guillermo Salceda-Delgado, Amy Van Newkirk, Axel Schulzgen, Rodrigo Amezcua-Correa, Publication date 2014/7/27, Conference Optical Sensors, Pages SeW4C. 2, Publisher Optical Society of America

6. **High Temperature Sensor based on Supermode Interference in Multicore Fiber**
   Authors Amy Van Newkirk, Zeinab Sanjabi Eznaveh, Enrique Antonio-Lopez, Guillermo Salceda-Delgado, Axel Schulzgen, Rodrigo Amezcua-Correa, Publication date 2014/6/8, Conference CLEO: Science and Innovations, Pages SM2N. 7, Publisher Optical Society of America

7. **Arc-induced long-period fiber gratings inscribed in asymmetric adiabatic tapers**
   Authors Alejandro Martínez-Rios, David Monzón-Hernández, Guillermo Salceda-Delgado
   Publication date 2013/3/11, Conference SPIE OPTO, Pages 86210L-86210L-6, Publisher International Society for Optics and Photonics

8. **Raman Response Function of Phosphosilicate Fiber**
   Authors Alejandro Martinez-Rios, Guillermo Salceda-Delgado, Ismael Torres-Gomez, Victor Manuel Duran-Ramirez, Publication date 2011/10/16, Conference Frontiers in Optics, Pages FMN6, Publisher Optical Society of America

CAPITULO DE LIBRO

1. **Long period fibre gratings**
   Authors Alejandro Martinez-Rios, David Monzon-Hernandez, Guillermo Salceda-Delgado, Ismael Torres-Gomez, Publication date 2012, Publisher INTECH Open Access Publisher